# LASER SHOCK IMPRINTING OF METALLIC MEMBRANES TOWARD SOFT TEMPLATES AND ITS APPLICATIONS

by

**Shengyu Jin**

**A Dissertation**

*Submitted to the Faculty of Purdue University*

*In Partial Fulfillment of the Requirements for the degree of*

**Doctor of Philosophy**


School of Industrial Engineering

West Lafayette, Indiana

May 2019

# THE PURDUE UNIVERSITY GRADUATE SCHOOL
# STATEMENT OF DISSERTATION APPROVAL

Dr. Gary J. Cheng, Co-Chair
School of Industrial Engineering

Dr. Yi Xuan, Co-Chair
School of Electrical and Computer Engineering

Dr. Wenzhuo Wu
School of Industrial Engineering

Dr. Ramses V. Martinez
School of Industrial Engineering

**Approved by:**

Dr. Abhijit Deshmukh
Head of the Departmental Graduate Program

*To my beloved family*

# ACKNOWLEDGMENTS

This thesis is for all who supported me. It was an amazing journey to explore the unknown. Without the strong supports from advisor, mentors, colleagues, and friends, I would not reach the end line of this journey.

First of all, I would like to thank Professor Gary Cheng for providing me with a precious opportunity to pursue my graduate study in Purdue. His passion, wisdom, and curiosity leaves a huge impact on me.

I would like to thank Professor Yi Xuan, Professor Wenzhuo Wu and Professor Ramses Martinez for being my committee. Their continuous mentoring helps trim my ideas and keep them on the right track. I am deeply impressed with not only their academic background but also their willingness to mentor a young researcher.

Also many thanks to group members, Dr. Dong Lin, Dr. Qiong Nian, Dr. Yaowu Hu, Biwei, Jin, Sen, Xingtao, Licong, Maithilee, Bill, and Danilo. And for my colleagues, Dr. Bahk, Dr. Ziabari, Dr. Koh, Mojib, Yixiu, Ruoxing, Shengjie, Zhiguang, Enas. Special appreciation to Prof. Wang, Prof. Shakouri, and Prof. Bermel. And help from Wayne, Marc, Bill, Dave, Mike, Joon, Dan, Sean, Tim, Nancy, Kyle, Mary Jo, Cheryl, Erin, Jenny, Pam, Lindsay, Jill and Anita. Thanks for the helps during my Ph.D. days. For those who are not mentioned here, your kindness is always remembered.

I would like to express my appreciation to my grandparents, parents, sister, and families. I hope I am still a good grandson, son, and brother, though I have been away from them for years. Thanks for being my grandparents, my parents and my sister.

Finally, for my wife, Dr. Mo Li. It is the gift to meet with you and the luck to spend the rest of my life with you. You are such a talented girl who I have to chase since my freshmen year, and you proudly won this academic race to acquire the degree in May 2017. This is the second happiest moment to complete this thesis, and the happiest absolutely was from our wedding ceremony. Thanks for being a supportive partner during these days in West Lafayette. Now new challenges are on the way, and let’s keep boiler-up!

# TABLE OF CONTENTS

# LIST OF FIGURES

# LIST OF TABLES

# ABSTRACT

Author: Jin, Shengyu. Ph.D.
Institution: Purdue University
Degree Received: May 2019
Title: Laser Shock Imprinting of Metallic Membranes Toward Soft Templates and its Applications
Major Professor: Gary J. Cheng

Laser shock imprinting (LSI) is a novel fabrication technique capable of manufacturing various membrane materials. This top-down imprinting process can fabricate membranes in high precision, high throughput, and large scalability. It reveals a variety of applications ranging from electronics to photonics, which is beneficial from its reliable and precise modulation of micro/nanostructures.

In this thesis, we firstly proposed and developed a cost-effective LSI process to manufacture hierarchical micro/nanostructured power generators. By combining the conventional soft lithography technique, LSI is well compatible with it to fabricate metal membranes towards soft templates. It is a significant progress from the originally-developed silicon wafer template layout because it effectively reduces the process cost by replacing sophisticatedly developed silicon wafers with low-cost photocurable polymers. In addition, the use of polymer expands the boundary limit of geometrical complexity from simple patterns to hierarchical structures, as a result, we successfully conducted LSI technology to fabricate biomimic leaf structures into metallic membranes with the help of soft SU-8 templates. These fabricated metallic membraned are used as water-driven triboelectric nanogenerators. In addition to the introduction of polymer template, we further developed a successive laser shock imprinting (SLSI) process to fabricate hierarchical nanostructures in a higher resolution. Typically, grating templates are collected via recycling blank discs and used as soft templates. Then multiple times of LSI process are conducted to manufacture membranes into complex nanostructures. The use of blank disc further reduces cost and increase process resolution. The highlight of this part of work is to feature the introduction of metallic thin films on disc template, which plays a significant role during this high strain rate imprinting process. Then, the imprinting mechanism was investigated through the finite element method to validate the experimental findings. Lastly,

this soft template LSI process was applied to fabricate low dimensional materials such as nanowires (1D) and nanomembranes (2D), potentially introducing homogeneous and inhomogeneous strain field. Kelvin probe force microscopy was used to directly probe strain-induced changes. This soft-template LSI process reveals a new route of precisely fabricating low dimensional membranes into nanoelectronics systems.

# CHAPTER 1. INTRODUCTION

## 1.1 Motivation

In 1917, Dr. Albert Einstein discovered a phenomenon called stimulated emission, where a photon travels through the excited medium, resulting in relaxation from the excited state to ground state while emitting a new photon, which is identical to the initial photon in terms of energy, wavelength, and phase condition. The electron on the ground state can be pumped to excited state again by the applied external energy source. This process is named pumping process. Laser was firstly built based on these principles by Theodore Maiman in 1960. Since then, beneficial from developments of different types of laser system, laser has been widely used in a variety of industrial, research, medical and military applications.

Laser interaction time is one of critical parameters to predict the effect from irradiation on the target material. Generally, Laser could be categorized into two major modes depending on the continuity of pumping and emission: continuous wave (CW) mode and a pulsed mode. In the subcategory for pulsed mode, it includes the long laser pulsed one (the duration in the magnitude of microsecond, $10^{-6}$ s), the short laser pulsed one (the duration in the magnitude of nanosecond, $10^{-9}$ s), and ultrashort laser pulsed one (the duration in the magnitude from picosecond, $10^{-12}$ s to femtosecond, $10^{-15}$ s). The longer pulse duration lasts, the more obvious heating effect is observed. Based on the desired duration of heating effect, a variety of durations of laser pulse is used in different applications. Long pulse-duration lasers are generally used for laser forming, welding, cladding, and the shorter counterparts are employed in laser ablation[1]. Among these different types of laser, we explore short laser pulse (nanosecond) system and its application as the laser dynamic behavior.

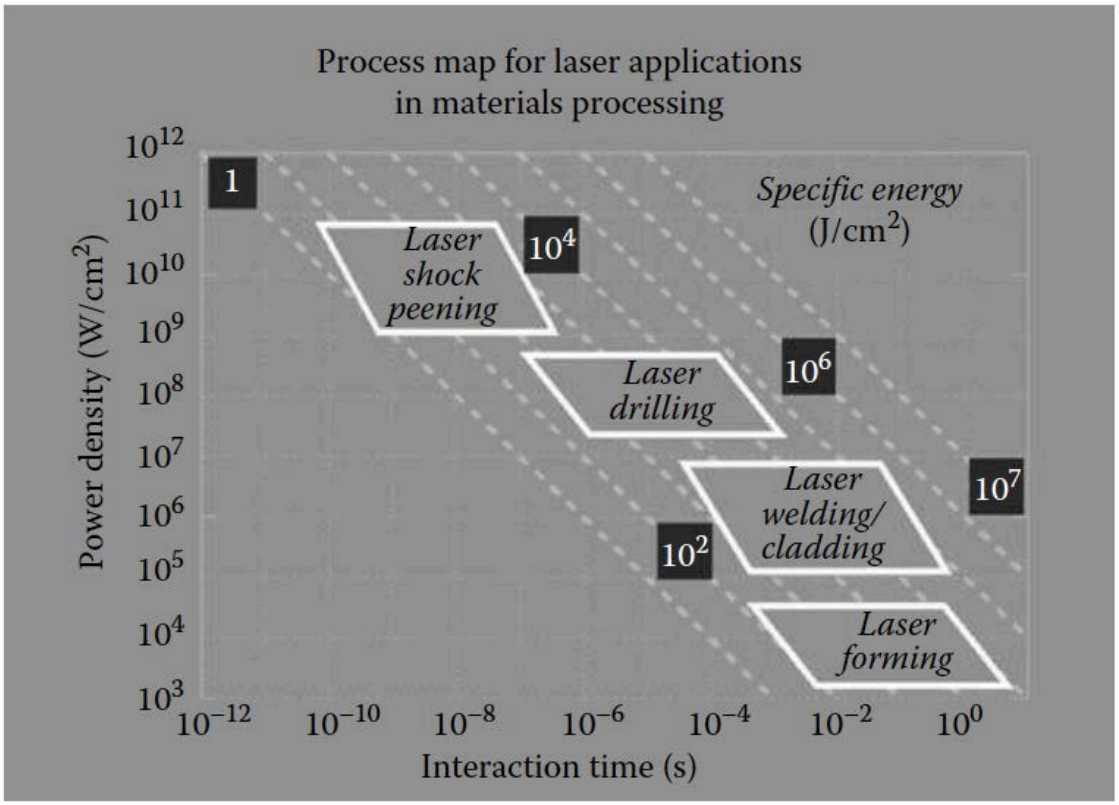


Figure 1.1 Process map for laser application in material processing. Adapted by permission from CRC Press Taylor & Francis Group. ref. 1. Copyright 2017.

When the laser-matter interaction time is reduced to nanoseconds, the significant phenomenon for this process is ablation. The mechanism for nanosecond-pulsed laser ablation is the sequential combination of the melting, due to short-time period temperature elevation, the absorption of photons, and evaporation, due to continuous photon absorption. These evaporated materials could convert into the plasma once lost electrons due to the existence of laser irradiation. Because of the instantaneous expansion of vaporized materials, the resultant shock pressure generated from this process could reach up to several tenths of one GPa[2]. Confined within the proper media, the shock pressure could be amplified by a factor of five. Such high pressure is beyond the yield strength for most metals, and this technique, therefore, is widely employed in introducing plastic deformations as well as defects aiming at increasing the mechanical properties[2].

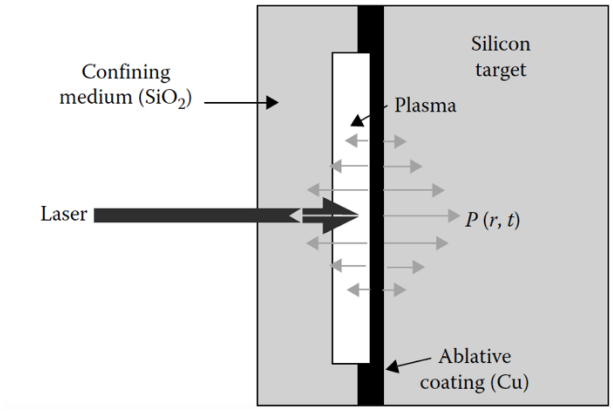


Figure 1.2 Laser Shock Peening Process Set-up. Adapted by CRC Press Taylor & Francis Group. ref. 2. Copyright 2017.

In 2014, our group has successfully applied this high-pressure laser process into sub-10nm accuracy shaping process[3], named Laser Shock Imprinting (LSI). This technique takes advantages of instantaneous high pressure and temperature, which could induce high strain-rate for metals to be plastically deformed without any mechanical damages. Previous fabrications of metallic structure highly rely on time-consuming processes, such as raising the temperature above the glass transition temperature for metallic glass[4] and multiple steps of sophisticated methods. This process has been intensively studied from bulky materials to nanoscale materials to explore tunable and unique properties in terms of electronic and mechanics[5,6]. Majority of these researches are founded on the well-designed and sophisticatedly fabricated hard molds, generally silicon mold. However, the cost of this fabrication lay a barrier to keep this process from being widely applied in scalable processes.

## 1.2 Objectives

The ultimate goal of this thesis is to further expand the application of LSI technique by developing and selecting a variety of cost-effective and reliable soft templates. By doing this, the cost of the process is significantly reduced while the imprinting quality remains at a comparable level. In addition, the advantage of soft templates, such as 3D formability, scalability, reliability, will be potentially adopted by LSI process. Lastly, the final stage of

the study will be focused on the application of this method on fabricating low dimensional material. As this process was originally designed to fabricate membranes and thin films, which are dimensionally compatible with low dimensional materials such as graphene (2D) and nanowires (diameter less than 100 nm). Based on the aforementioned motivation, this thesis aims to accomplish following objectives:

(1) LSI/Soft templates-fabricated self-powered triboelectric devices: Soft templates are developed to fabricate multiscale micro/nanopatterns, which is incapable of by silicon wafer-based photolithography. Then, the imprinting resolution limit is systematically investigated. Besides, the finite element method is studied to investigate deforming mechanics of soft templates. Lastly, the application of LSI into the power generator, triboelectric devices, is systematically studied.

(2) SLSI process of fabricating nanophotonic patterns: Evolved from originally developed soft template LSI, SLSI is capable of manufacturing complex hierarchical patterns metallic membranes using trench molds. The templates are as simple as blank optical discs. The unique concept of SLSI is imprinting a membrane multiple time using simple trenches templates to generate complex nanophotonic patterns. The capability of SLSI is systematically studied and the imprinting mechanics of disc templates were numerically investigated.

(3) LSI/Soft templates process on low dimensional materials : LSI process was applied to imprint low dimensional materials to induce homogeneous and inhomogeneous strains. A variety of low dimensional materials were investigated. Graphene survived along with a series of test. The straining effect is investigated using Kelvin probe force microscopy.

## 1.3 Structure of the dissertation

The dissertation is structured as follows: (1) Chapter 1 is the introduction of LSI process and the objectives. (2) Chapter 2 presents a literature review on laser processing and the evolution of LSI process. (3) Chapter 3 summarizes characterization techniques used in this thesis. (4) Chapter 4 gives the development of soft templates and its application

and feasibility (experimentally and numerically) as LSI templates. The resolution limit was also investigated. Lastly, the fabricated membranes were used as triboelectric power generators, and their power output was further optimized. (5) Chapter 5 presents SLSI process developed from simple trenches molds adopted from optical discs. Hierarchical photonic patterns were developed by combining a variety of parameters such as laser intensity and types of molds. (6) Chapter 6 provides a direct application from LSI on low dimensional materials. (7) Chapter 7 is the summary of the dissertation.

# CHAPTER 2. BACKGROUND AND LITERATURE REVIEW

## 2.1 The overview of nanoimprinting on polymers

As early as in 1970, Bartolini et al. have developed an embossing process to fabricate hologram motion pictures for imaging applications[7]. In 1978, Philips announces the compact disc (CD) project and, four years later, released its first CD products with Sony. The manufacturing of CD relies on the technology of pressing using its master mold to rapidly replicate stored data into products. The imprinting techniques were further adopted by academia in the 1990s. Along with Soft lithography[8] (by Xia et al.) and Step-and-Flash imprint lithography (SFIL) [9] (by Colburn et al.), nanoimprinting lithography (NIL) [10,11] were developed Chou et al. and this technology successfully achieved sub-25 and sub-10 nm resolution lithography.

### 2.1.1 Nanoimprinting process on polymers

The principle of NIL is shown in Figure 2.1. A hard mold containing nanoscale features is pressed into a polymer-coated substrate. Due to the thermo-rheological nature of the polymeric substrate, the hard-mold impress results in the thickness contrast on it. Usually, the polymeric substrate is followed by $O_2$ reactive ion etching (RIE) to remove the residual polymeric layer, exposing the silicon substrate.

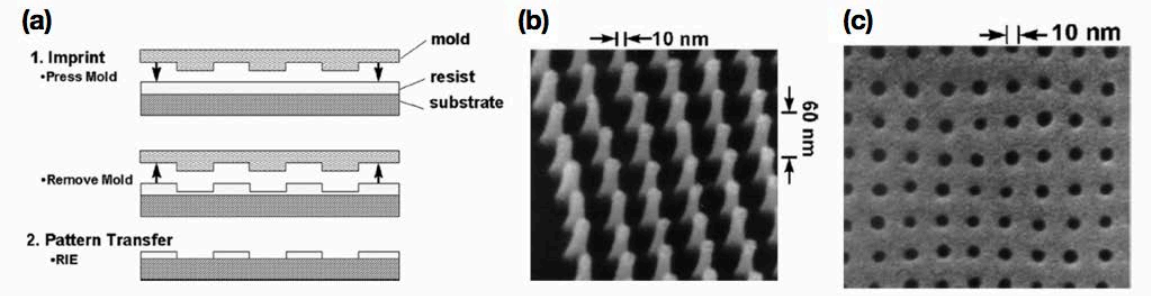


Figure 2.1 (a) The Originally proposed NIL process, (b) Scanning electron microscopy (SEM) image of a NIL mold of pillar arrays with 10-nm diameter, and (c) SEM image of a NIL-fabricated polymer substrate using such a mold in (b). Adapted by American Institute of Physics. ref. 10. Copyright 1997.

NIL is a high-throughput and cost-effective process with a simple equipment layout, leading to a scalable manufacturing with high accuracy. Given these promising advantages, this technology attracted the spotlight as a candidate of next-generation lithography for integrated circuits (ICs), according to International Technology Roadmap for Semiconductors (ITRS) in 2003. Soon after the development of NIL, the so-called SFIL process was developed in University of Texas[9]. The critical difference of the process, compared to NIL, is the introduction of ultra-violet (UV) light during imprinting. Instead of reforming plastic from a planar layer into a nanoscale-featured layer, SFIL initiates from a UV-curable polymer, then cures it into the inverted form (or female-type) of the designed mold (male-type).

### 2.1.2 NIL mold fabrication

Considerations for mold candidates include hardness, thermal expansion, and compatibility with current micro/nanofabrication technology. Among a variety of candidates, Si and $SiO_2$ become superior ones due to sufficient hardness and durability as well as the excellent compatibility with the modern fabrication process. Another advantage over other candidates as molds is minimum thermal expansion mismatch between Si (or $SiO_2$) and polymer coatings. The large mismatch of thermal expansion significantly affects the imprinting output by resulting in distortions[12].

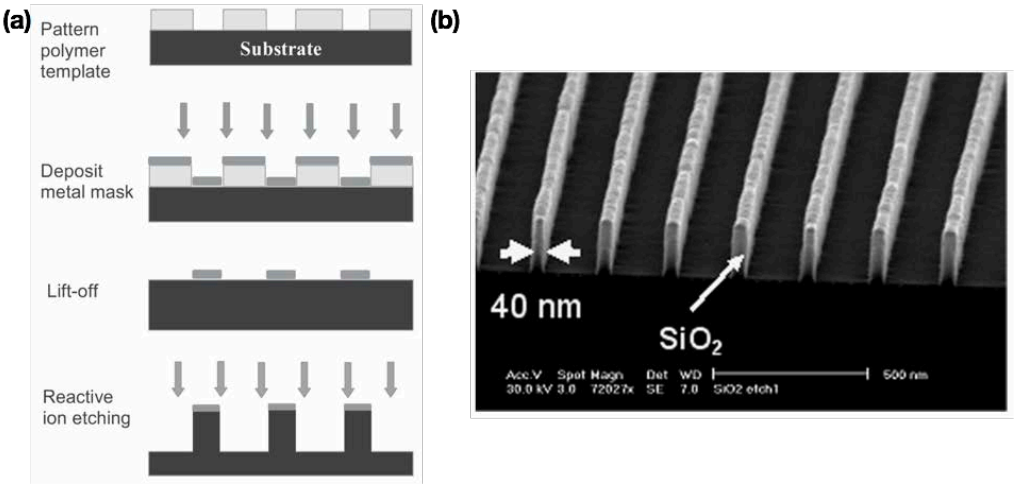


Figure 2.2 (a) Mold fabrication and (b) SEM image of fabricate $SiO_2$ trenches. Adapted by Wiley Group. ref. 12. Copyright 2007.

The fabrication process is adopted by surface machining process of photolithography on Micro-electro-Mechanical system (MEMS). Typically, the casted polymer layer is patterned, followed by the deposition of a metal layer as a hard mask. After the polymer layer is lift-offed, RIE process is performed to further etch the silicon to complete the final mold with high aspect ratio. Figure 2.2 (a) shows the schematic flow chart of such fabrication, and (b) shows the final product of the fabrication.

As scaling down the feature sizes of mold, the protrusions inevitably increases contact surface areas between the mold and the polymer substrate. As a result, the adhesion between them is effectively high, leading to the difficulty in the delamination. To address this issue, self-assembled monolayers (SAMs) are formed on the surface of the mold to effectively reduce surface energy to ease the delamination process[13].

### 2.1.3 NIL Resist

NIL replicates the surface relief patterns on the polymer resist layer, the ideal properties for resist materials are easy deformability and mechanical strength as well as easy delamination from the mold. In addition, etching selectivity to underneath hard substrate is important when determining the aspect ratio after the pattern transfer from the resist into the substrate. Hirai et al[14]. reported that, during the imprinting, the resist material has lower Young's modulus than that of the mold (generally Si or $SiO_2$), and that the minimum pressure is higher than the shear modulus of the resist material. Usually, NIL is conducted at an elevated temperature and the major reason is the reduction of shear modulus of the polymer resist, thus flowing the resist into mold features. To complete the imprinting process in a reasonable timeframe, the viscosity should be sufficiently low enough to ease the process[15]. This thermo-rheological requirement is explained by a simple model of the squeezed flow of a Newtonian liquid between plates with a radius of R and a gap with a distance of d[16]. The explanation of such model is presented below:

$$P = \frac{3\eta R^2}{4d^3}\frac{dh}{dt} \quad (1)$$

P represents to the applied pressure, η is the viscosity of the resist material during the process, and dh/dt is the imprinting speed. Under a reasonable imprinting speed, the lower of the viscosity is, the less endeavor of imprinting is needed to complete the imprinting.

Thermally plastic polymer resists are one of the mostly used agents. The advantage of such agents is simultaneously qualifying for two key requirements, low Young's modulus and low viscosity, by raising the temperature beyond the glass transition temperature ($T_g$). One of the typical thermally plastic polymers is poly(methyl methacrylate) (PMMA). Figure 2.3 shows the significant change over the temperature and its corresponding retardation time.

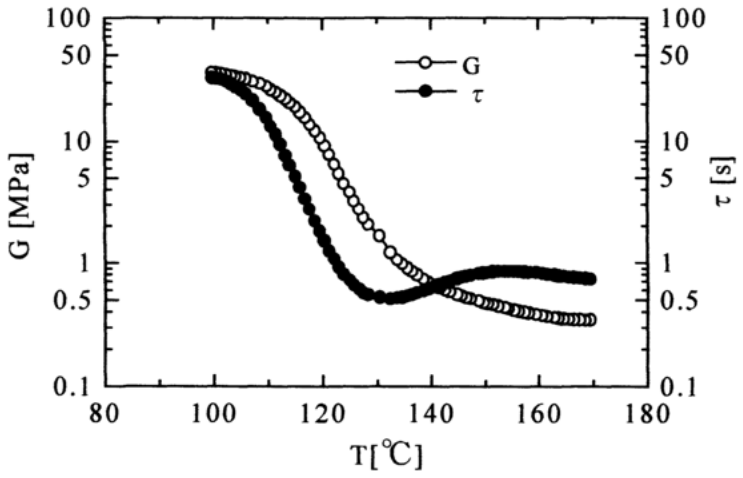


Figure 2.3 Measured rheological property of PMMA. G: shear modulus and τ: retardation time. Adapted by the society of photopolymer science and technology. ref. 14. Copyright 2002.

The limitation of the use of thermally plastic polymers is the high-temperature induced thermal expansions. Though the inherent thermal expansion mismatch between the polymer and Si (or $SiO_2$) can be eased by using low-surface energy coating, the perfect release of mold from the polymer-casted substrate is not guaranteed. Thus the alternative approach is the use of UV-curable liquid precursors. The viscosity of this liquid precursor is inherently low in the room temperature, therefore, the imprinting process does not require external heating but the flood of UV light. Therefore, the transparent copolymer is generally used as the mold.

### 2.1.4 The deformation process of NIL

Hirai and coworkers reported that the original thickness and pressure applied will make a direct impact on the formation process[17]. It is indispensable to investigate the temporal evolution of deformation of polymer resists to obtain the optimistic geometry.

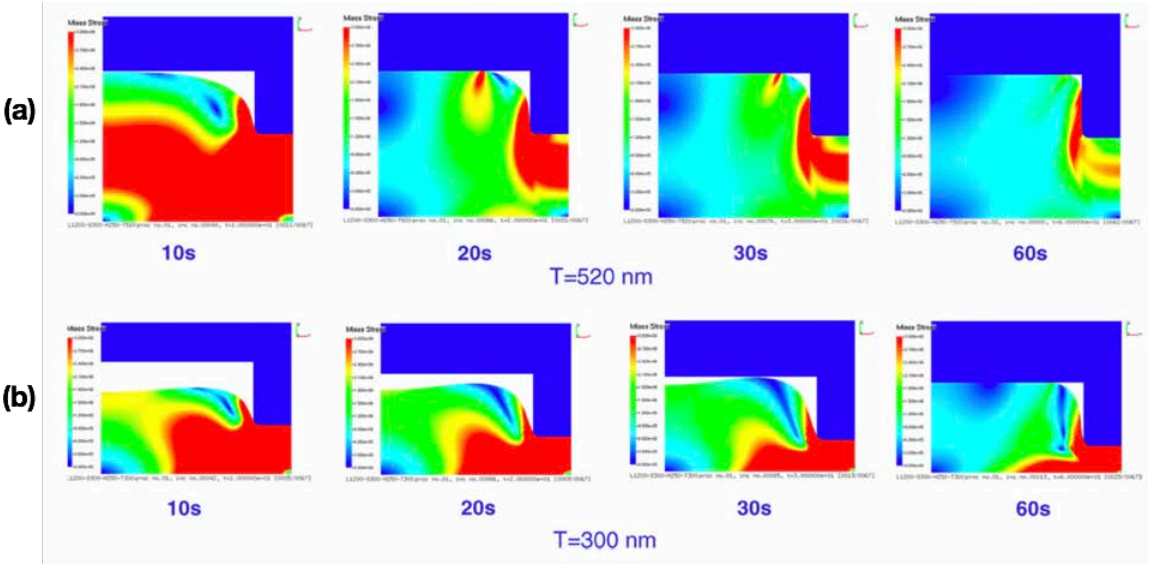


Figure 2.4 Temporal evolution of deformation of (a) thick resists and (b) thin resists. Adapted by Elsevier. ref. 17. Copyright 2008.

As presented in Figure 2.4, there is a tremendous difference in temporal deformation in the resists. Typically, the geometry of deformed resists presents twin peaks (here is a single peak near the mold edge). This is majorly due to the fluidic flow in thin resist cases is majorly limited on the edge, thus leading to a formation of a peak near it. This numerical result is confirmed by our own trial of nanoimprinting, as shown in Figure 2.5.

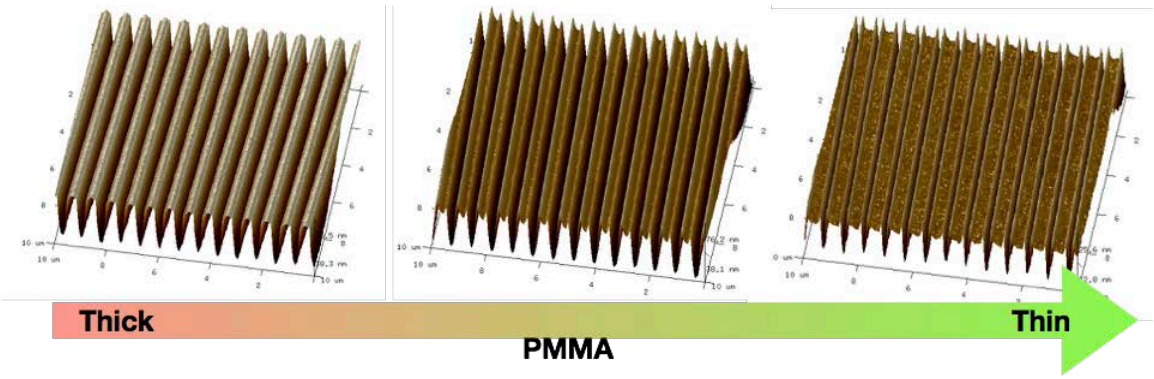


Figure 2.5 Thickness dependence of PMMA deformation under identical pressure.

## 2.2 The overview of micro/nanoimprinting on metals

In spite of attractive mechanical stability, micro/nanoimprinting of metals have not been widely studied and developed due to the constraints of grain size effects as well as structural dislocations [18]. There are effective solutions to bypass such microstructural constraints such as the use of finer or amorphous crystalline[19], thermal process[20], and the employment of mold with extremely high hardness such as SiC or diamond[21,22]. However, the side effects accompany with such solutions. For example, the long-term heat treatment inevitably brings in surface oxidation at the ambient environment, and the operation cost raises if vacuum configuration is coupled thus the manufacturing is not effective in terms of the productivity and the cost. The fabrication of hard mold is feasible, however, the cost of vacuum etching is relatively high and it is difficult to guarantee the repeatable use of mold due to the extremely high hydraulic pressure necessary during the process. Assuming that the use of a mold is repeatable, the following difficulty of micro/nanoimprinting of metal is the strong capillary forces at small scales. The molding pressure, therefore, is dramatically elevated, as a result, the deformation at such scales becomes challenging.

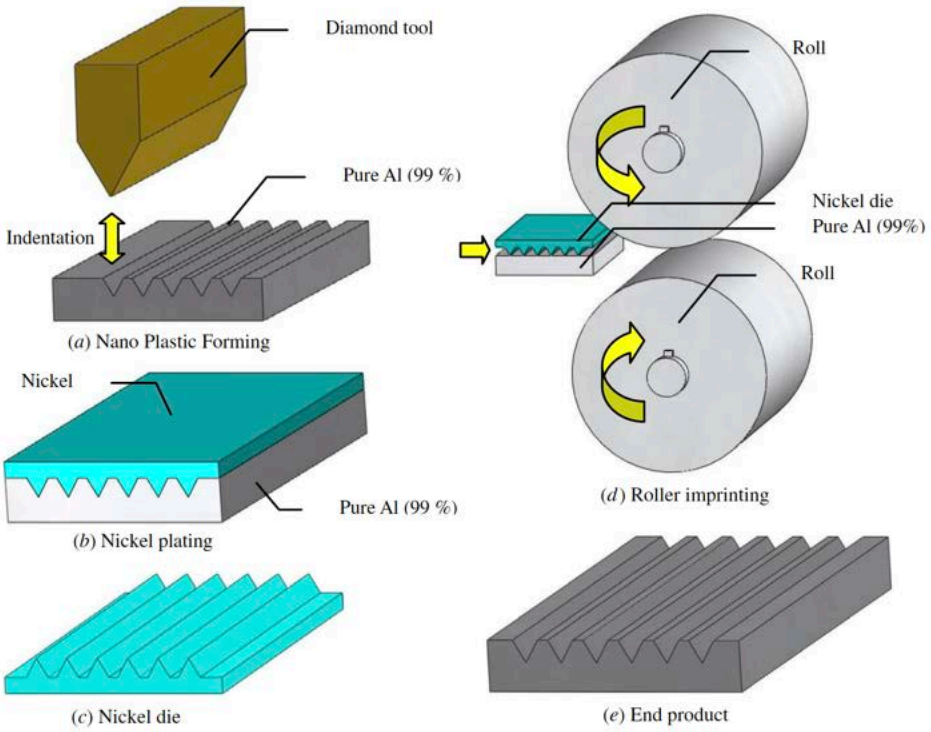


Figure 2.6 Schematic diagram of the micro/nanopattern fabrication process. Adapted from IOP Publishing, ref. 18. Copyright 2009.

The conventional metal imprinting tool wear is listed in Figure 2.6. Imprinting of metallic materials requires very high pressure at ambient condition, only few of materials are good candidates for tool wear. To reduce the pressure applied, the heating might be effective. However, external heat treatment complicates the tool wear set, and it might introduce necessary oxidation, resulting in cracks. It is necessary to develop a technique that is capable of micro/nanopatterning with easy toolsets.

### 2.2.1 Laser shock pressure generation

As mentioned previously, laser ablation occurs when the pulse duration is in the range of $10^{-9}$ s. The phenomenon occurs when a pulsed laser with high energy intensity irradiates the solid surface, the irradiated area is gasified and possibly losing electrons due to the high temperature, high pressure, and strong electromagnetic field on the surface, leading to the generation of plasma. If the irradiated surface is confined under media such

as water or hard glass, the plasma-generated pressure propagates into the solid surface, resulting in a huge shock pressure. This phenomenon is widely applied in surface engineering areas such as laser shock peening and laser dynamic forming.

A laser shock peening model is developed by Fabbro and co-workers[23,24]. The model is based on the conservation of the momentum and energy, described as follow:

$$\frac{dL(t)}{dt} = \left(\frac{1}{Z_1} + \frac{1}{Z_2}\right) P(t) = \frac{2}{Z} P(t), \tag{2}$$

$$I(t) = P(t)\frac{dL(t)}{dt} + \frac{3}{2a}\frac{d}{dt}[P(t)L(t)] \tag{3}$$

where P(t) is the pressure of the plasma and $Z_i$ is the shock impedance of materials, such as confinement medium and target materials. The shock impedance is calculated as $Z_i = \rho_i D_i$, where $\rho_i$ is the density of material and $D_i$ is the shock velocity through the material. I(t) is the transient (t) absorbed laser energy. L(t) is the depth from the surface. A typical temporal profiles of plasma pressure and laser intensity in the below[25]. Typically, the laser intensity is reaching 1GW/cm$^2$, the estimated plasma pressure is 1GPa and it decays within ~ 100 ns. The pressure is much beyond the yield strength of metals.

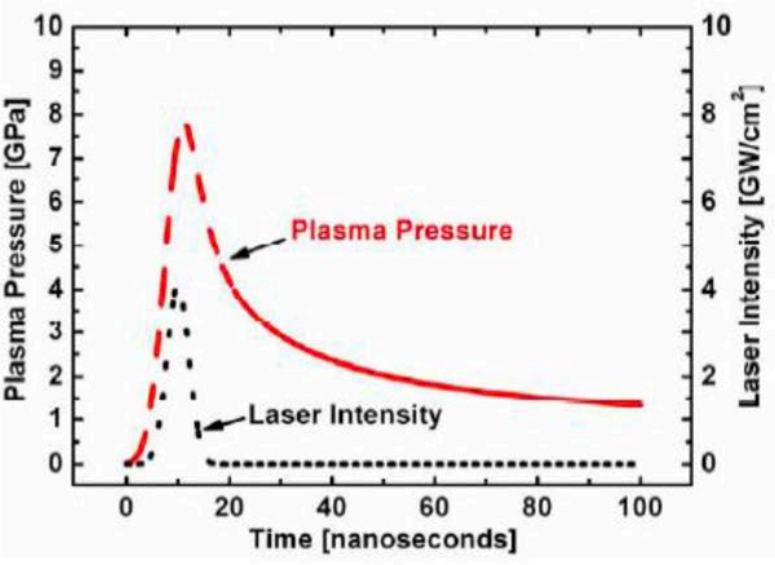


Figure 2.7 Temporal profiles of laser intensity and generated plasma pressure. Adapted from ASME, ref. 25. Copyright 2012.

2.2.2 Laser dynamic forming (LDF) and LSI

The laser shock pressure was adopted in a variety of applications such as improving mechanical properties[26,27]. In 2009, Dr. Gary Cheng's group has successfully applied this high pressure forming process to metal micro/nanopatterning process, initially called LDF[28–32] and further modified as LSI[3,5,6,33]. A typical layout for LSI is present in Figure 2.8 below. A thin film metal foil or membrane is placed on the mold, and a pulsed laser irradiates to the top side of the membrane. Due to the high pressure of plasma, the metal foil is deformed into the mold, resulting in a inversed structure to the original mold. The process is performed at the ambient environment, and it is free from complicate tool sets and temperature controls.


Figure 2.8 A schematic illustration of LSI layout. The confinement layer is omitted here.

Gao et al. firstly developed LDF and formed metallic foils into 2D and 3D meso-micro-nanostructures. It reveals the superplastic behavior of LDF process, which is induced by ultrahigh strain rate of ~ $10^6$ $s^{-1}$ to $10^7$ $s^{-1}$ He also reported that LDF can improve mechanical strength due to strain hardening and the refinement of grain size[29]. Figure 2.9 directly presents the capability of LDF or LSI on the micro/nanopatterning. The smallest

feature size could reach ~ 10 nm, which is comparable to current IC fabrication node size of ~ 7 nm.

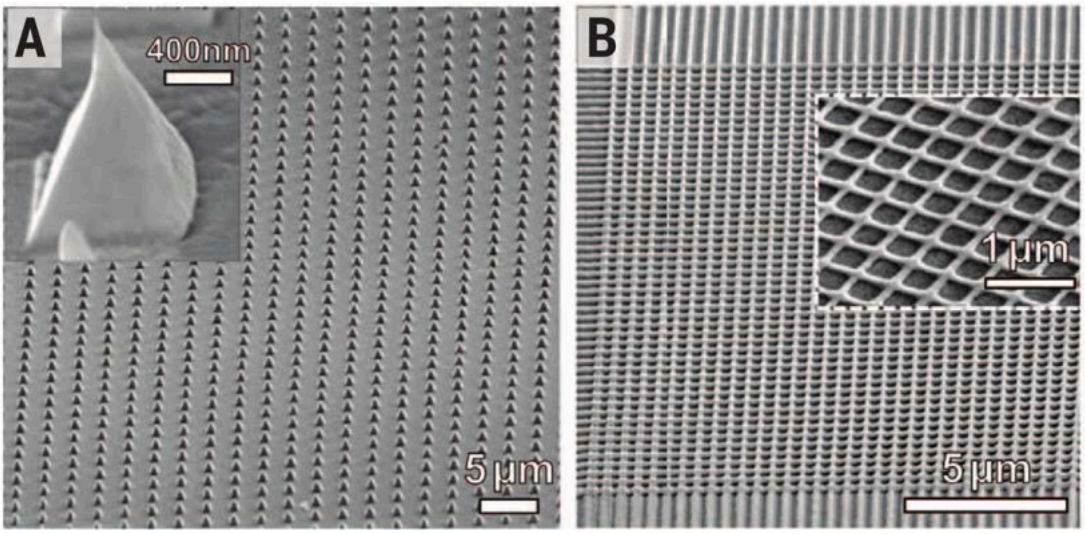


Figure 2.9 SEM images of fabricated micro/nanostructures: (A) Pyramid and (B) Fish-nets. Adapted from AAAS, ref. 32. Copyright 2014.

At the meanwhile, Li et al. applied LDF to imprinting of low dimensional materials such as nanowires[34] and graphene[35,36]. For example, the strain engineering of nanowires has a variety of promising applications in the modulation of electronic and mechanical properties as well as band structure engineering. In 2012, LDF is firstly applied to imprint to strain nanowires and the maximum strain is about 110% locally. In addition, the nanomembranes such as graphene are introduced with this technology to deform against nanofabricated molds[35]. The strain effect was characterized via Raman spectroscopy of the fingerprint of 2D peak. The record of shift is 15 $cm^{-1}$ when the deformed aspect ratio is beyond 0.1. The advantage of the technology is the modulation of strain using the applied laser energy and corresponding plasma pressure.

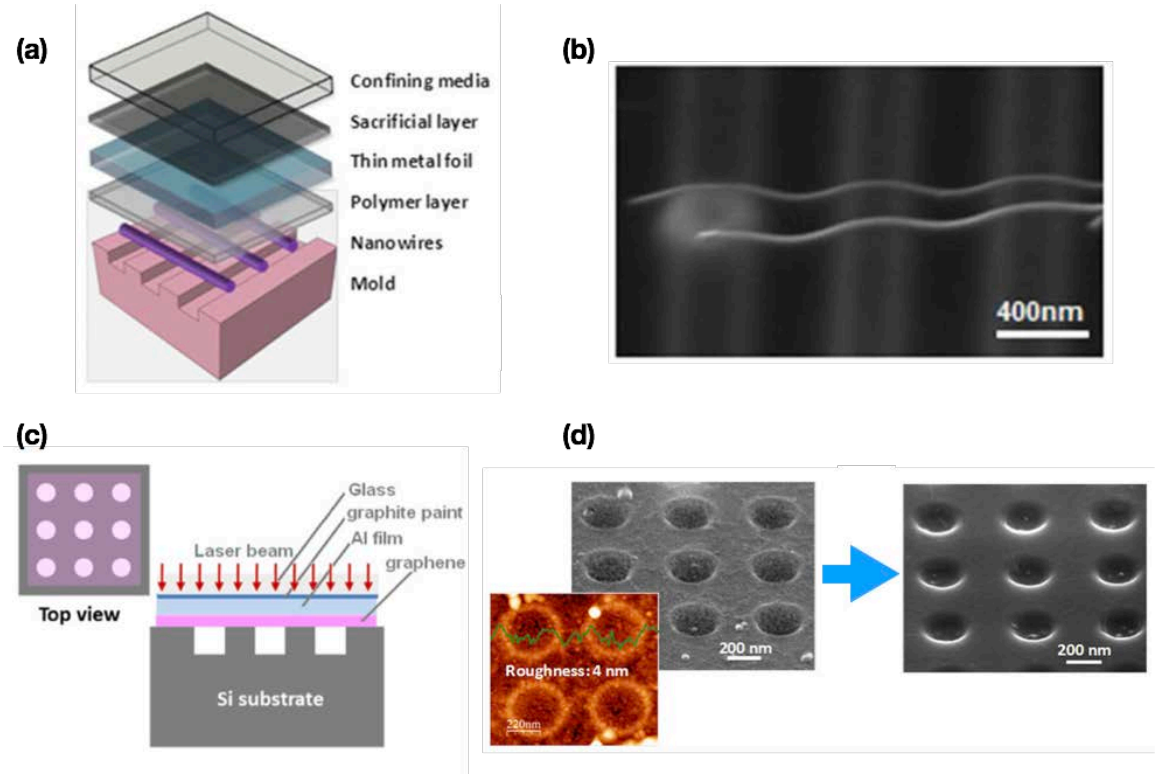


Figure 2.10 (a) a schematic illustration of imprinting of nanowires using LDF, (b) a SEM image of imprinted nanowires (Ag), (c) a schematic illustration of imprinting of graphene, and (d) SEM images of graphene before and after LDF, lower left: AFM image of before LDF. Adapted from IOS publishing and ACS. Ref. 34–36. Copyright 2011 and 2012.

Hu et al. modified the process name into LSI and applied it to the nanoshaping into semiconductor nanowires[5]. As Figure 2.11 shows, the germanium nanowires were LSI-ed and the devices were fabricated on. The mobility was improved due to strained nanowires. The strained effects were confirmed geometrically using SEM and AFM, and the optical approach of Raman spectroscopy was used to characterize the strained effect.

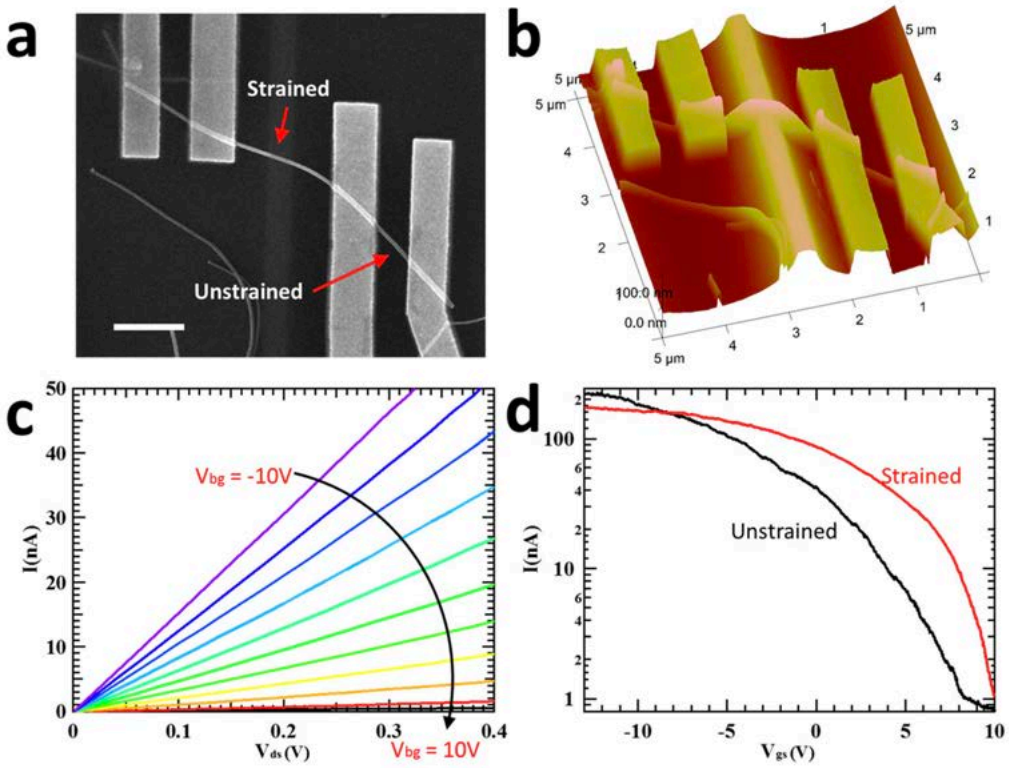


Figure 2.11 (a) an SEM image of strained semiconductors and in-situ fabricated devices, (b) a corresponding AFM image of (a), (c) output electrical characteristic, and (d) transfer characteristics of Ge nanowires. Adapted from ACS. Ref. 5. Copyright 2016.

Apart from the application of LSI into imprinting of low dimensional membranes and nanowires, LSI was further developed to pattern metallic membranes for optical sensors. Because LSI is the imprinting process providing a high pressure beyond the yield stress of most metals, it was used to imprint the plasmonic materials such as Al, Ag, and Au into periodic nanostructures[37,38] and ultrafine-gaped structures[33].

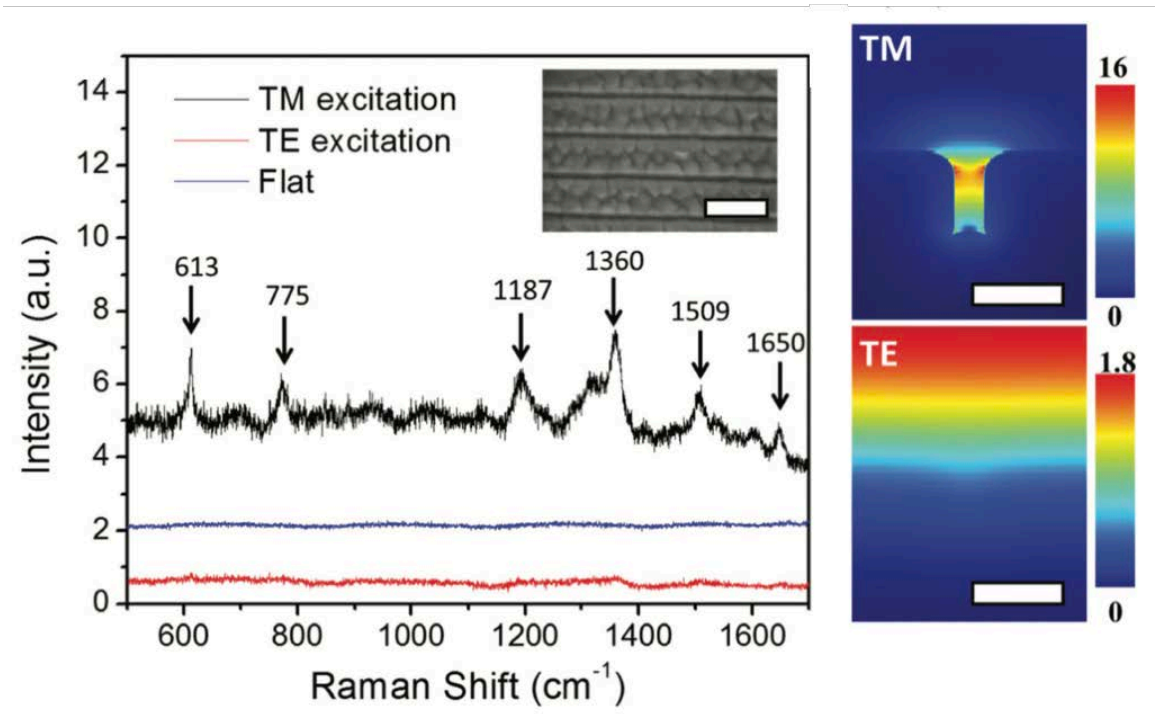


Figure 2.12 Raman spectra of R6G molecules on LSI-ed metallic structures (left) and electromagnetic field enhancements along different polarizations (right). Scale bars: 150 nm (left) and 50 nm (right). Adapted from RSC. Ref. 37. Copyright 2016.

As Figure 2.12 shows the ultra small-gaped trenches of Ag is generated through LSI. This periodic structured plasmonic materials shows the potential as an optical sensor to detect the ultralow concentrations of molecules such as R6G. This grating structure of plasmonic structures also shows the optical anisotropic property. Furthermore, a pair of metallic structures is fabricated closed to each other with a gap of 10 nm. LSI can help to create ultrafine gaps near 1nm by compressing the deposited metallic nano-columns, as Figure 2.13 showing below.

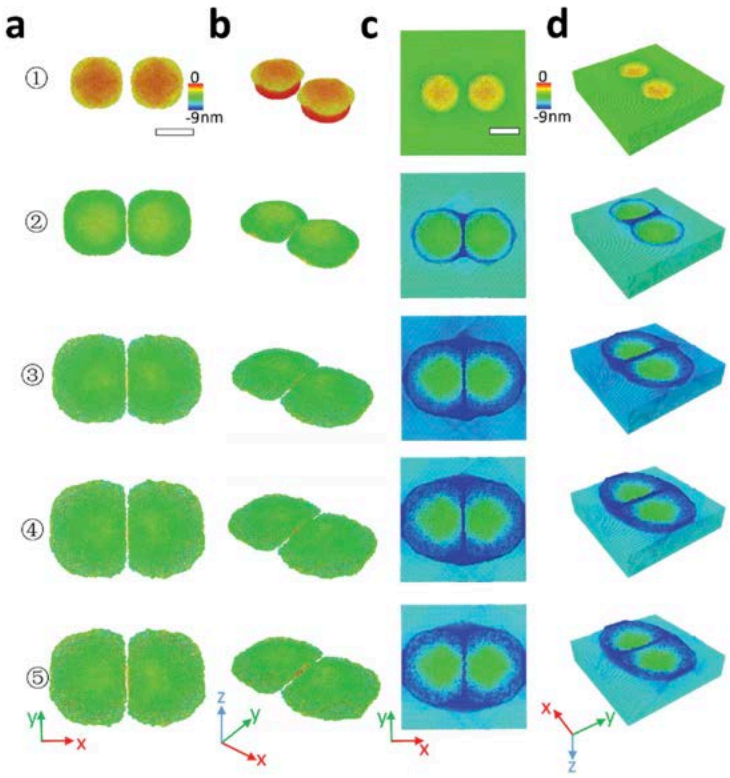


Figure 2.13 Generations of ultrafine gaps using LSI process. Adapted from Wiley. Ref. 33. Copyright 2016.

## 2.3 The fabrication of LSI molds

Mold or template is another critical part of the whole LSI process. Generally, the mold is made of hard materials because the target materials are the membrane or foil with the relatively softer mechanical property. Due to the difference between mechanical property such as hardness and ductility, the membrane can be successfully imprinted into a harder mold. In the following part, mold types or methods of fabrications are listed.

### 2.3.1 As-received Microscale molds

Transmission electron microscopy (TEM) grids can be used as molds because grids are reliable in dimensions and mechanical properties. TEM grids are made of hard metals such as copper and nickel. The mesh dimensions are ranging from 113 μm to 7.5 μm. Al foils with LSI process is presented in Figure 2.14. Coins can be used as a template, and the Al can be imprinted with high fidelity. Optics with structural features are also good candidates as molds. For example, holographic grating structures provide structures with a

variety of periodicity. Typically, these optics can be categorized depending on the number of grating lines in 1 mm. 300, 600, 900, 1200 lines are patterned in 1 mm dimension, and the corresponding periodicity is 3.3 μm, 1.6 μm, 1.2 μm, and 0.9 μm, respectively.

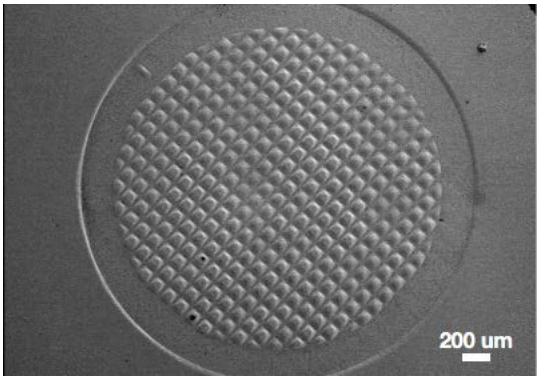


Figure 2.14 A copper foil is imprinted towards TEM grids.

### 2.3.2 Photolithography

Photolithography is one of the most widely used patterning processes in current IC fabrication. The working principle is applying photons to polymer resist under the designed mask to initiate photonic interactions, which can be further removed or remained depending on demands, completing the patterning step. As an example of positive polymer resist, polymer resist patterns are deposited with e-beam evaporated metallic thin film, and further removed by the developer solution, remaining metallic patterns on the substrate. Current IC fabrication requires a higher density of transistors in limited regions to meet Moore's Law. The resolution of the important parameters. Up to date, the current technology of using extreme ultraviolet (EUV) to generate 13.5 nm wavelength starts to be used in high volume production. Due to the access limitation in academia, the mostly used photolithography equipment can successfully reach the resolution of 3 μm. Though Hg lamp source with i-line (wavelength of 365 nm) is used, the resolution of the mask cannot be reached highest enough to achieve the resolution limit.

As mentioned before, a silicon wafer is the material with sufficient hardness and fully compatible with current IC fabrications. Thus, the evolution of LSI begins with the silicon mold fabrication. One of the representative structures is the LSI fabricated pyramid.

The fabrication process is following, the silicon wafer was patterned with square arrays and soaked into a strong base solution such as KOH and NaOH to initiate the wet etching. Due to the directional difference of the packing density of Si atoms, the silicon wafer was etched faster in one direction than the other, thus leaving the inverse structure of pyramids as Figure 2.15 depicts.

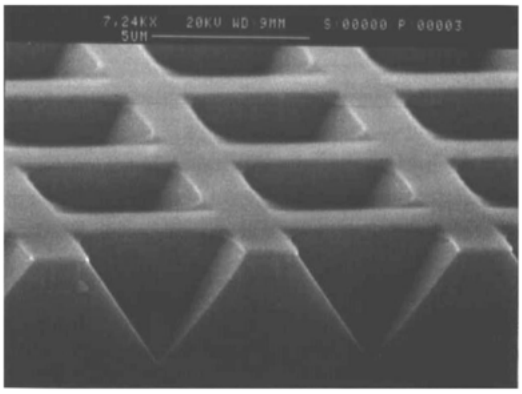


Figure 2.15 Anisotropic wet etching of Silicon. Adapted from The Royal Society. Ref. 39. Copyright 2006.

Al foil was placed on top of such mold, and LSI was applied. The high pressure facilitates the deformation of foil into such structures and leading to positive-toned pyramid structures.

### 2.3.3 Focused Ion Beam (FIB)

FIB is another commonly used equipment of fabricating the mold. The instrument of FIB is identical to SEM except for the type of beam. FIB used ion beams rather than electrons. Because the ions are higher charged and heavier than electrons, thus they are used to mill the surface of the wafer (Si) to thin materials. Moreover, the precise control of beam energy and the dose can facilitate the modulation of milling depth. The most common use of FIB is the preparation of cross-section of the sample, and further to thinning the samples for the requirement of TEM characterization. In LSI mold fabrication, FIB is generally used to create the trenches with a variety of aspect ratio, which is greatly critical to examine the strain ratio for low dimensional materials.

### 2.3.4 E-beam Lithography (EBL)

EBL is one of highest resolution equipment. The wavelength of e-beam is the lowest among carriers and medium, thus the corresponding resolution is highest. Analogous to photolithography, the beam source is electron, and the polymer resist is PMMA. The technology can achieve sub-10 nm patterning if the dose condition, as well as polymer resist, is optimized. In spite of the advantageous high resolution, EBL is not widely used in IC fabrication due to the low throughput.

### 2.3.5 Nanoimprinting Lithography

As mentioned in 2.1, the NIL is mostly used to imprint the polymer. Thanks to the technology of RIE, the imprinted patterns could be transferred to the substrate underneath with selectivity of polymer/substrate. The feature below shows the pattern transferred after PMMA is etched away, remaining silicon parts. Figure 2.16 shows the side-by-side comparison of NIL-ed PMMA and corresponding Si patterned. The periodicity of patterns remained the same, however, the aspect ratio is changed. This is because the selectivity of the etching medium to PMMA and that to Si is different.

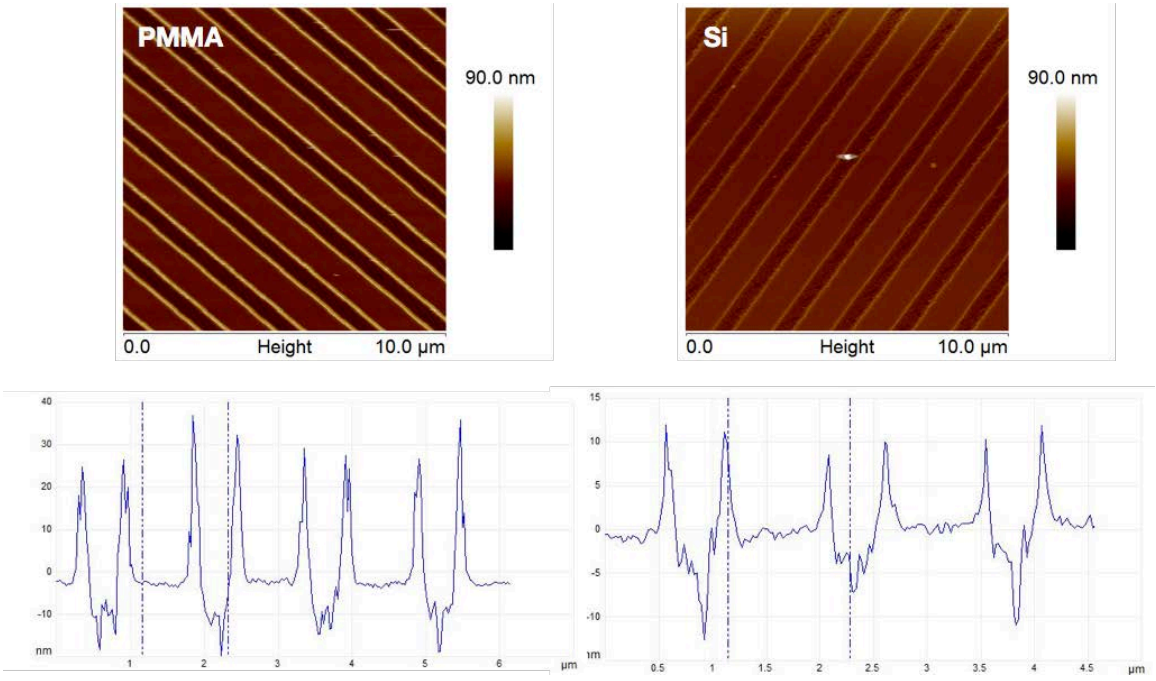


Figure 2.16 AFM images of patterns for PMMA (left-up) and etched Si (right-up), and corresponding surface profiles.

In addition, if the etching is performed in a certain direction, the pattern will be tilted according to the introduced angle, as Figure 2.17 exhibits. The whole substrate is tilted 30 degrees during the RIE removing of PMMA, and the final output of pattern is anisotropic and tilted. Though these kinds of process is unique in terms of pattern generation, the long-term vacuum process is not cost effective. The etching inevitably introduces roughness of material, which lowers the fabrication quality and performance.

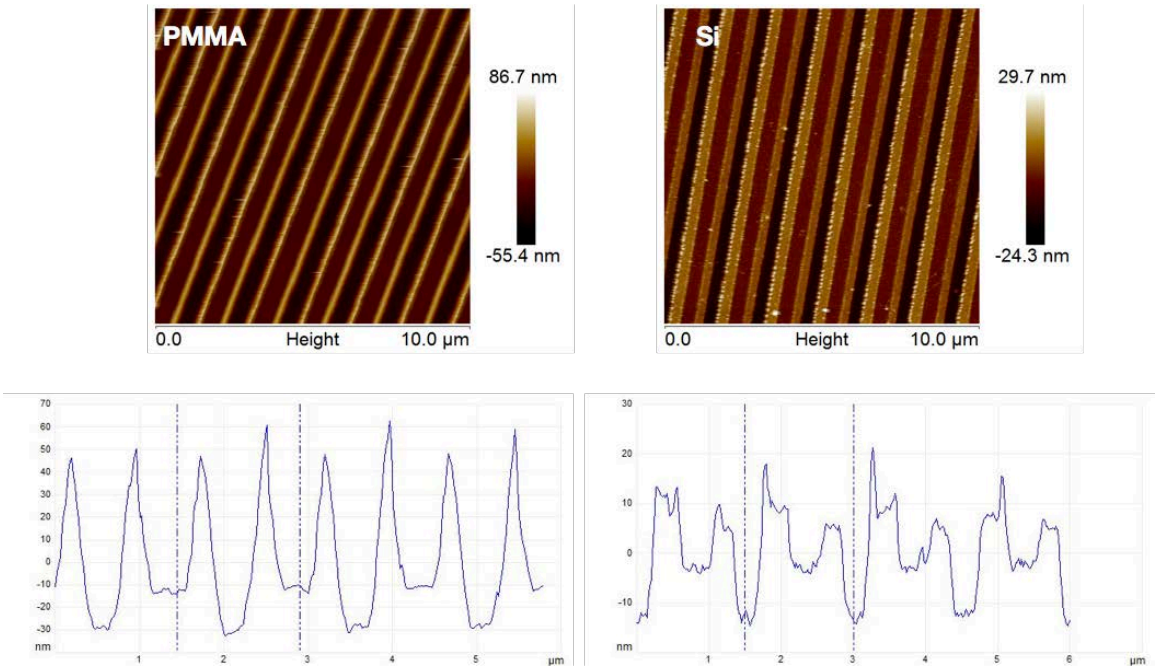


Figure 2.17 AFM images of patterns for PMMA (left-up) and tilt-etched Si (right-up), and corresponding surface profiles.

## 2.4 The comparison of mold fabrication

Table 2.1 lists the comparison between resolution limits and throughput among different molds. As-received molds such as TEM grids and optic gratins are fabricated through vendors so the throughput is high and the recycling is available. The drawback is the lack of further design, and one cannot further modify the patterns. TEM grid shows high feature size which is lack of applications in optics and electronics. An optic grating can be a qualified candidate for LSI process, and these types of molds are not researched under LSI process before. Molds fabricated on silicon is ideal for fabricating high precision nanopatterns, as introduced in the previous part. Silicon with limited dimension is not ideal for fabricating hierarchical structures with complex feature combined. In addition, if silicon

is heavily etched via wet or dry process, the mold become too fragile to survive high-pressure LSI process because etched region can work as artificial defects which can be easily propagated along, eventually resulting in the catastrophic mold damages.

Table 2.1 Comparisons of mold types, resolution limits, and throughput

| **Mold Type** | **Resolution [μm]** | **Throughput** |
|---|---|---|
| Grids (TEM) | 7.5 | High |
| Grating (Optics) | 0.6 | High |
| Photolithography | 1.0 | High |
| EBL | 0.01 | Low |
| FIB | 0.1 | Low |
| NIL | 0.01 | Mid |

It is essential to develop a method of fabricating the mold with hierarchical structures in order to expand the LSI process to wider ranges of applications. In the following parts of the study, the development will be revealed.

# CHAPTER 3. CHARACTERIZATION TECHNIQUES

## 3.1 Optical Microscopy

An Optical microscope is the one that usually uses visible light and magnifies the target object. An eyepiece lens and an objective lens are coupled to magnify the object. The resolution limit is presented as equation 4 shows.

$$R = 0.61\frac{\lambda}{NA} \tag{4}$$

R is the resolution limit, λ is the wavelength, and NA is the numerical aperture. Numerical aperture is a measuring capability of gathering lights and resolving object details. It is the product of refractive index (n) and sine of half of the angular aperture, μ. Equation 5 shows the numerical aperture equation.

$$NA = n\sin\mu \tag{5}$$

For the objective lens in air, the half of angular aperture cannot exceed 60°. Thus NA of 0.87 is the limit in air. The resolution can be improved by increasing refractive index, therefore, oil-immersion NA is the solution to it, whose NA can reach 1.25 or higher [40].

There is a special mode in optical microscopy, named dark-field microscopy. It is a special one to block out the unscattered light and to collect scattered one to present the objective image. It is generally used in imaging transparent objectives such as cell and biomolecules. It is useful in this research to show grating-coupled plasmonic resonance. In this study, Olympus BX-51 Optical microscope was used to characterize the topology of microstructures and corresponding dark-field images.

## 3.2 Scanning Electron Microscopy (SEM)

SEM is an electron-based microscope to scan the target objective collecting information. By scanning along the sample surface, various types of carriers are emitted, including secondary electron (SE), back-scattering electrons (BSE), and X-ray, which are collected by detectors to determine the topography, crystalline orientation, elementary composition, and distribution. The resolution of SEM is much higher (~ 1nm) compared to

optical microscopy due to lower wavelength of the electron. The information collected by SEM is comprehensive. In addition to regular SEM, cryogenic electron microscopy (Cryo-EM) is used for special imaging. Basically, various types of leaves were observed under the electron microscope, but the high vacuum environment results in catastrophic damage to the microstructures. Thus, the cryogenic technique is used to preserve original structure by rapidly cooling down without creating solid water crystalline.

In this study, two types of EM were used. S-4800 Hitachi field emission SEM (FESEM) was used to observe micro/nanostructures. Cryo-EM (Nova Nano SEM, FEI) was employed to characterize preserved leaves structures.

## 3.3 Atomic Force Microscopy (AFM)

An AFM was firstly proposed and released by Binning and Quate from Stanford University and Gerber from IBM in 1986. The working principle is depicted in Figure 3.1. The AFM operation depends on force interaction between the tip and the sample surface [41,42]. The tip surface is proximity in the sample and the non-negligible force is transferred to the detector by a laser. It is a veritable topology characterization method without constraints of material types in terms of electrical conductivity, which is necessary for a scanning tunneling microscopy (STM).

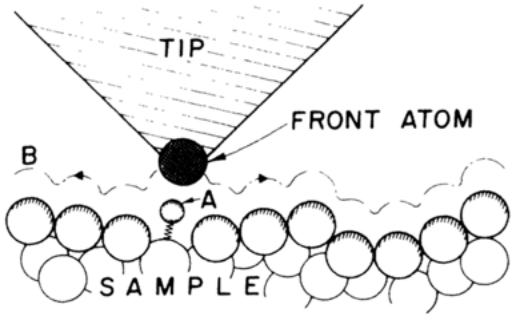


Figure 3.1 Working principle of operation of an AFM. Adapted from American Society of Physics. Ref. 42. Copyright 1986.

The resolution depends on the sharpness of the tip radius. The sharper of the tip is, the higher-resolution can be achieved. In addition, the scanning environment of vacuum gives a better resolution due to minimum environmental interference to the AFM cantilever. Depending on the cantilever motion, AFM scanning can be categorized in contact and AC

mode, and the latter is barely touching the sample surface, minimizing the potential damage to the sample. If the tip is replaced with magnetic materials[43], the magnetic force can be detected to characterize the magnetic domain distribution. Analogously, If the tip of the AFM is replaced from silicon to doped silicon or other conductive materials and working under the contact mode, it is applicable as measuring electrical properties [44,45], which is known as conductive AFM (C-AFM). Similarly, if the conductive tip is working under intermediate or non-contacting mode, it is able to measure the contact potential difference (CPD) as Figure 3.2 presents. This type of AFM is called Kelvin Probe Force Microscope (KPFM)[46].

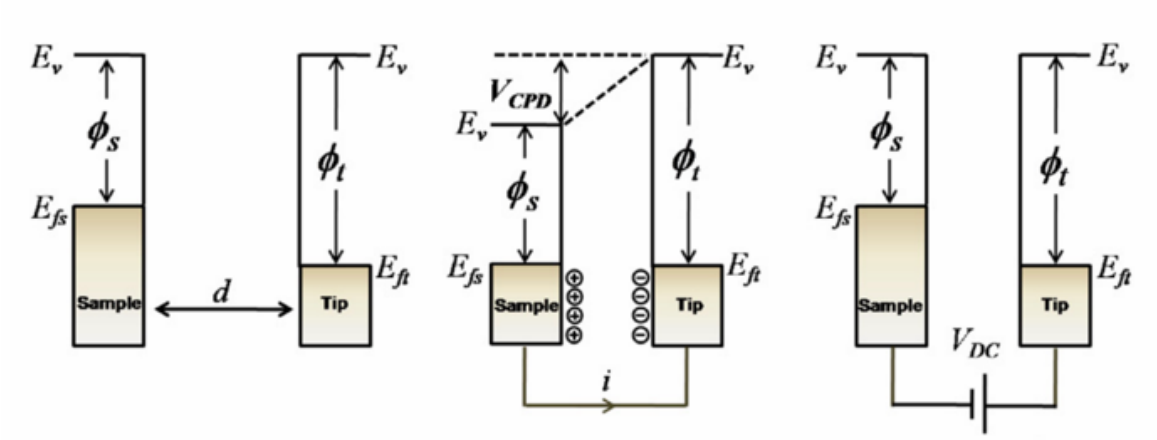


Figure 3.2 Working principle of KPFM. Adapted from Elsevier. Ref. [46]. Copyright 2011.

In this thesis, AFM (Veeco Dimension 3100) was used to acquire the high resolution AFM images under AC mode. The tip has a radius of 30 nm and the frequency is 250 KHz. KPFM (Asylum Research E) was used to measure the surface potential of the sample. The tip is coated with a conductive layer of Pt to ensure the electrical conductivity.

## 3.4 Low-noise current amplifier

The low-noise current amplifier is used to detect current signals in a sensitive manner. Instead of using a voltage amplifier, which might lead to unacceptable penalties

in frequency response and phase accuracy, the current amplifier can sink the current directly to null. The sensitivity can range from 1mA/V to 1 pA/V. In this study, the current amplifier (Stanford Research System Model SR570) is used to characterize the current generated from the LSI fabricated device. The high sensitivity of this equipment facilitates the measurement with lowest noise interference.

## 3.5 Goniometer

Sessile drop technique is used to characterize the solid surface energy. The major process is placing a droplet of the water on the solid surface, and the goniometer is used to measure the angle between a droplet and the solid surface[47,48]. Typically, the surface with high surface-energy gives low contact angle and vice versa. The goniometer includes light source, which is used to brighten the droplet to acquire clear texture of droplet, and CCD camera, which is used to capture the image of the droplet. In this study, a Ramé-Hart goniometer (Model 590) was used for measuring the static contact angle to qualitatively determine the surface energy.

## 3.6 X-ray Photoelectron Spectroscopy (XPS)

XPS is a powerful analytical technique to measure elementary composition. This technique is the study of electrons emitted from X-ray-irradiated compounds[49]. A target molecule or atom is bombarded with X-ray and ejects an electron[50]. In principle, all electrons with binding energy less than that of the exciting X-ray are ejected[51]. The binding energy is different depending on the atomic number and valence, thus XPS is a powerful technique to detect elements both in qualitatively and quantitively. Energy conservation for the photoemission process is shown following.

$$E_{h\nu} = E_k + E_\phi + E_B(i) \quad (6)$$

$E_{h\nu}$ is X-ray energy, $E_k$ is the kinetic energy of the photoelectron, $E_\phi$ is the correction part such as the work function, and $E_B$ (i) is the binding energy on the *i*th level.

In this research, Kratos XPS system detects existing elements of the fabricated device and determines the valence state of the surface element. Two type of detections are

performed, one is the wide window detection to acquire wide-ranged energy spectrum and the other is the high-resolution detection, which is used to determine the valence level.

## 3.7 Spectrometer

Spectrometer, or optical spectrometer, shows the intensity of light in a spectrum, usually from near-infrared (NIR) through visible (vis) to ultraviolet (UV). Depending on the layout, the reflection or absorption is measured. In this study, a dual beam system is used: one beam is used reference, and the other one is detecting light. Dual monochromators are identically used to spatially separate the light to increase the accuracy of the light. In this study, Lambda 950 model spectrometer was adopted to measure the spectrum from 2000 nm to 300 nm to observe the optical response of fabricated devices.

## 3.8 Conclusion

In this chapter, we reviewed characterization techniques and working principles for series of equipment. Topography was characterized using optical microscopes, SEM, and AFM. Electrical properties were measured using the current amplifiers and KPFM. Optical response was measured using the spectrometer. All measurements are repeated several times to ensure the repeatability, accuracy, and reliability.

# CHAPTER 4. LARGE-AREA DIRECT LASER SHOCK IMPRINTING OF 3D BIOMIMIC HIERARCHICAL METAL SURFACE FOR TRIBOELECTRIC NANOGENERATORS

## 4.1 Introduction

### 4.1.1 The demand for power generators

Scavenging environmental energy through sustainable approaches is promising not only to address the global energy issues but also to enable the self-powered operation for electronics and sensors in emerging technologies[52]. Various technologies have been developed to convert environmental energy into electricity through physical processes such as electrostatic, piezoelectric, and recently, triboelectric processes[5354]. Triboelectric nanogenerators (TENGs) show technological potential in efficiently harvesting mechanical energy through contact triboelectrification and electrostatic induction[55–60]. Major efforts in TENG research have been devoted to improving power generation by increasing triboelectrification surface area and engineering the surface properties. Fan et al. reported that the output of TENG highly depends on microstructured patterning[53,61]. Seol et al. claimed that higher packing density of micro/nanostructures results in better TENG performance[62]. The output performance can be modulated by modifying the electrode surface with different functional groups of SAMs, in that electrode functionalized with amine group shows superior output rather than other functional groups such as hydroxyl, ester, and chloro, when the other electrode is polytetrafluoroethylene (PTFE). The proposed interpretation for such output difference results from largest electronegativity difference between the amine group and fluorine group (from PTFE) rather than any other combination[63]. Micro/nanostructure engineering of polymer surface has been dominantly utilized for boosting the contact triboelectrification, with deposited metal electrodes for collecting the scavenged energy. Since high-quality metallic electrode on the backside of polymer domains is deposited in the final step of fabrication in these polymer-based TENGs to ensure their electrical connections to external electrical devices, it is inevitable to employ the high-cost process such as e-beam evaporation. Thus, it is necessary to explore an alternative approach to manufacture TENGs in a cost-effective manner. The cost of fabrication of TENGs is effectively saved if the sequence of process is reverse from

the currently adopted way. Typically, the process initiates from inexpensive metallic foil, such as Aluminum foil, then an insulating monolayer is self-assembled on it. Nevertheless, this state-of-the-art approach is limited by the vague potential for producing 3D hierarchical surface structures with conformable coverage of high-quality metal. Obstacles, such as the intricate fabrication and expensive machinery, concerning the economical and cost-effective production of TENGs with directly patterned metallic surfaces with 3D nanoscale structures by design continue to prevail.

### 4.1.2 LSI of TENG on soft templates

Fabricating metallic micro/nano-scale patterns have great potential applications for a variety of areas such as plasmonics[37] and electronics[64]. However, manufacturing metallic structures in a precise, large-scale, and three-dimensional way remains as a challenging task under currently used technology. Though reactive-ion etching (RIE), focused ion beam (FIB) present high-accuracy removal of materials, it is not an economical approach in term of time and cost to achieve fabricating three-dimensional structures[65,66]. On the other hand, additive manufacturing of metal is preferable in large-scale fabrication, but the challenging aspect of this process is resolution[67]. In 2014, Gao *et al.* developed an LSI process to enable crystalline nanoscale metallic structure in a large area[3]. The working principle is to trigger the superplastic flow of metal to be conformably deformed into a nanoscale mold with an ultra-high strain-rate process. To extend the fabrication into three-dimensional structures, it is necessary to seek a suitable mold to accomplish LSI process. Fortunately, soft-lithography can provide such molds with desirable dimension and accuracy. PDMS and SU-8 is a superior combination regarding replicating surface structures from various surfaces such as surface-machined silicon[68] and even natural surface[69]. However, imprinting of metal toward these soft molds is generally very challenging due to nature of softness as well as low-temperature resistance. It is well known that deformation of polymers is rate sensitive, with elasto-viscoplastic response to high-strain-rate deformation. Thus, these soft molds are applicable in LSI process in principle since within short laser pulses (<10 ns) the straining in polymers is developed much slower than the metallic materials under laser shock. The formability of metals is

high under the high-strain-rate deformation, which enables metals to flow into a soft mold with high-fidelity while the soft mold possibly remains its original shape. In addition, LSI process is a cold forming process in which the laser energy is absorbed by a protecting and ablative coating layer, and therefore effectively prevents thermal cracks of polymeric molds, which most likely occurs in traditional hot embossing. The LSI-enabled capability of conformably transfer of hierarchical microstructures from 3D natural leaves into metallic surface addresses the challenges of scalability, resolution, and hierarchical complexity simultaneously by combining high-strain-rate metal deformation and 3D soft mold (SU-8).

### 4.1.3 Water-driven TENG (Water-TENG)

Among the various categories in TENG family, water-TENG has been attracting growing attention due to the needs of sustainable and recyclable energy harvesting system[70]. Until now, there are several successful water-TENGs[71,72], and most of them require micro/nanostructures and hydrophobic surface to maximize the performance output. Interestingly, these two typical characteristics of high-density microstructures and hydrophobic (low surface energy) surface are analogically similar to structural and surficial properties in water-repellent leaves such as bamboo leaves[73] and lotus leaves[74], whose surfaces consist hierarchical surface structures with a dense coating of low-surface-energy waxing. This structural and chemical combination of hydrophobic leaves stem from long-term adaptation and evolution in semiaquatic environments. Mimicking the hierarchical microstructures and hydrophobicity from these natural templates into the water-TENG device is effective in terms of maximizing electrical performance because these hierarchical structures are desirable to improve the effective contact area between devices and water drops. In addition, hydrophobicity is another key factor in optimizing the performance of TENGs because the maximum effectiveness of water-TENGs occurs when the water drops are completely off from the device[75]. Since the metallic surface is intrinsically hydrophilic due to the existence of native oxide, it is necessary to modify the surface with low-surface-energy polymers, such as fluorinated silane, to complete this dual biomimetic approach.

In this chapter, we demonstrate a scalable laser-based metal replication from the soft mold, conformably transferring the features from natural template to metallic sheet. Targeting natural templates are a dehydrated 'Bamboo' *Indocalamus Longiauritus* leaf (BB), *Iris* leaf (IRS), 'Northern Starburst' *Rhododendron* (NSR), and 'Japanese Stewartia' *Stewartia Pseudocamella* (SP), which were selected with respective microstructure size from small to large and with respective packing density from high to low. In addition, the wettability was further tuned by coating different surface-energy silanes, such as 1H,1H,2H,2H-Perfluorooctyltrichlorosilane (PFTS), octyltrichlorosilane (OTS) and N-(6-aminohexyl)-3-aminomethylethoxysilane (AHAMTES). The contribution from patterned features as well as functionalized silanes toward resultant triboelectric performance was systematically studied. Furthermore, to better understand the linkage between the functional group and water-TENG performance, the surface potentials were measured using Kelvin probe force microscope (KPFM). Lastly, finite element method (FEM) was developed to validate the morphological findings. This work provides a new route of manufacturing scalable large area bioinspired micro/nanoscale patterns on metal surface with designed functionality, and open ways to engineering the surface energy and nanostructures for many applications such as energy, electronics, surface plasmon resonance, biochips and bioplasmonic, etc.

## 4.2 Experimental methods

### 4.2.1 Replication of biomimic structure on metal from the soft mold by LSI

Figure 4.1 (a) to (e) schematically illustrate the LSI process. A naturally dehydrated bamboo leaf and fresh leaves from IRS, NSR, and SP (Figure 2 (a1) to (d1), respectively) were picked around West Lafayette campus (Indiana, USA), then placed in the dish, with the back of leaves bonded to it. PDMS (Sylgard 184, Dow Corning) was cast into the dish to mold the leaves, with the mass ratio between the base monomer and curing agent of 10: 1. Followed by degassing process, the dish was placed on the hot plate at the temperature of 345 K for 1 h to accelerate the curing. Since the geometry of PDMS master mold is the complementary to that of the original leaf, this master mold is negative in geometry. Then, few drops of SU-8 5 (MicroChem) were dipped on the glass slide. PDMS master mold,

with feature-side facing down, toward where SU-8 drops were placed, leaving mold filled with SU-8. Flood exposure (MJB-3, SUSS MicroTec) (wavelength of 365 nm, the power of 10 mW) was conducted for 10 min to cure SU-8 completely. This positive-geometry SU-8 template was ultrasonically cleaned under SU-8 developer, followed by isopropyl alcohol (IPA) rinsing to completely remove uncured SU-8 residual. The dimension of the final SU-8 mold is around 20 mm x 20 mm. LSI process was performed on free-standing Al foils (Lebow Company) according to our previously demonstrated method[3] with a minor modification. A laser beam with 3-mm diameter irradiates the ablation layer of a 4-μm-thick Al foil with graphite (Asbury Carbons) sprayed on. Under the intense laser irradiation (Q-switch Nd:YAG laser, 1064-nm wavelength, 5-ns pulse duration, the effective pulse energy is ~ 200 mJ) (Continuum® Surelite III), the graphite is instantaneously evaporated thus generating the ionized plasma as well as strong momentum. Confined within a glass slide on top, this shock wave was transferred downwards the targeted Al foil placing on SU-8 mold, conformably replicating the positive geometry into Al foil. Fabricating the foil with the area of 20 mm x 20 mm requires fifty pulses of irradiations, which combine stepper motor controllers (Thorlabs) to cover the whole desired area.

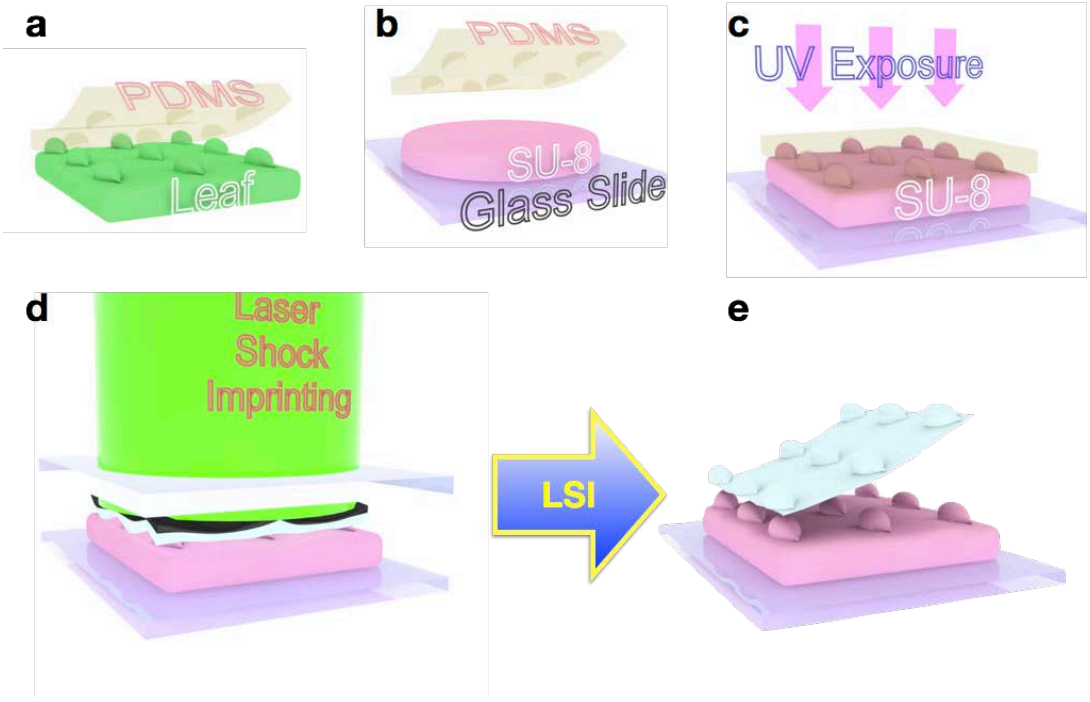


Figure 4.1 Schematics of the soft mold fabrication and LSI process

### 4.2.2 Surface functionalization of micro/nanoscale biomimic metal structures

Three pieces of identically fabricated Al foils were $O_2$-plasma (Plasmatech) treated under the flow rate of 30 sccm, the bias of 50 W, and the pressure of 100 mTorr. This process is helpful to create hydroxyl (-OH) group on the surface of Al foil, facilitating the three different types of SAM coating. The coating process was slightly modified from the coating on PDMS[76] and silicon wafer[77]. The foils were immersed in three different silane solutions. The used silanes here are PFTS (1mM, Gelest®), OTS (1mM, Gelest®), and AHAMTES (10mM, Gelest®). The coating process was the same for three different silanes except that AHAMTES requires moderate temperature (345 K) rather than room temperature. After finishing the coating, the foils were rinsed with toluene, IPA, and deionized (DI) water to remove any physically adsorbed silanes. Drying the foils at the temperature of 385K under the inert atmosphere is helpful to orient the chains of SAM effectively[78]. The final products of water-TENGs are presented in Figure 4.2.

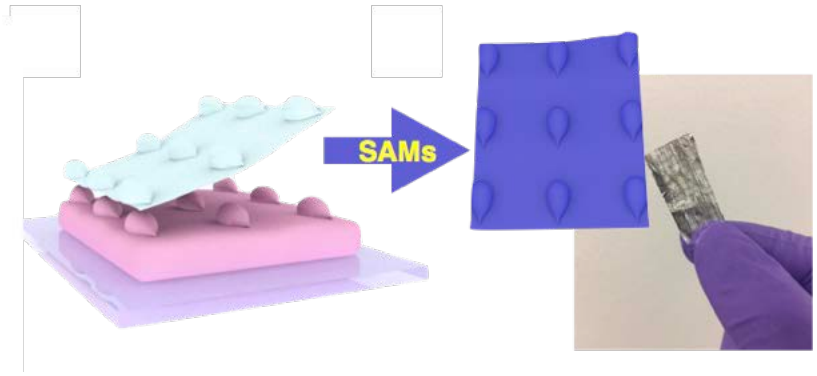


Figure 4.2 Surface functionalization of a fabricated metallic membrane

### 4.2.3 Characterizations

Two types of scanning electron microscopes (SEM) were employed in these series of characterization. Cyro-SEM (Nova NanoSEM, FEI) was utilized to characterize the morphologies for leaves, and field emission SEM (FESEM) was then used to observe the topologies of the SU-8, and LSI/Al foils. Kratos X-ray photoelectron spectroscopy (XPS) system determines the existing elements of the fabricated water-TENG device. Static contact angles were measured using a Ramé-Hart goniometer (Model 590). Surface

potentials were collected via Nap mode in KPFM (Cypher, Asylum Research). The electrical outputs of fabricated devices were measured using a low noise current preamplifier (Stanford Research System Model SR570) when providing a constant rate of water drop using a programmable syringe.

## 4.3 Results and Discussion

### 4.3.1 Pattern transferring from natural leaves to metallic foils

Figure 4.2 shows the side-by-side comparison of four different leaves for each stage of the replication process. BB and IRS show apparently different surface properties compared to NSR, and SP leaves regarding wettability. Relatively high contact angles (> 130 ˚) for formers while the relatively low contact angles (< 70 ˚) for latters. One of the possible interpretations of the contact angle discrepancy would be the presence of microstructures from the leaf surface. It is well-known that multi-scale microstructures mainly contribute to self-cleaning of leaves, and this contribution is evident from replicated SU-8 mold shown from the 3rd column in Figure 4.2 that much cleaner surfaces are found with fewer dust on BB and IRS leaves than the other two. It is worth mentioning that though microstructures are helpful to increase the contact angle, the chemical component of the surface is also critical regarding surface wettability. According to the previous report[74], low-surface-energy diols are found on the surface of hydrophobic plants' leaves. In addition, Shomer-Ilan et al.'s work[79] shows that certain plants with high hardiness would generate acid amino after low-temperature exposure, increasing hydrophilicity. Therefore, low contact angles from NSR and SP could probably result not only from the morphology but also from high-energy surfaces themselves.

Replication from PDMS to SU-8 is facile mainly because of good wettability between two materials, so is the peel-off process, because creating irreversible bonding between them is thermodynamically infeasible merely under UV irradiation or heating without introducing extra functional groups[68]. Good wettability and facile detachments between PDMS and SU-8 contribute to high-fidelity surface transfer from natural template to SU-8 mold. In the following strategy, pristine Al film is subjected to instantaneous high pressure and temperature generated from LSI process, resulting in conformable

deformation against SU-8 mold. The final products are presented in the 4$^{th}$ columns of Figure 4.3. This process does not involve either obvious distortions of shapes or damages to Al foil due to the superplastic flow of Al toward to mold, triggered by laser-induced high-strain-rate deformation. From our previous work, LSI technique is employed to generate sub-10-nm nanostructures by imprinting the metallic sheet against Si wafer on which nanoscale patterns were sophisticatedly fabricated using E-beam lithography[3,37]. To expand this technique to a broader way of applications such as three-dimensional geometry fabrication on the metallic sheet, both PDMS and SU-8 raise as candidates because they could effectively address the encountered issues of scalability and conformability during transferring substrate. SU-8 is considered to be a better candidate as a mold during LSI process because of the superior mechanical property regarding higher Young's modulus of SU-8 (~ 2 GPa) compared to the counterpart of PDMS (~ 10 MPa)[4]. Soft PDMS mold, therefore, cannot sustain the shape during the deformation of Al foil, thus causing shape distortion after LSI. Deformed Al foils show similar shapes of microstructures and geometry because of the good sustention from the SU-8 mold. Though harder mold is beneficial for creating better-fidelity micro-features, it is not preferable to carbonize SU-8 mold because it would result in decreasing the ductility of SU-8, eventually, breaks during the laser shock imprinting process. Simulation describing this high-strain-rate deformation process is discussed in the later part of this chapter.

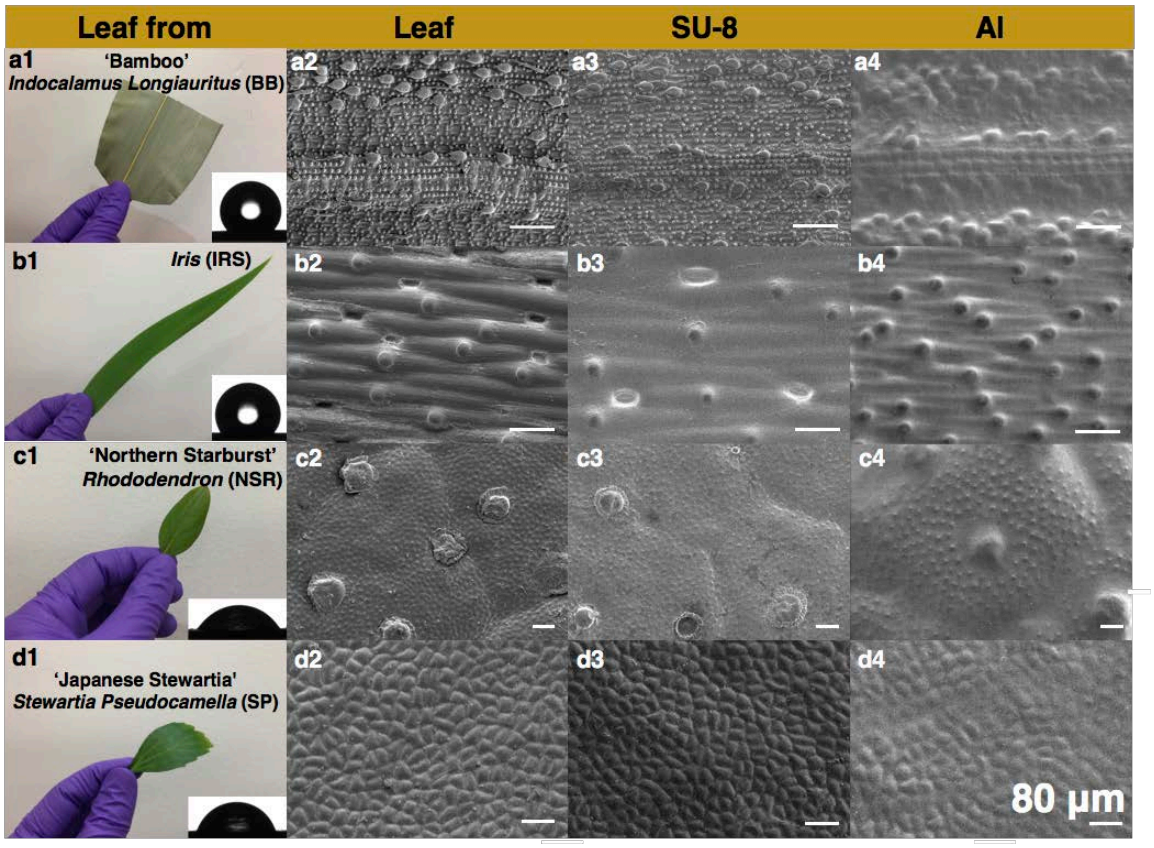


Figure 4.3 Leaves from (a1) Bamboo (BB), (b1) Irish (IRS), (c1) Northern Starburst (NSR) and (d1) Japanese Stewartia (SP). Their respective contact angle measurement (inset) and SEM images of original leaves are presented from (a2) to (d2), respective SEM images of SU-8 shown from (a3) to (d3), and respective SEM images of LSI/Al listed from (a4) to (d4). (Scale bar: 80 µm)

### 4.3.2 Mechanism of structured metal with hydrophobic coating as water-TENG devices

After transferring the features on Aluminum, the surface wettability is attempted to be mimicked. For instance, original BB leaves show hydrophobicity. However, Aluminum is hydrophilic due to the existing oxide layer on the surface. PFTS is coated on laser-shock-imprinted Al foil (LSI/Al) to modify surface wettability from hydrophilicity to hydrophobicity as the tails of PFTS, trifluoromethyl ($CF_3$-), could provide a low-energy surface. Hydrophobicity is a desirable surface property for the water-TENG device as the maximum power occurs only after the water drops are completely off the device[72]. The working mechanism is majorly summarized into two types: electrostatic induction and triboelectricity[70]. Due to sliding between water drops and the device surface, the device

surface is negatively charged while the water drop is positively charged due to the difference of electron affinity. When the droplet is from the surface, the device surface remains negatively charged (Figure 4.4(a)), and the same amount of positive charges electrically nullify the device. As the following droplet is fed, negative charges attract counter-ions from the droplet to form an electrical double layer (EDL), generating positive potential difference (Figure 4.4(b)). Electrons flow from the ground the device until reaching the equilibrium (Figure 4.4(c)). Again, the water drop slides off from the device (Figure 4.4(d)), the electron flow to the ground to become the electrical neutralization. Therefore, this water-TENG continuously collect the energy as the droplet is fed periodically.

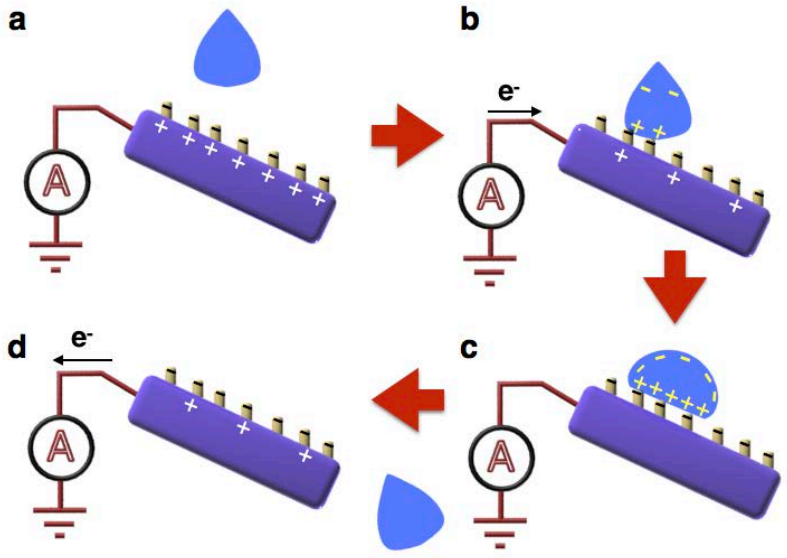


Figure 4.4 (a) Surface is negatively charged after several droplets passed, (b) and (c) electrons flow into the device as the EDL is created, and (d) electrons flow to the ground when the droplet leaves off the device.

The electrical output is evaluated for this PFTS-coated and BB-patterned LSI/Al (PFTS/BB/Al). The experimental setup shows how all-metal water-TENG device works as it collects the triboelectric energy from water droplets. Figure 4.5(a) shows the electrical characterization with the voltage output and the short-circuit current density ($J_{sc}$). Both

outputs present a good periodicity as the droplets are sliding along the device surface. Positive tiny peaks occur on each periodicity in voltage output and current density, indicating electrons transfer into the device. As droplets leave off the device, significant opposite-signed peaks are observed in both outputs. The amplitudes are 1V and 0.4 mA $m^{-2}$ for voltage output and $J_{sc}$, respectively. The electrical power output of this device was estimated when connected to a variety of external loads. As shown in Figure 4.5(b), the output power gradually rises when connected to resistances from 100 MΩ to 1 GΩ, then drops down as the resistance decreases. Maximum areal power output is around 15 μW $m^{-2}$ with the external load of 1 GΩ. It is interesting to find that, Aluminum, after the LSI, shows improved voltage and current output, as shown in Figure 4.5(c) and (d). An in-situ monitoring of the voltage during continuous water droplet flowing was demonstrated. Despite types of patterns imprinted, the output enhancements are found in both output signals compared to their pristine counterpart. When identically imprinted Al (LSI/Al) samples are chemically modified with PFTS and performed the electrical output test, significant improvements in both voltage and current outputs in BB-patterned-LSI/Al (BB/Al). It is worth mentioning that original BB has very high density of extruded microstructures (~ 2.5 x $10^5$ /$cm^2$ for 3-μm-feature and ~ 1.4 x $10^4$ /$cm^2$ for 30-μm-feature) and well-aligned packing rather than the others. This combination of high-density and aligned structures probably contribute to higher chances of sliding between water drops and the device. The other patterns with surface modification cannot achieve such output improvement might result from following reasons: First, packing density is not high enough for IRS patterns (~ 6.2 x $10^3$ /$cm^2$ for 20-μm-feature), providing lower chances of sliding between the droplet and sliding surface. Second, the packing densities for NSR and SP are comparable to BB. However, the features on these leaves are not as extruded as ones on BB, thus the friction is not critically changed. This also leads to an interpretation of the phenomenon, where there is no significant improvement of both outputs are seen among the different patterns imprinted Al, that the size of the contacted area between droplets and non-chemically modified surface, with a low contact angle, is too large to “count” the imprinted features. When the contact area is reduced due to the high contact angle, the smaller feature size and packing density are then more critical to generating higher electrical performance.

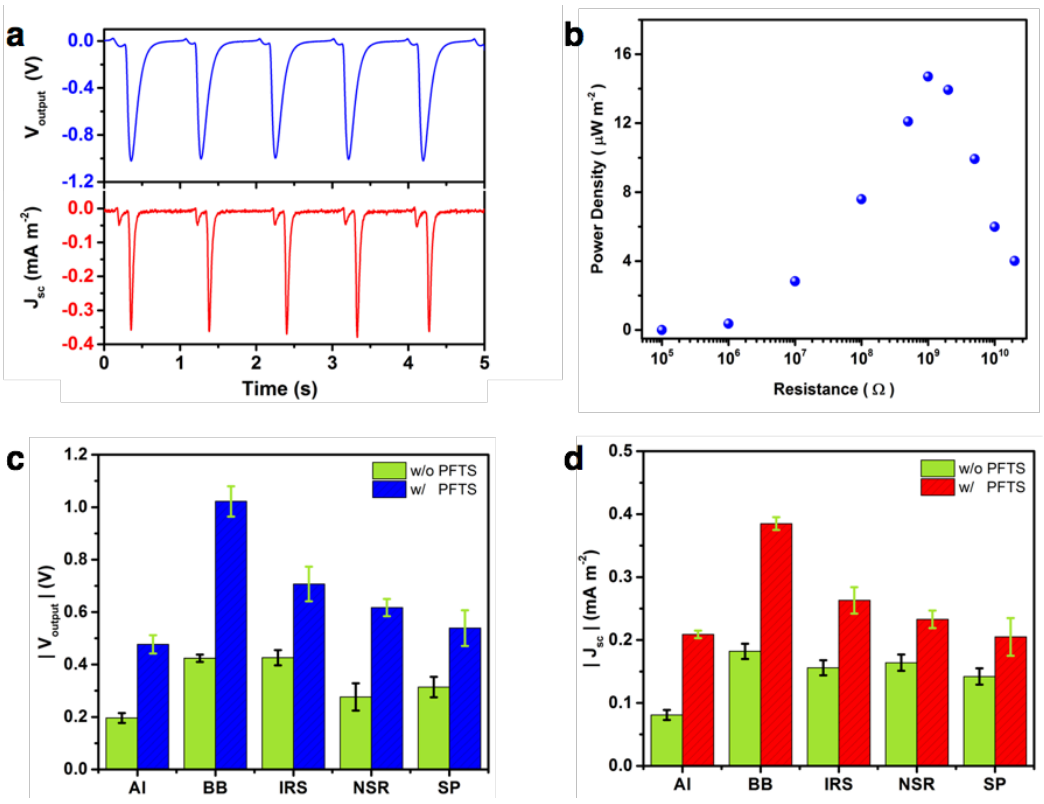


Figure 4.5 (a) PFTS/LSI/Al voltage output(blue) and short-circuit current density (red) when droplets are periodically fed, (b) Power density from PFTS/LSI/Al with external load connected, (c) absolute voltage output comparison among non-LSI-processed and different LSI-processed leaves (green and non-shaded) and corresponding devices with PFTS coated (blue and shaded), and (d) absolute short-circuit current density comparison among non-LSI-processed and different LSI-processed leaves (green and non-shaded) and corresponding devices with PFTS coated (red and shaded).

### 4.3.3 Modulation of wettability of bamboo metal structures through SAM coatings

To further modulate the surface wettability of BB/Al and to understand the impact from chemical component toward the resultant electrical output, extra two silanes, OTS, and AHAMTES were used. OTS has the similar electron affinity as PFTS, while AHAMTES shows opposite tendency. By choosing these two types of silanes with opposite electronegativity, surface wettability is expected to be modulated from the hydrophobic to the hydrophilic. Therefore, after the morphologies are conformably transferred from leaves into metal, two opposite types of surface wettability of leaves are mimicked. OTS and AHAMTES were chosen with the similar chain length bonded to the silanol (-Si-O-) after successful assemble to aluminum, which was confirmed by XPS results in Figure 4.6.

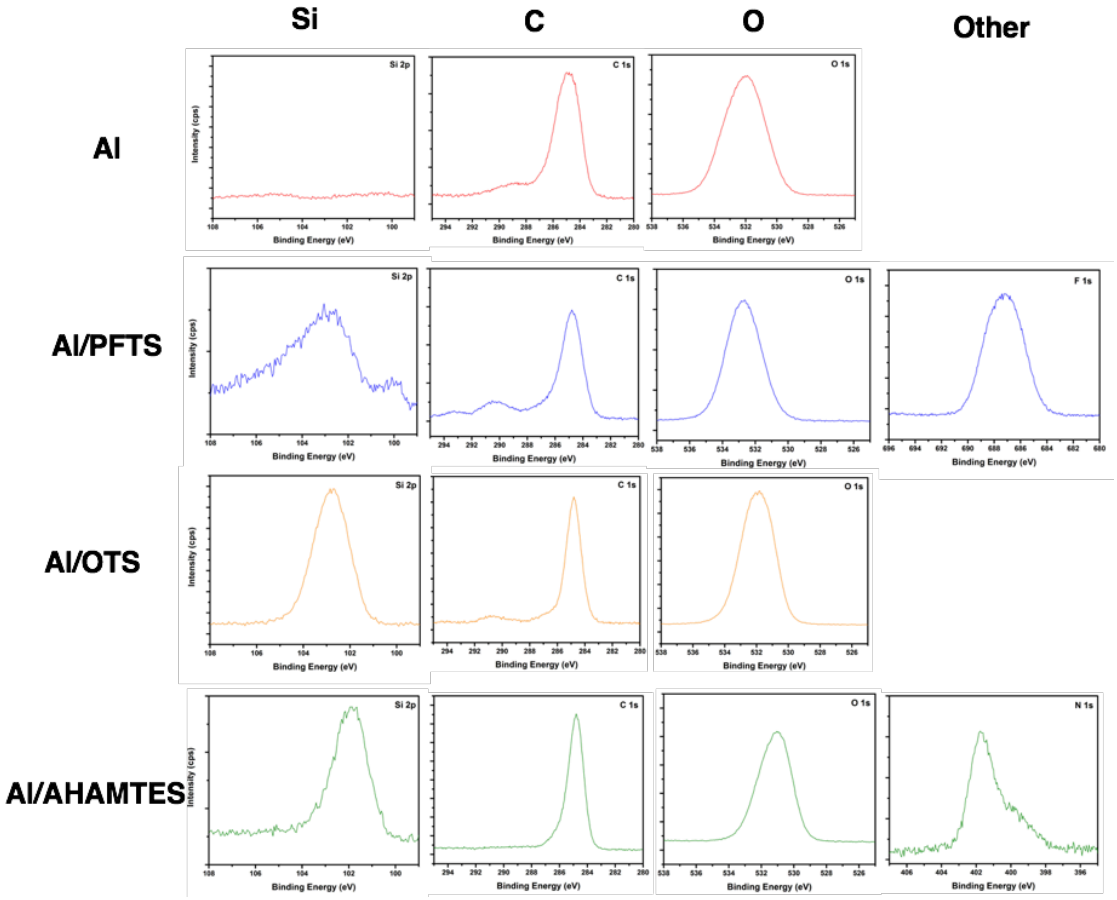


Figure 4.6 XPS spectroscopy for Al (red), Al/PFTS (blue), Al/OTS (yellow), and Al/AHAMTES (green).

The major difference of PFTS, OTS, and AHAMTES is the tail component of each chain, which are trifluoromethyl ($CF_3$-), methyl ($CH_3$-), and amine group ($NH_2$-), respectively. These typical functional groups are present in Figure 4.6 as well. The possibility of the existence of adsorbed SAMs was low because that all the coated samples were vigorously rinsed by series of solvents. Another direct evidence for successful coating of silanes is shown as contact angle changes in Figure 4.7 (a) (on the top of each bar), obvious contact angle differences (~ 105 °, ~ 95 °, and ~ 45 ° for PFTS/Al, OTS/Al, and AHAMTES/Al, respectively) were observed among the different coatings, which confirm the surface energy contributions from SAMs, especially the functional groups on chain ends. Note that the contact angle for pristine Al foil is ~ 80 °. It should be noted that, though the aluminum surfaces were introduced with microstructures before coatings, it does not

make significant changes to those foils without LSI because the microstructure sizes do not reach nanoscale.

### 4.3.4 Effects of SAM coatings on triboelectric outputs from bamboo metal structure

Voltage output was measured using the same set-up mentioned above, however, in this case; it was normalized by the sliding area for each device based on the base contact area (the circular area between the bottom of drop and foil surface). Figure 4.7(a) shows PFTS/BB/Al dominates the performance among all the devices. AHAMTES coating does not show as high output as the other two, unlike the previously reported work where amine-terminated contact-mode TENG[63] is superior regarding overall electrical performance, indicating that TENG device is highly material-dependent. In the contact-mode TENG, two materials listed far from each other in triboelectric table [59] are selected, while note that in this work, one of the "working electrode" is a water drop. Thus, it requires separate and independent analysis. To analyze the output discrepancy on three types of SAMs, the surface potentials were characterized using KPFM. As shown in Figure 4.7(b), the tip (Pt (100) coated on Si) approaches the functionalized Al surface with the distance of 50 nm on each round of potential scanning. Keeping the Al foil grounded, a voltage is applied to the cantilever to nullify the potential difference of Fermi level between the tip and the substrate, known as the contact potential difference ($V_{CPD}$)[80]. A negative $V_{CPD}$ is applied to the tip when the Fermi level of tip is lower than that of the functionalized Al to compensate the Fermi level difference, or relatively lowering the vacuum level of the functionalized substrate, and *vice versa*. It is the water drop that primarily slides along the functionalized LSI-Al foil, the interpretation of output differences among different functionalization is probably behind the work function difference. According to the previous report [63], the maximum output of contact-mode TENG occurs at the device containing amine group against fluorinated ethylene propylene. This phenomenon most likely results from the largest electronegativity discrepancy between the amine group and fluorinated-terminated functional group, which could be deducted from $V_{CPD}$, high $V_{CPD}$ refer to more vacuum level decrease from cantilever (Pt). $V_{CPD}$ versus Pt tip for each functionalized substrate is presented in blue bars in Figure 4.7(c). As it is challenging to determine the work function

of water, the reported work function drop[81] of 1.2 eV from Pt vacuum level, when water is attaching to it, is taken into consideration. The red bars in Figure 4.7(c) shows the vacuum level difference to water vacuum level (Ø $H_2O$ vac.). The sequence of normalized output from high to low is PFTS, OTS, and AHAMTES. This tendency is the same as the vacuum level difference between functionalized Al and water, as shown in red bars from Figure 4.7(c). The further two vacuum levels locate, the higher output was achieved. Such vacuum level changes are resulting from the dipole moment of different SAMs. It is deduced that the surface potential difference for each SAM layer correlates the overall TENG output. From the previous reports [82,83], fluorinated alkaline silanes and alkaline silanes exhibit the dipole moment towards the surface, leaving the head part of SAMs positive thus pulling the vacuum level downward depending on the scale and direction of the dipole moment. Amine group-contain silanes, however, shows opposite dipole moment, thus leaving the tails negative and the vacuum level for the aluminum part is lifted. Simplified band diagram visualizes these surficial changes in Figure 4.7(d). Because of the existing dipole moments from SAMs, electrons are easily transferring from water to PFTS/Al, while the transportation is the relatively difficult from water to AHAMTES due to the lifted vacuum level from Al side.

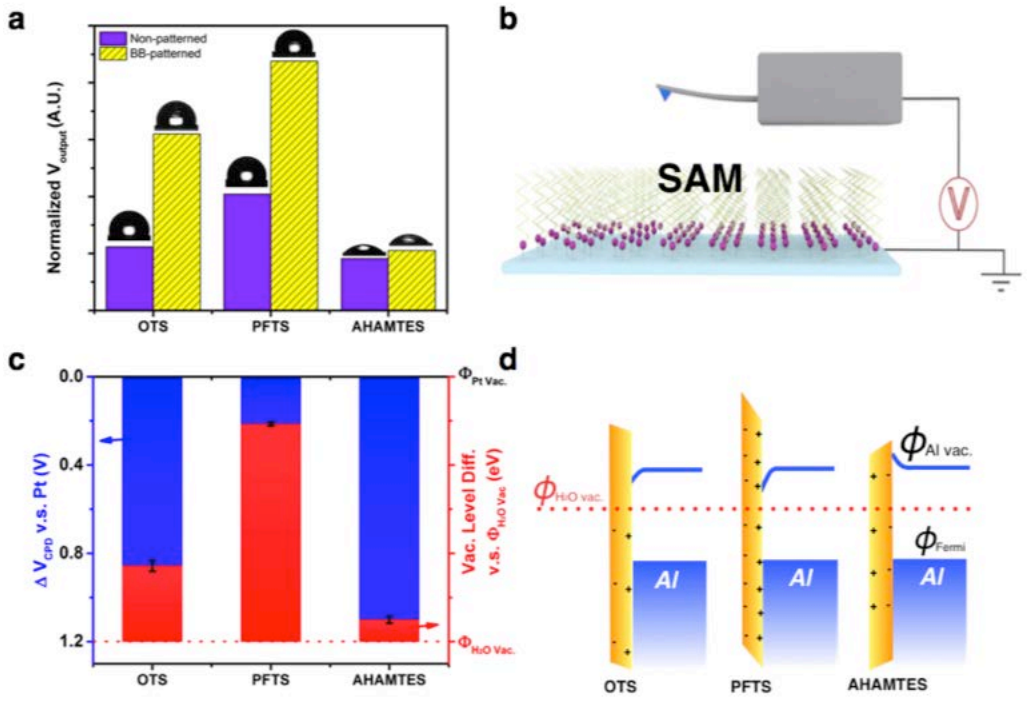


Figure 4.7 (a) Normalized voltage output comparison among three different SAM-coated devices with (yellow and shaded) and without (purple and non-shaded) LSI-processed (BB-patterned), (b) scheme of simplified KPFM setup with SAM-coated Al foil. (c) Contact potential drops versus Pt tip for three different SAM-coatings (blue) and corresponding vacuum level differences above water vacuum level (red), and (d) Simplified band diagrams of three different SAM-coated Al foils (blue line).

### 4.3.5 Mechanics of laser shock imprinting of metal against soft SU-8 mold

To better understand deformation in metal foil against soft SU-8 mold, a 2D plane strain FEM was used to simulate the LSI process. Note that due to the difference in terms of mechanical behavior between Aluminum and SU-8, two numerical models were used in this simulation. As discussed above, the conformable deformation of aluminum is resulting from the high strain rate exceeding $10^6$ $s^{-1}$. Thus, Johnson-Cook (J-C) strain-rate sensitive plasticity model was applied to Aluminum foil to validate the experimental findings. J-C model is presented in the following equation,

$$\bar{\sigma} = (A + B\bar{\varepsilon}^n)\left[1 + C\ln\frac{\dot{\varepsilon}}{\dot{\varepsilon}_0}\right](1 - \theta^{*m}) \quad (7)$$

where $\bar{\sigma}$ is the equivalent yield strength, $\dot{\varepsilon}$ is the plastic strain rate, A is the nominal yield strength at reference strain rate, $\dot{\varepsilon}_0$, B, and n are the work hardening parameters. C

represents strain-rate dependence and m represents temperature dependence and $\theta^* = (\theta - \theta_0)/(\theta_{melt} - \theta_0)$. J-C model constants and other material properties used in the simulation for Aluminum are listed below[37] in Table 4.1:

Table 4.1 Material Parameters for Aluminum

| Property | Value |
|---|---|
| **Density (g cm$^{-3}$)** | 2.7 |
| **Young's Modulus (GPa)** | 36 |
| **Poisson's Ratio** | 0.33 |
| **Specific Heat Capacity (J g$^{-3}$ $^{o}$C$^{-1}$)** | 0.90 |
| **Coefficient of thermal expansion (K$^{-1}$)** | $14.2 \times 10^{-6}$ |
| **Thermal Conductivity (Wm$^{-1}$ K$^{-1}$)** | 237 |
| **Initial Yield Stress, A (MPa)** | 140 |
| **Hardening modulus, B (MPa)** | 157 |
| **Strain rate dependence, C** | 0.016 |
| **Work hardening exponent, n** | 0.167 |
| **Thermal softening exponent, m** | 1.7 |
| **Transition Temperature, $\theta_0$ (K)** | 800 |

For simplifying the model, as well as lack of reported work regarding viscoelastic behaviors of SU-8, Neo-Hookean hyperelastic model was adopted for numerically capturing mechanical behavior of SU-8 to account for compressibility with strain energy formulation given as follows,

$$U = \sum_{i=1}^{N} \frac{2\mu_i}{\alpha_i^2}\left[\lambda_1^{\alpha_i} + \lambda_2^{\alpha_i} + \lambda_3^{\alpha_i} - 3 + \frac{1}{\beta_i}\left(J_{el}^{-\alpha_i\beta_i} - 1\right)\right] \quad (8)$$

where μ is the shear modulus and J is the volume change. This form of strain energy potential is in polynomial representation used in ABAQUS where parameter N can go up to 6 (N is usually set below 2 when first two invariants are defined. In this case, N is taken as 1) $\lambda_1$ $\lambda_2$, and $\lambda_3$ are the principal stretches, $\alpha = 2$ and $\beta = (\nu/1 - 2\nu)$, where ν is passion

ratio. The initial shear modulus and bulk modulus are given by $\mu_0=2C_{10}$ and $K_0=2/D_1$ where $C_{10}$ and $D_1$ are temperature dependent material parameters defined to be 1.625 GPa and $1.247x10^{-8}$ $m^2/N^3$, respectively, for SU-8[84].

4-μm Aluminum foil is placed on the SU-8 mold, which has a hemisphere-like structure dimensionally similar to the bamboo's papillae. Strain distributions on Aluminum and SU-8 molds are presented in Figure 4.8(a), before LSI, and in Figure 4.8(b), after LSI applied. The imprinting process generates strain distribution depending on the geometry, where the edge (region I in Figure 4.8 (a)) has higher strain than strains at the top of the feature (region II in Figure 4.8 (b)), resulting in conformable feature-transferring. It is also shown from Figure 4.8 (b) that compressive strains (~ 3%) are distributed on the upper region of SU-8 mold, which might set obstacles on zero-distortion transfer of substrate. However, this minor distortion does not have any issues on transferring most hierarchical micro-features from leaves to metals. To systematically study resolution limit for this soft-mold LSI, regular-shaped patterns, such as trenches and square arrays, with a variety of dimensions are studied. As Figure 4.9 shows, both trenches and arrays were successfully deformed using SU-8 molds. As the dimension is reduced, the sharpness of features begins less clear compared to larger-feature cases. To better understand this tendency, a numerical model with 2D FEM was conducted. When the deformation initiates, as shown in Figure 4.8 (c), the foil is subjected to a variety of stress concentration depending on the position, where higher stress is concentrated on upper corners of the mold. Suspended parts of Aluminum contact to the flat features because these areas are free from any impedance, while the deformation starts at the regions near molds' upper corners, as seen from Figure 4.8 (d). Finally, Figure 4.8 (e) shows the completion of deformation of Aluminum foil while leaving the reduction of thickness near molds' corners, which is a direct evidence of the plastic deformation. It is also clearly presented that the corners of molds in tilted downward, which may cause a minor distortion from perfect feature-transfer. Theses tilting phenomena set obstacles for soft-mold LSI from generating sub-100nm patterns. Current set-up can reach the resolution of ~ 1um, as shown features in Figure 4.3 (a4).

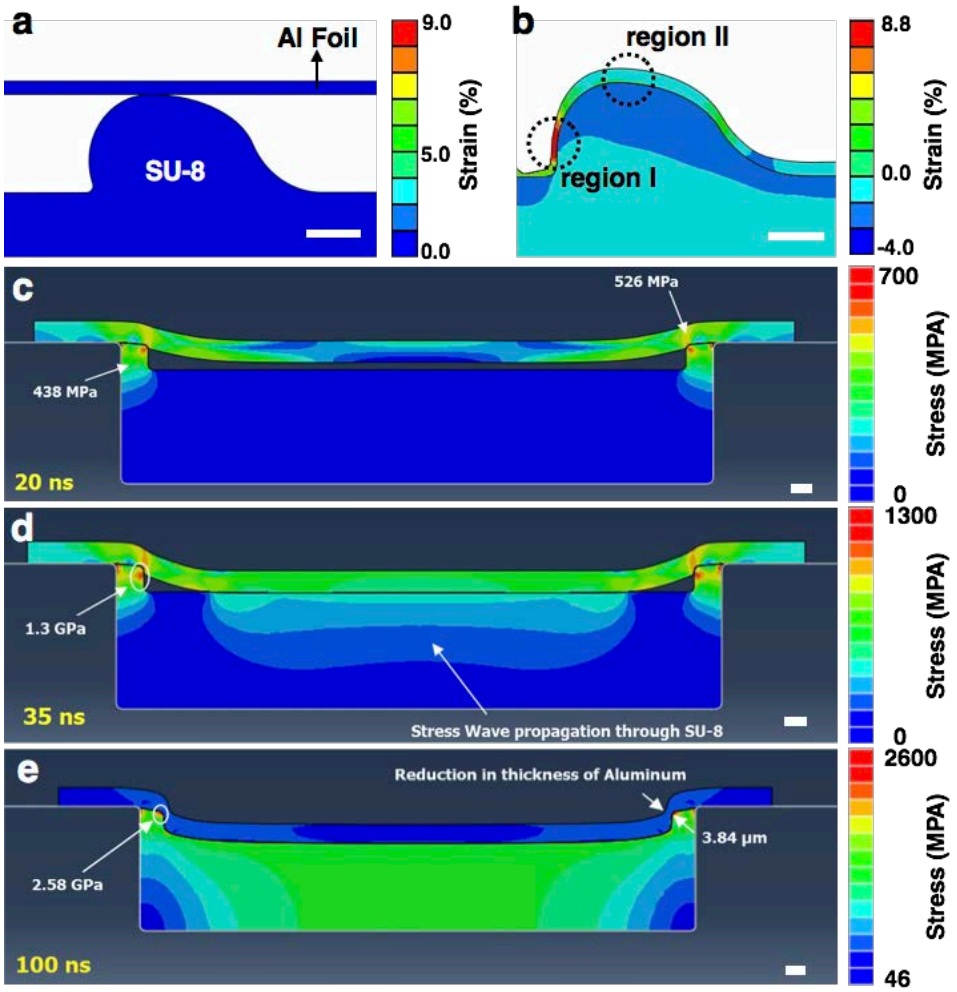


Figure 4.8 Schematics of (a) Al foil is placed on a microstructure of SU-8 before LSI, (Scale bar: 10µm) (b) strain distribution of the system after LSI, (Scale bar: 10µm) and stress field distributions for Al- SU-8 trench system during LSI: (c) initial stage, (d) developed stage, and (e) final stage. (Scale bar: 4µm)

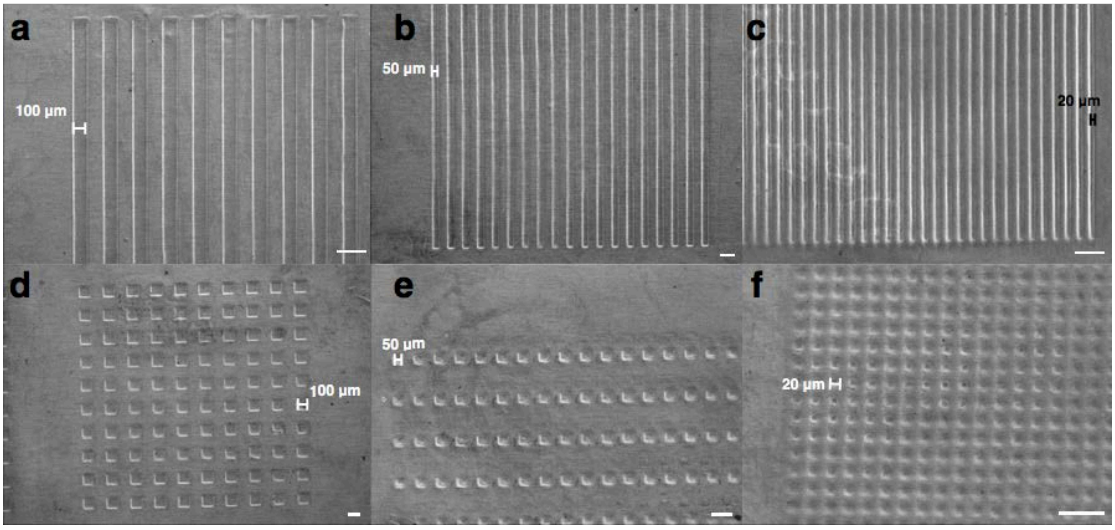


Figure 4.9 LSI/Al with features of (a) 100-µm, (b) 50-µm, and (c) 20-µm trenches as well as (d) 100-µm, (b) 50-µm, and (c) 20-µm squares. (Scale bar: 100 µm)

It is worth mentioning that this hard metal forming against soft mold is feasible through LSI for the following reason: LSI can induce high-strain-rate deformation in Aluminium due to its superplasticity at high strain rate, while SU-8 is a viscoelastic material whose response of strain to the stress is much slower than metal within a few nanoseconds under high-strain-rate process in LSI. In addition, as the nanosecond laser irradiation is absorbed by an ablative coating on top of metal to generate confined shock wave and propagating through the metal foil and mold, the process results in an ultrafast and mostly cold deformation in metal without thermal effects, the SU-8 mold avoids catastrophic damages (Figure 4.10 (a) and (b)) after LSI, which is much better than other processes, such as hot pressing and casting, resulting from continuous high temperature and pressure. Only minor elevation (~ 730 nm, 7% to original thickness) of the thickness of SU-8 mold was observed as shown in Figure 4.10 (c), which is probably due to the detachment of SU-8 from the glass slide after high stress applied from LSI.

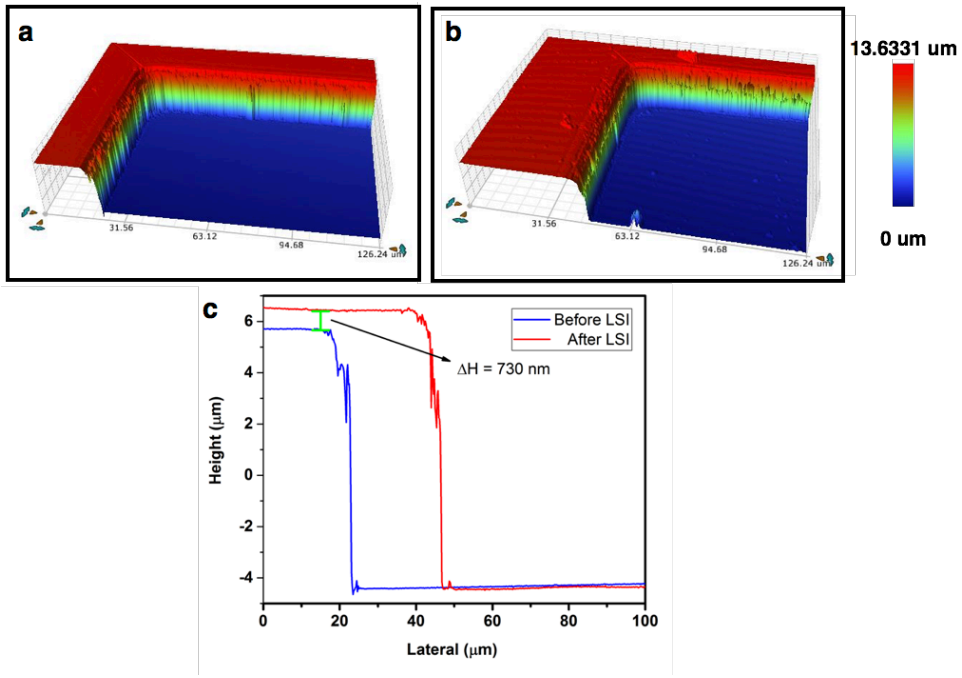


Figure 4.10 Surface profile before (a) and (b) after the LSI. (c) Lateral profile comparison for before (blue) and after (red) LSI.

## 4.4 Conclusion

In summary, An effective route of making a biomimic metal surface in both morphology and chemical functionalization is present in this study. LSI is capable of large-scale, three dimensional, and high-fidelity fabrication of hierarchical biomimic micro/nanoscale metallic structures. This technique is fully compatible with optical lithography and soft lithography. SAMs coating is used to modulate the wettability of metallic surface from hydrophobic to hydrophilic depending on the terminated functional groups. The contribution from patterned features as well as functionalized silanes toward resultant triboelectric performance was systematically studied. In the performance evaluation of water-TENG device, it is realized that both micro-sized structures and the high-density nanostructures are beneficial in overall triboelectric output. Furthermore, the surface potentials were measured using KPFM to understand the linkage between the functional group and water-TENG performance. Another key factor to further maximize the water-TENG output is the modulation of vacuum level to ease electron transfer from water by introducing dipole moment from SAM. Our approach opens doors to new

manufacturable TENG technologies for economically feasible and ecologically friendly production of functional devices with the directly-patterned 3D biomimic metallic surface in energy, electronics, and sensor applications.

# CHAPTER 5. LASER-INDUCED ASCALAVLE FABRICATION OF NANOPHOTONIC PATTERNS USING LOW-COST OPTICAL DISCS

## 5.1 Introduction

### 5.1.1 Issues on current lithography

Designing and fabricating nanostructures are under continuous investigations in a variety of areas such as plasmonics[6], biosensors[85], and electronics[5]. Large-area fabrication of such nanostructures with high accuracy [12,86,87], tunability [88–90], as well as hierarchy [91], remains as a significant challenge. Nanoimprint lithography (NIL)[92] is a useful technique which consists of deforming thermoplastics or UV-curable resists under thermal or photonic control. This process developed from a single-imprinting to a successive-imprinting method on the same region, generating complex hierarchical structures [93,94] by combining different molds to achieve multiband and omnidirectional optical properties[95]. However, the thermo-rheological nature of polymer resists beyond the glass transition temperature ($T_g$) set the obstacle for fabricating hierarchical nanostructures by deforming polymers through a consecutive nanoimprinting[16].It was reported that patterned polymer resists such as polystyrene suffers from relaxation as the temperature increases[96]. Though sophisticatedly prepared mold with hierarchy succeeds such fabrication, sequential spin-coating of polymer resist as well as reactive-ion etching (RIE) of such molds is not cost-effective[97]. In addition to the difficulty of fabricating hierarchical polymer patterns[98], the transfer step from polymer to metallic structures requires extra processing steps of high-vacuum RIE and e-beam evaporation[99].

### 5.1.2 LSI process as the alternative

It is essential to develop a cost-effective and large-area approach for hierarchical metallic nanostructures which can effectively simplify the process and reduce the cost of fabrication. One major challenge of fabricating high-quality metallic arrays is inducing high-strain-rate superplasticity[100] in metals. Conventional methods of shaping metal cannot provide sufficient strain rate to succeed this process. Fortunately, LSI presents a cost-

effective direct nanoimprinting of metal under high strain rate[3]. This laser-based approach is versatile in terms of adapting to the current technology of fabrications. By employing silicon mold fabricated via e-beam lithography and dry etching, LSI can successfully imprint metallic foil down to 10-nm scale[3,33] to enable excellent plasmonic and sensing applications. Besides, by using soft SU-8 mold fabricated via soft lithography and optical lithography, it transfers hierarchical micro/nanostructures from natural leaves into aluminum foils to be used as triboelectric nanogenetrators[101]. Goswami et. al. successfully combined of LSI technique and roll-to-roll to demonstrate the potential of LSI as a scalable, low-cost, and high-throughput process. Previously, this imprinting technique only focused on the high-fidelity transfer from sophisticatedly-made molds (e.g., silicon, SU-8, and hard epoxy) to metallic foils. Furthermore, these molds cannot balance between reliability and cost. For example, silicon molds are excellent in generating robust patterns while the cost is high as it involves the high-vacuum process of evaporation and dry etching. Polymer molds, on the other hand, are cost-effective but they suffers from the robustness of patterns. Thus, it is worthwhile to establish the LSI process using robust and low-cost molds, while keeping its capability of generating hierarchical nanostructures.

### 5.1.3 Template candidates with reliability and accuracy

Optical discs, such as compact disc (CD), digital versatile disc (DVD), and Blu-ray (BR), are candidates for LSI molds because of their economic availability, structural consistency and mechanical reliability[102,103]. A blank optical disc, with labels peeled off, consists of many radial grooves on both sides: the label side and the pure polymer side. The major polymer component of optical discs is polycarbonate (PC), which is proved to be a strain-rate dependent material[104], exhibiting stronger and tougher mechanical property under high-strain-rate process. Moreover, the label side consists identical radial grooves except a thin layer of reflective metals, such as gold, silver, nickel, and aluminum.

In this chapter, we start the study from qualifying two LSI mold candidates, the one with metal deposited and the one without. This side-by-side comparison reveals the superior imprinting conformability of the imprinted foil due to the mechanical stability from the metal-deposited PC layer, which is further numerically validated via finite

element methods (FEM). The imprinted nanophotonic patterns excite surface plasmon through grating-coupled surface plasmon resonances. The efficiency of this resonances can be tuned by the depth of patterns, which was modulated by the applied laser intensity. Furthermore, surface plasmon resonances at multiple bands were systematically studied by varying the width of 1D-periodic disc mold. In addition, the rotation of molds between every step during SLSI achieves hierarchical micro/nanostructures, which is optically responsive in multiple direction and band. Eventually, Rigorous Coupled-Wave Analysis (RCWA) was employed to validate the optical findings of such structures. SLSI is an advantageous metal-patterning process which can effectively simplify the fabrication set-up, i.e. from the vacuum to the ambient, significantly reduce the processing time by using the fast nano-second laser, and generate smooth and high fidelity nanophotonic patterns in a cost-effective and high throughput manner.

## 5.2 Experimental method

### 5.2.1 Preparations of SLSI molds from optical discs

Commercially available optical discs (CD, DVD, and BR from Verbatim) were used as SLSI molds. Typically in CD, acrylic labels were peeled from the disc, and the reflective metallic layer remains at the acrylic label side, while the rest of discs consist of PC layer. These molds were rinsed with alcohol to remove the coated dyes and dried under the nitrogen gas flow. Note that in the case of DVD, both upper and lower parts of molds are made of polycarbonate except for the lower part deposited with a reflective metallic layer. Similarly, in the case of BR, a protective polymer layer was delaminated from the original mold, remaining the reflective metallic layer on the PC layer.

### 5.2.2 Fabrication of Plasmonic arrays on Al foils

A free-standing Al foil (Lebow company) with a graphite-sprayed sacrificial Al foil was placed on top of the mold and confined using a pair of borosilicate glasses (Mcmaster Inc.) Then, Nd: YAG laser (1064-nm wavelength, 5-ns pulse duration, Continuum) irradiated to ablate the sacrificial graphite layer, generating a strong momentum during ionized plasma is created[33] . A single pulsed laser can fabricate a foil with an area of 13 x

13 $mm^2$. SLSI processes were performed by rotating molds at angles to fabricate a more complex pattern. Detailed process will be discussed in the section of results and discussions.

### 5.2.3 Characterization of plasmonic arrays on Al foils

Optical microscope (Olympus) was used to observe the distribution of patterns. Metrology of the plasmonic patterns was characterized by atomic force microscope (AFM) (Veeco, Digital Instruments). The optical properties of SLSI-ed Al were acquired by a spectrometer (Lambda 950, PerkinElmer), whose default incident angle is 8°.

### 5.2.4 Numerical simulation

A Maxwell's equations solver[105], S4, is employed to simulate the reflectivity for SLSI-ed Al. Finite element method (FEM) (ABAQUS) is used to validate the experimental findings of mechanical displacement of metallic foils. Typically, Johnson-Cook strain-rate sensitive plasticity model[106] was used to metallics foils as well as disc molds.

2D plane strain finite element method was used to simulate the mechanical behavior during LSI process. As discussed in the main text, the ultimate goal of this simulation is to directly compare the imprinting process for metal foil as well as molds with and without the deposited reflective layer. As the strain rate induced by laser ablation is above $10^6$ $s^{-1}$, Johnson-Cook strain-rate sensitive plasticity model was feasible for the simulation[106]. This model is presented in the following equation,

$$\bar{\sigma} = (A + B\bar{\varepsilon}^n)\left[1 + C\ln\frac{\dot{\varepsilon}}{\dot{\varepsilon}_0}\right](1 - \theta^{*m}) \quad (7)$$

where $\bar{\sigma}$, $\dot{\varepsilon}$ , A , $\dot{\varepsilon}_0$,B, and n is the yield strength, plastic strain rate, nominal yield strength, reference strain rate, and work hardening parameters, respectively. C and m correspond to strain-rate dependence and temperature dependence, respectively. θ*is equal to $(\theta - \theta_0)/(\theta_{melt} - \theta_0)$, where $\theta_0$ and $\theta_{melt}$ is transition temperature and melting temperature, respectively. Model Constants and other material parameters used are listed in the table below[37,107] in Table 5.1.

Table 5.1 Material parameters for Al, Au, and PC

| Property | Al | PC | Au |
|---|---|---|---|
| **Density (g $cm^{-3}$)** | 2.7 | 1.197 | 19.3 |
| **Young's Modulus (GPa)** | 69 | 2.54 | 79 |
| **Poisson's Ratio** | 0.33 | 0.344 | 0.42 |
| **Specific Heat Capacity (J $g^{-3}$ $^oC^{-1}$)** | 0.90 | 1.3 | 0.16 |
| **Thermal Conductivity ($Wm^{-1}$ $K^{-1}$)** | 237 | 0.19 | 318 |
| **Initial Yield Stress, A (MPa)** | 140 | 75.8 | 120 |
| **Hardening modulus, B (MPa)** | 157 | 68.9 | 243 |
| **Strain rate dependence, C** | 0.016 | 0.052 | 0.056 |
| **Work hardening exponent, n** | 0.167 | 1 | 0.147 |
| **Thermal softening exponent, m** | 1.7 | 1.85 | 0 |
| **Transition Temperature, $\theta_0$ (K)** | 800 | 420.15 | 296.15 |

## 5.3 Results and Discussion

### 5.3.1 SLSI process for creating intricate patterns of nanostructures

The DVD mold is shown in Figure 5.1(a), and this mold was tailored to the size of 2 cm x 2 cm. A typical LSI set-up is presented in Figure 5.1(b). A thin Al foil, with a graphite-sprayed sacrificial layer, is mounted on the aforementioned disc mold, then the set-up was tightly confined using a pair of glass slides. A fast nano-second laser irradiated the sacrificial graphite layer. Due to the extremely high energy of laser (power density ~ 1GW/$cm^2$) absorbed by the graphite, it induces the ablation of the graphite layer, generating a shock wave that propagates through the metal foil and deforms it against the underneath mold. The peak pressure of this shock wave can reach ~ 1GPa[3]. The output product of Al foil is shown in Figure 5.1(c), showing a large-area rainbow-colored foil after series of one-pulse irradiation. SLSI consist of a series of sequential LSI on the same Al foil, rotating the mold at the certain angle ($\theta_r$) between every LSI step. Figure 5.1($d_1$) to ($f_1$) schematically illustrate SLSI process. Typically, simple trenches were patterned through a single LSI of a metal foil into the mold. After rotating the mold at a certain angle ($\theta_r = 60°$), the second step of LSI is proceeded to generate pixel arrays. Lastly, another step of mold rotation and LSI can generate triangular nanoblock patterns. Corresponding topological characterizations of the pattern product on each step AFM are presented in Figure 5.1($d_2$) to ($f_2$). Similarly, triangular nanoblocks with different scales are fabricated by changing the

type of mold to CD (Figure 5.1(g)) and BR (Figure 5.1(h)). In the following session, a comprehensive study of the mold selection, tunability of SLSI is presented.

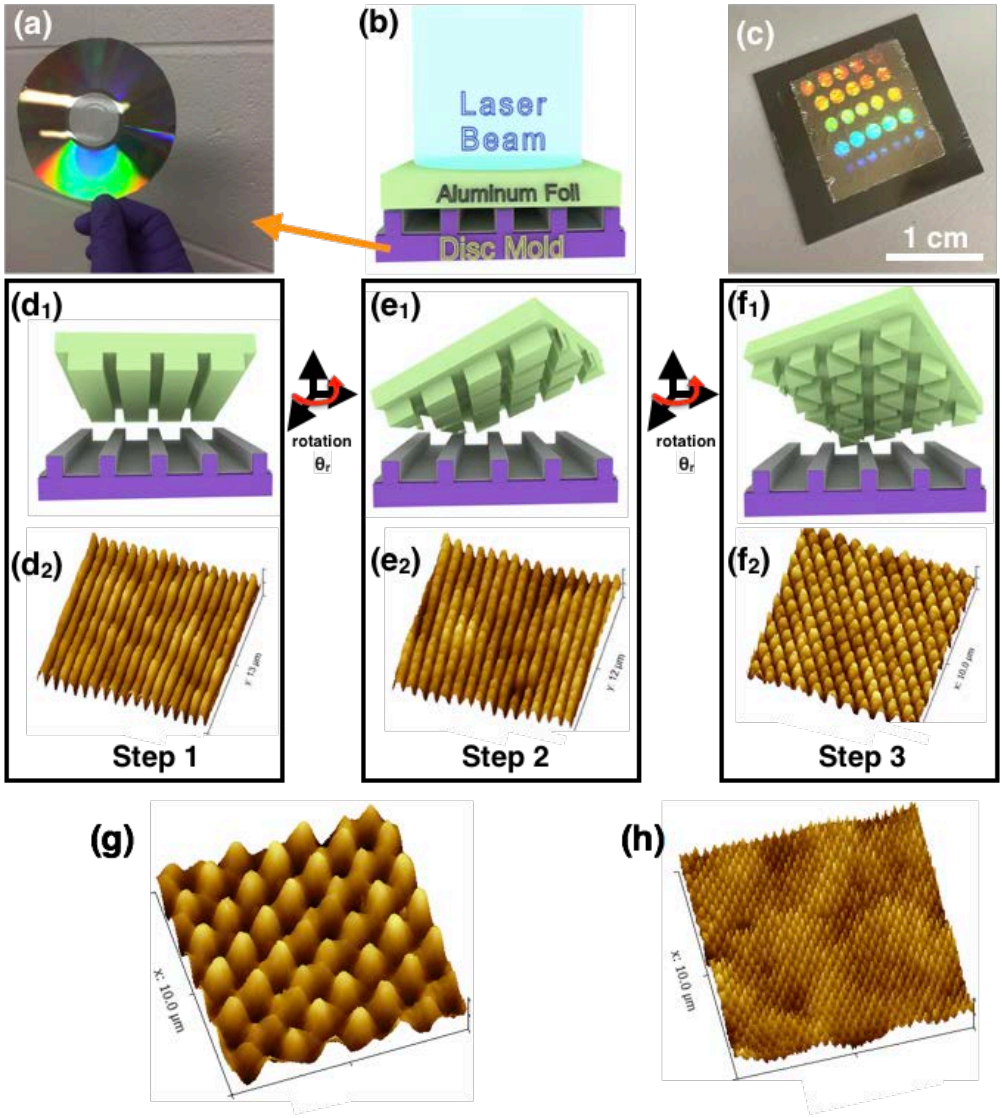


Figure 5.1 (a) Peeled-off optical disc mold (P8), (b) schematic illustration of LSI set-up, (c) LSI-ed arrays on Al foil mounted on a wafer, scale bar 1cm. Schematic illustration of LSI-ed metal foil using P8 mold after ($d_1$) 1st imprinting process, ($e_1$) 2$^{nd}$ imprinting process with angle rotation ($\theta_r$) , ($f_1$) 3$^{rd}$ imprinting process with another angle rotation ($\theta_r$) , and corresponding 3D AFM images of ($d_2$) trenches generated by single LSI,($e_2$) pixel arrays generated by double SLSI, and ($f_2$) triangular nanoblocks generated by triple SLSI. (g) triangular nanoblocks after triple SLSI using P16 molds, (h) triangular nanoblocks after triple SLSI using P3 molds.

### 5.3.2 The selection of molds and the modulation of depth via laser energy

Two types of molds are delaminated from a single DVD: a PC layer with metal deposited (metal/PC), and the other without. Both molds are majorly made of PC, which shows strain-rate dependency as well as strain-hardening property according to the reported work [108]. Therefore, both types of PCs are potential candidates for LSI molds. To qualify for a better mold candidate, both mold candidates were used to deform Al foils via LSI process. Figure 5.2(a) exhibits surface profiles for LSI-ed Al foil under two types of mold: metal/PC (blue) and PC (red). PC-used trenches exhibit the depth of ~ 10nm, while the metal/PC-used ones show the depth of ~ 40 nm. In addition, the inset image of Figure 5.2(a) can distinguish the better fidelity imprinting effect from the case of the metal/PC-used. FEM is studied to investigate the role of the metal layer on PC. Figure 5.2(c) shows deformations after a single LSI process on the Al foil and the PC mold, while Figure 5.2(b) shows counterparts on the Al foil and the metal/PC mold. The initial frontlines are marked as dashed lines in both Figure 5.2(b) and 5.2(c). When the metal is absent from the mold, the soft PC layer cannot effectively hold the shape for Al, thus leaving limited plastic deformation on Al foil. Major deformation occurs on the PC layer rather than Al foil. Therefore, the original sinusoidal geometry of the PC mold is severely distorted after a shockwave passed. In contrast, the metal layer, in the case of metal/PC-used one, would hold the shape of the original mold, thus the sinusoidal geometry is transferred from the metal/PC layer to the Al foil. Another key evidence for conformal geometrical transfer is the less deformed PC layer underneath the Au layer. Due to the existence of the Au layer, the deformation is majorly condensed on the Al. These simulation results are consistent with the experimental observations, where the metal/PC mold behaves superior in terms of imprinting conformability. Therefore, in the following sessions, all metalic foils would be imprinted using metal-deposited molds. Afterward, CD, DVD, BR molds are denoted as P16, P8, and P3, respectively, where the numbers are from the respective periodicity divided by 100 nm. Their respective imprinted foils are denoted as Al_P16, Al_P8, and Al_P3.

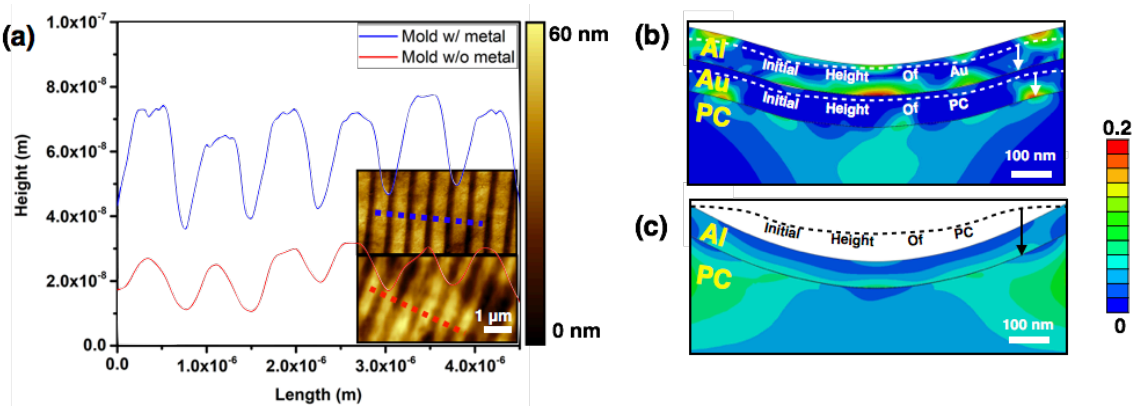


Figure 5.2 (a) Surface profiles for Al using two different mold conditions: (1) LSI using metal/PC mold (blue) and (2) LSI using PC mold (red), inset: (top) AFM images for LSI_Al using condition (1) and (bottom) using condition (2). Strain distributions for set-up: (b) LSI using metal/PC mold and (c) LSI using PC mold.

Imprinting depth can be tuned via laser energy. As Figure 5.3(a) presents, higher laser energy not only increases the imprinting depth but also improves the imprinting fidelity. The intrinsic roughness on Al foil gradually decreases, and the texture of gratings are more clear as the applied laser power is elevated. The imprinted grating structures can excite surface plasmon waves on the metal via grating-coupled surface plasmon resonance[109], which results in the improved absorption at a certain wavelength. This coupling efficiency is correlated with various factors such as trench depth[110] and quality factor[111]. In general, the higher absorption, or lower reflection, is performed at the metal surface due to the improved coupling efficiency. The correlation between applied laser energy and imprinted depth is summarized in Figure 5.3(b), where the depth of trench gradually increases from 3 to 60 nm, resulting in the gradual decrease in terms of reflectivity from 82% to 73% at the wavelength of 853 nm. This tendency of increasing resonant coupling efficiency with increasing depth was confirmed by S4 simulation, shown in the red dashed line in Figure 5.3(b). The discrepancy between measured and simulated reflectivity might result from the geometrical difference of trenches, where imprinted trenches tend to be sinusoidal while the simulated trenches were assigned with vertical walls and sharp fillets[111]. It is worthwhile mentioning that the depth of trench cannot reach a maximum of mold trench (100 nm for P8 mold) because the major component of mold, polycarbonate, whose Young's modulus is relatively low, is compressed under the generated high pressure, resulting in reduced space for Al foil to be imprinted through.

Though high-strain-rate compression makes polycarbonate harder, the inherently low Young's modulus cannot provide enough stiffness to imprint Al foil completely to the original depth of mold, which has been indicated from FEM study on Figure 5.2(b). According to our repeated experiments, LSI could reach 60% depth of the original mold.

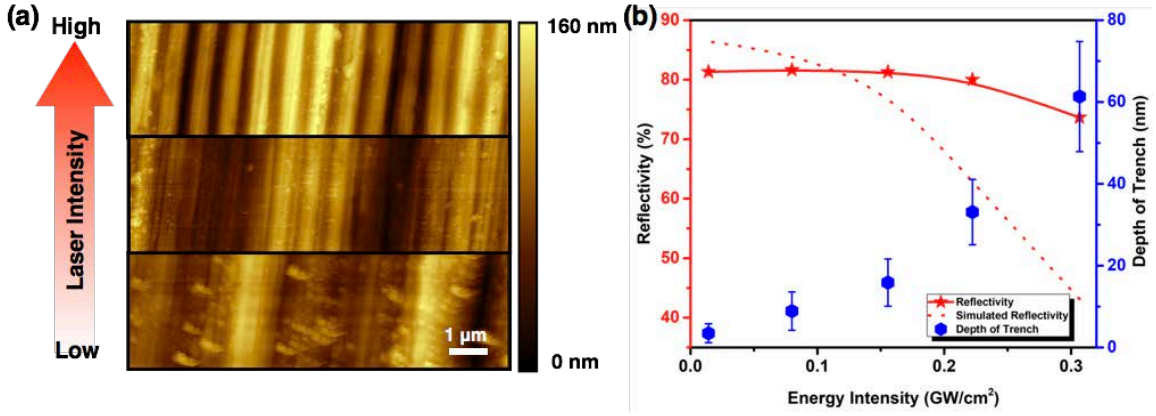


Figure 5.3 (a) AFM images showing morphological changes as the laser energy is modulated, (b) Laser modulation of depth of trenches (blue hexagonal) measured (red stars) and simulated reflectivity (red-dashed line) for Al_P16.

Analogously, the modulation of depth was successfully achieved using the narrower P3 mold (depth of 20 nm) as illustrated in Figure 5.4(a). A similar correlation between laser energy and imprinted depth as well as conformability was observed. Depicted in the Figure 5.4(b), the imprinted depth gradually increases from 3 nm to 12 nm as the energy dose increases. Higher energy dose required for LSI process in P3 mold compared to its counterpart in P8 mold, one speculate the possibility that grain size effect of foil increases the difficulty in plastic flow into smaller gaps. In addition, the higher contact areas between foil and molds might play a similar role in term of mechanical reluctance during this process. It is worthwhile mentioning the difficulties in linking the imprinted depth to grating coupling efficiency in Al_P3. Firstly, the imprinted depth for Al_P3 is comparable to the intrinsic roughness for foil, as a result, distinguishing periodic patterns inherently rough surface is challenging. Secondly, the shallow depth of less than 20 nm additionally make the optical detection more difficult. Therefore, an overall efficiency of grating-coupling of Al_P3 is relatively low. Selecting deeper mold when processing LSI would effectively address such issues.

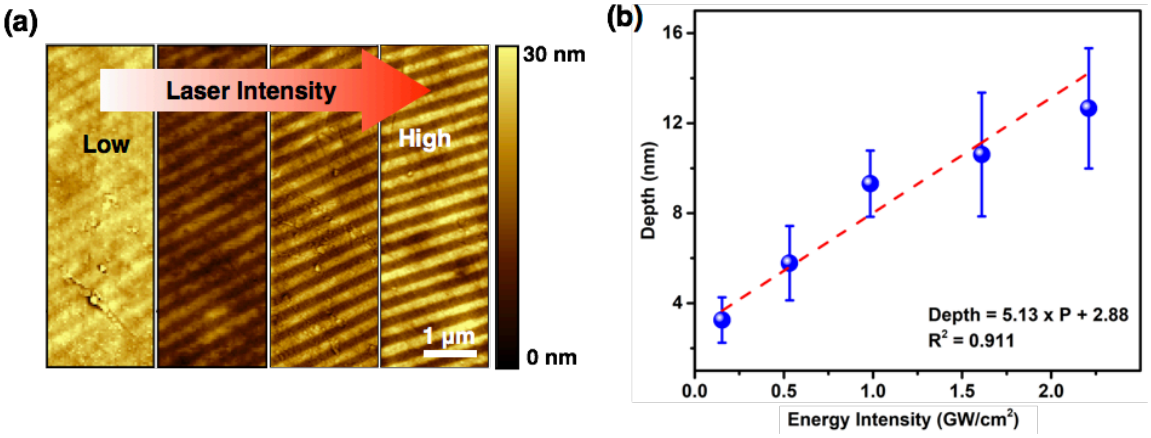


Figure 5.4 (a) AFM images of laser-modulated gradual surficial fidelity change in Al_P3, (b) Laser modulation of depth of trenches for Al_P3

### 5.3.3 Imprinting of trenches with the different width

The width of LSI-ed trenches is determined by the selection of original optical disc molds. The periodicity of trenches varies from 1600 nm, 740 nm, and 320 nm for, CD (P16), DVD (P8), and BR (P3), respectively. Figure 5.5 (a) to (c) show the fabricated foils with a variety of width. LSI provides a large-scale and uniform imprinting over foils as presented in inset figure of Figure 5.5(d). The Fast-Fourier-transformed (FFT) image (inset of Figure 5.5(c)) indicates the uniformity of imprinting throughout Al_P3, where the typical distance from the closest dot to the center is ~ 3.02 $\mu m^{-1}$, which is the inverse of a typical periodicity of 320 nm in P3 mold. It was reported that grating periodicity in one direction couples incident p-polarized modes only to surface plasmon polariton modes [6,112]. The set-up for the reflectivity characterization is schematically presented in Figure 5.5 (d), where the incident angle ($\theta_i$) of 8° and the incident plane of this non-polarized light is perpendicular to the grating direction, where the magnetic field is aligned with the grating direction. Imprinting of Al towards three major types of disc molds were conducted, and their corresponding optical responses are presented in Figure 5.5 (e). Interestingly, the resonance wavelength is expected by the periodicities of molds. Typically, Al_P16 shows dips at 1281 and 1686 nm in the reflectance spectrum; Al_P8 shows dips at 635 and 853 nm, and Al_P3 show a single dip at 366 nm. These pairs of decreased reflectance are due to grating-coupled plasmon resonance. Polarization effect of incident light is investigated,

and the resultant reflectance spectrum is comparable in case of non-polarization and p-polarization, as presented in Figure 5.6 (a). Under this optic setup of orientation, s-polarized light does not resonate with surface plasmon, because the magnetic field of incident light is not aligned with the direction of gratings, as shown in Figure 5.6 (c).

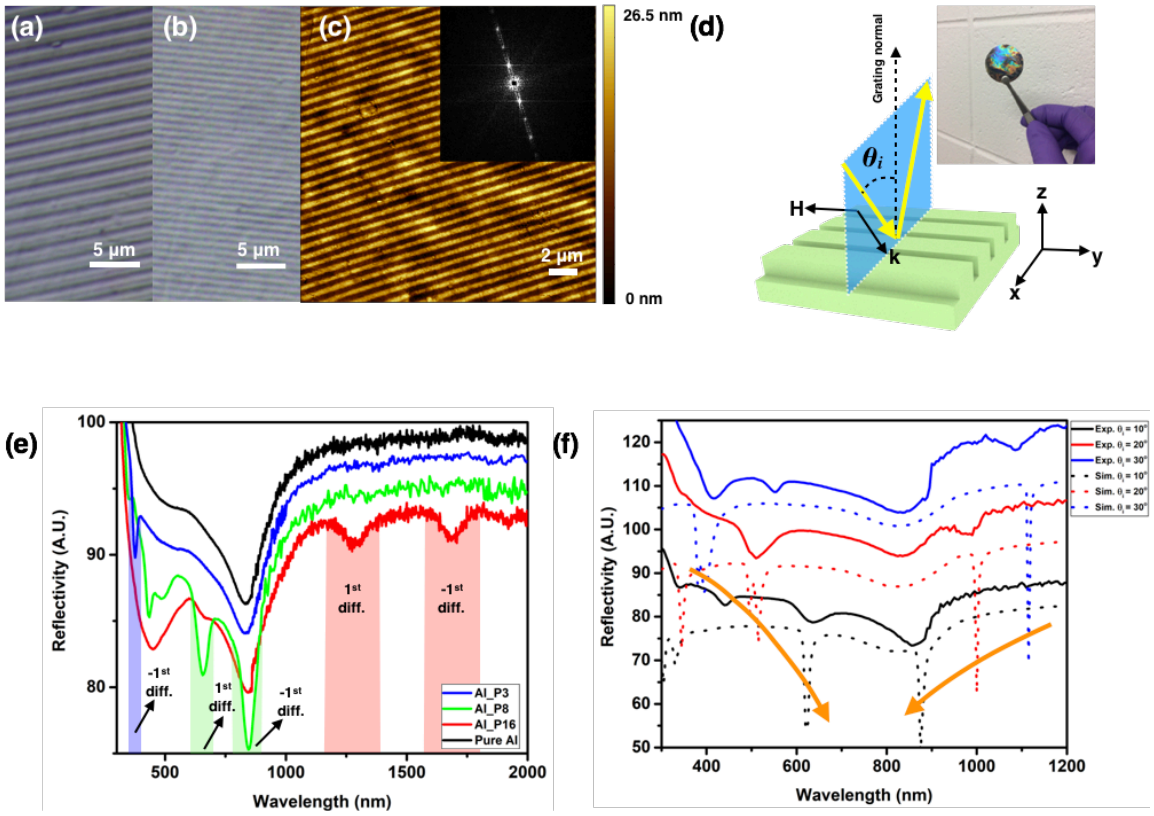


Figure 5.5 (a) optical microscopy image of Al_P16, (b) optical microscopy image of Al_P8, scale bars: 5 μm. (c) AFM image of Al_P3, scale bar: 2 μm, inset: FFT image of (c). (d) Layout for reflectivity measurement, the incident angle is 8°, (e) reflectivity for pure Al foil, Al_P16, Al_P8, and Al_P3, 1st and -1st diffraction modes for each curve are shaded except for pure Al foil, (f) angular dependence of reflectivity for the experiment (solid lines) and the simulation (dashed lines).

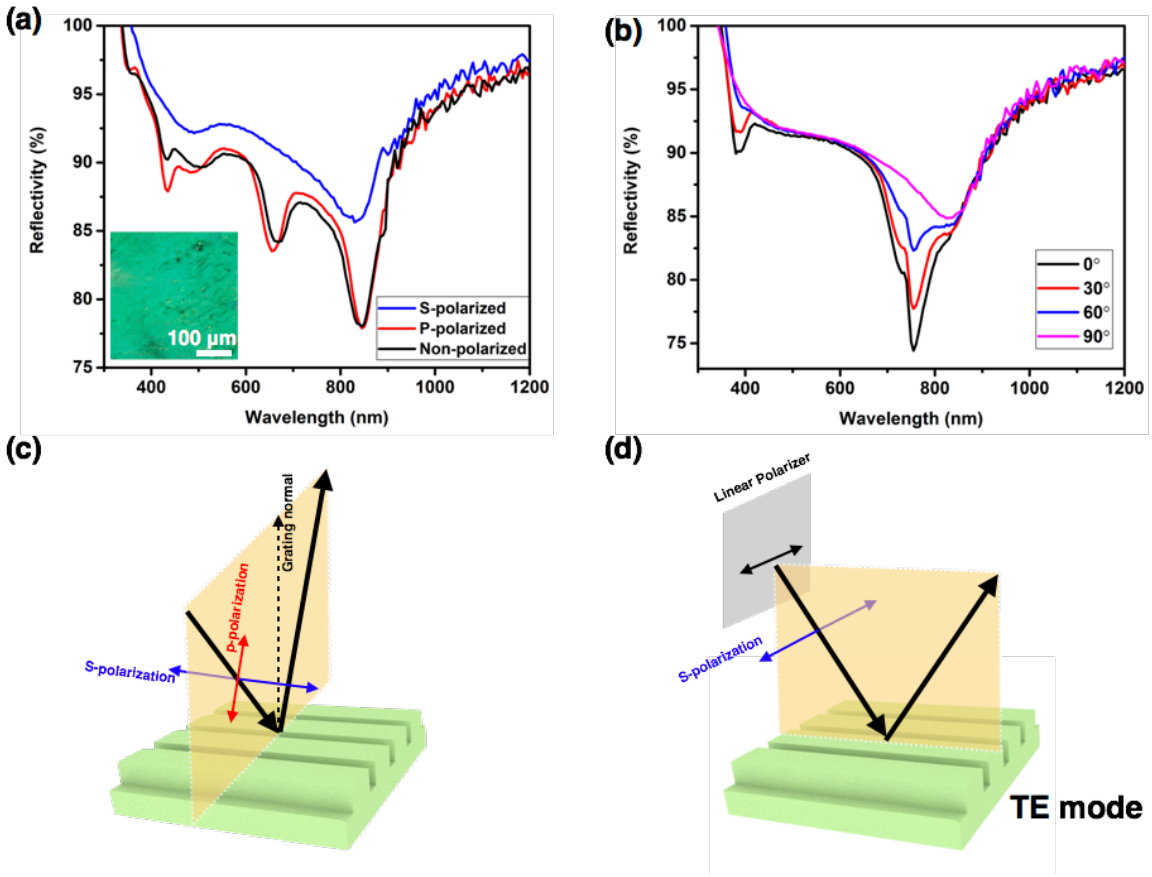


Figure 5.6 (a) Reflectivity of Al_P8 at s-polarized (blue), p-polarized (red), and non-polarized (black), inset: dark field image of Al_P8, scale bar: 100 μm, (b) reflectivity spectrum of Al_P8 at different angles of polarizer. The indecent plane is parallel to the direction of grating, (c) measurement set-up and the polarization condition when the incident plane is perpendicular to the grating direction, and (d) A linear polarizer is applied and tilted from $0^o$ (current set-up) to $90^o$ when the incident plane is parallel to the direction of the grating.

Surface plasmon waves cannot be excited from the air at a flat metal-dielectric interface since these modes live below the light line. Therefore, this surface plasmon is only excited under the addendum of external momentum such as grating structures, as mentioned above, so-called grating-coupled surface plasmon resonance. The criterion can be summarized as following[102,113],

$$k_{sp} = \pm\frac{2\pi}{\lambda_0}\sqrt{\frac{\epsilon_m\epsilon_d}{\epsilon_m+\epsilon_d}} = \frac{2\pi}{\lambda_0}\sqrt{\epsilon_d}sin\theta_i + m\frac{2\pi}{\Lambda} = k'_x \quad (9)$$

where $k_{sp}$ is the wavevector for surface plasmon, $k'_x$ is the wavevector of diffracted optical wave, $\lambda_0$, $\varepsilon_m$, $\varepsilon_d$, m, and $\Lambda$ is the wavelength for incident light, dielectric constant of metal and air, the order of diffraction (integers = 0, ±1, ±2 …), and periodicity of grating,

respectively. Indicated from the equation (9), when the incident angle ($\theta_i$) is fixed, the wavelength of resonant coupling is determined by the periodicity of the introduced grating and the order of the diffraction grating. According to the equation (9), in case of Al_16, the periodicity of $\Lambda$ exhibits a pair of resonant coupling near the wavelength of 1600 nm, one of which is greater than this periodicity at its $-1^{st}$ order mode and the rest one dip occurs below the periodicity. Analogously, dips from Al_P8 dips at 635 and 853 nm corresponds to the $1^{st}$ order and $-1^{st}$ order. Though the latter dip is overlapped with the inherent absorption of Al, it could be speculated from the decreased reflectivity compared to its counterpart of Al_P16 at this wavelength. Due to the limitation of the spectrum at short wavelength region, Al_P3 only shows a dip of reflectivity at 366 nm, which, according to the criterion of coupling resonant, refers to $-1^{st}$ order mode. For grating structures with larger periodicity, higher order diffraction modes can be coupled. For example, Al_P16 shows dips at short wavelength region such as 680 nm and 450 nm which are the dips due to the higher order mode of grating-coupled surface plasmon resonance. To further confirm this resonant effect, the incident angle is modulated to observe the change in terms of the resonant regime. As Figure 5.5 (f) shows, when the incident angle decreases from 30° to 10°, $1^{st}$ order mode of dip (~ 635 nm) is red-shifted and $-1^{st}$ order counterpart (~ 853 nm) is blue-shifted. The merging tendency of resonant peaks was numerically confirmed by S4 simulation, as shown in dashed curves in Figure 5.5(f). Eventually, it can be deduced that the peaks of the same order but the oppositely signed mode of diffractions merge into a single dip. According to the equation (1), when the incident angle is 0°, a unique value of resonant wavelength is expected. Limited by the measurement angle, it is challenging to assign incident angle to zero and to acquire corresponding reflectance spectrum. Instead, the merging phenomenon of the pair of resonant peaks can be observed by aligning the incident plane to the grating direction, with transverse-electric field mode activated by applying a linear polarizer perpendicular to the incident plane (Figure 5.6 (d)). Therefore, each order of grating-coupled resonance only observes a single dip. With the incident plane unchanged, the grating-coupled resonance cannot be excited if the magnetic field is perpendicular to the direction of gratings (Figure 5.6 (b)). In the following session, all of the optical measurements are performed under the set-up as depicted in Figure 5.5(d),

where the incident plane perpendicular to the direction of the grating and magnetic field is aligned with it.

### 5.3.4 The angular orientation of SLSI for producing of 2D and Quasi-3D nanostructures

As discussed above, trench structures excite surface plasmon resonance along the p-polarized mode, thus the structures are only optically responsive along the one direction. To expand the optical response to multiple directions, the conventional NIL uses a sequential process to generate trench structures along the other direction to complete 2D patterns. However, the whole process becomes time-consuming as the number of iteration increases, furthermore, the thermo-rheological nature of resist cause the secondary imprinting process easily relaxes the primarily imprinted patterns. SLSI technique effectively addresses this issue of pattern relaxation by precisely controlling the laser energy of each single LSI step. Figure S1(c) shows the relaxed depth of primarily imprinted trenches can be precisely controlled via laser energy, at the meanwhile, the secondary imprinting depth can be linearly modulated. Because the laser pulse duration is 5 ns, the imprinting process does not induce the long-time heating effect on metal, therefore, patterns were not as catastrophically relaxed as in the case of polymer resist patterns in NIL, where the heating duration is relatively long (~30 s) and the glass transition temperature is relatively low (~ 130 °C).

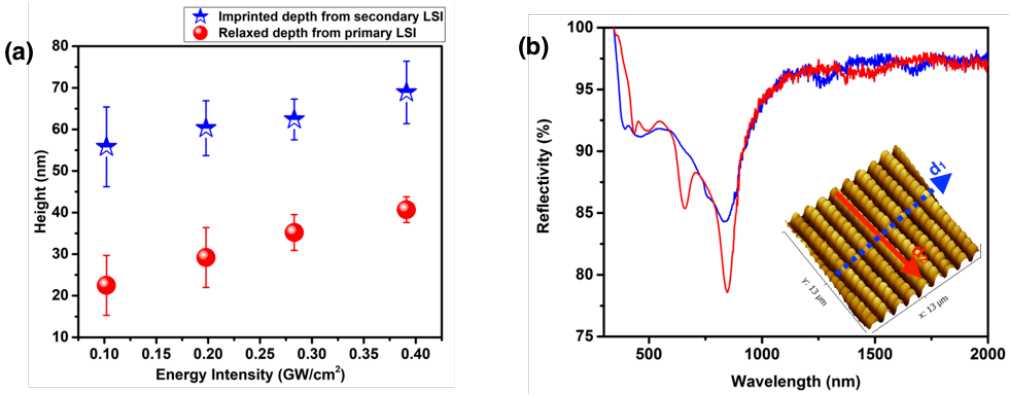


Figure 5.7 (a) Laser-modulated relaxation depth of the primarily imprinted trenches (red circles) and secondary imprinted depth (blue stars), (b) Anisotropic optical response along different orientation for LSI_P16/P8. Inset: 3D AFM images shows two typical grating direction: d1 (blue) is along the direction of P16, and d2 (red) is along the direction of P8.

By optimizing laser energy dose on each step of LSI, a variety of patterns are fabricated via combining types of mold and angles between two sequential molds. if the same mold of gratings were orthogonally SLSI-ed, the pixel arrays were realized, as shown in Figure 5.8(d) and 5.8(f). If SLSI is performed with a non-orthogonal angle ($\theta_r = 60^\circ$), an array of diamond-like nanoblocks were found in Figure 4(a). Likewise, if different types of molds were used for SLSI, multiscale nanostructures can be generated, as shown in Figure 5.8(b), 5.8(c), and 5.8(e). Due to trenches with different periodicities, which are 1600 nm for mold P16 and 720 nm for mold P8, grating-coupled surface plasmon resonance is excited at two bands. For example, when the magnetic field is aligned with mold P16 grating direction, a typical pair of infrared dips at ~ 1300 nm and ~ 1700 nm were realized, and when the magnetic field is aligned with mold P8 grating direction, characteristic resonant dips were observed at ~ 600 nm and ~ 900 nm.

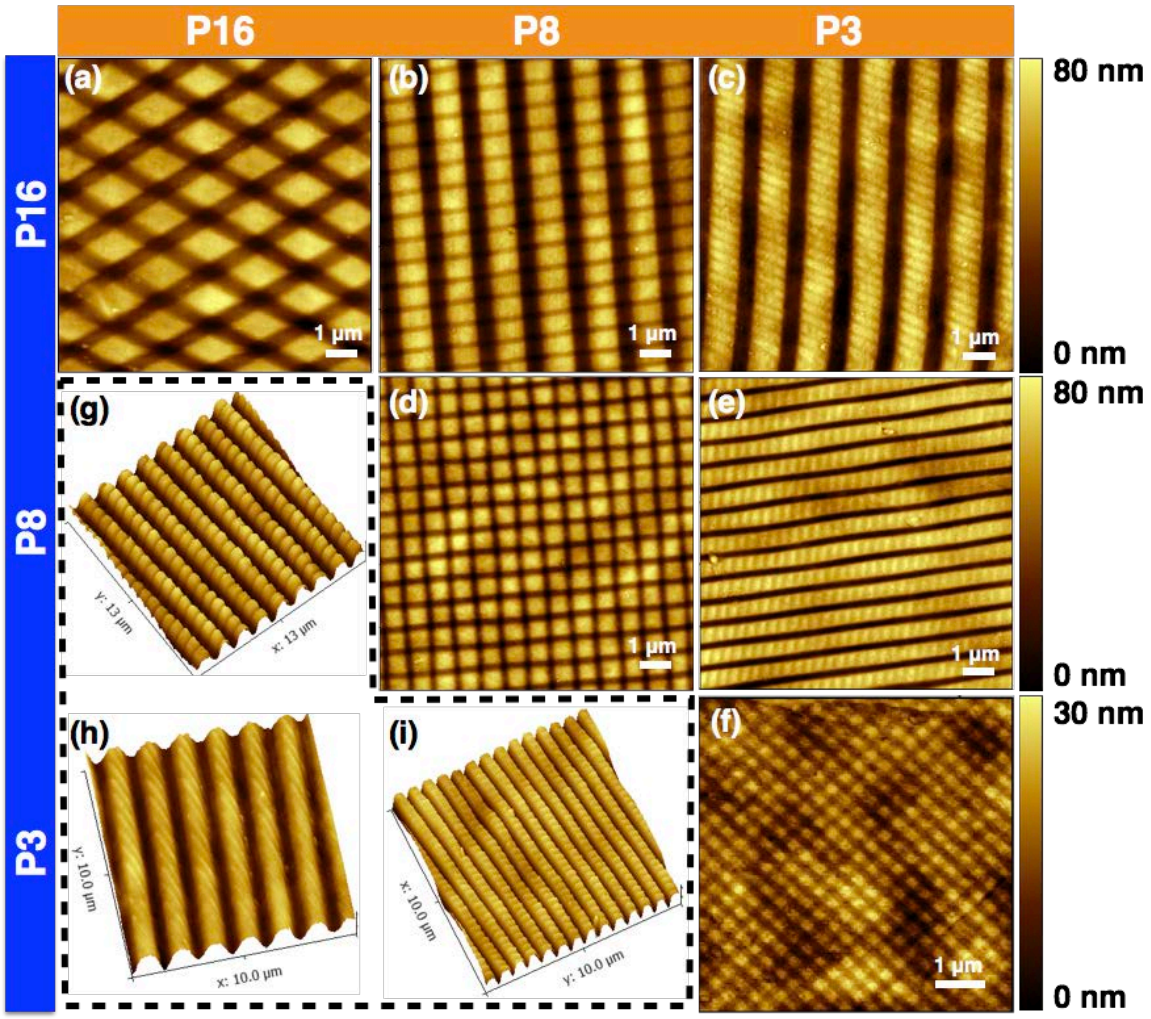


Figure 5.8 AFM images of angularly-combined SLSI_Al of (a) Al_P16/P16, (b) Al_P8/P16, (c) Al_P3/P16, (e) Al_P3/P8, (f) Al_P3/P3. 3D images of (g) Al_P16/P8, (h) Al_P3/P16, and (i) Al_P3/P8.

In addition, Quasi-3D nanostructures can be fabricated through SLSI. Figure 5(a) and the inset image of Figure 5(b) illustrate the final quasi-3D structure which was conducted with twice of each P16 mold and P3 mold imprinting process. This structure is difficult to be fabricated through other conventional processes. Interference lithography might encounter the difficulty in terms of simultaneously controlling in-plane and in-depth photon exposure. Although NIL might achieve such multi-scale structure, multiple times of RIE process most likely introduces the undesired surface roughness over the surface. SLSI can effectively avoid these issue. Firstly, in-plane and in-depth imprinting are well-controlled by tuning laser energy on each single LSI step. Secondarily, as mentioned

previously, SLIS can provide smooth surface comparable to the optical disc. Figure 5(b) exhibits the optical response of this multiscale structures. Characteristic absorption peaks for Al_P16 and Al_P3 preserve, and a minor decrease of absorption for ± 1$^{st}$ order of Al_P16 resonant peak was observed. This is mainly due to 3$^{rd}$ and 4$^{th}$ imprinting P3 mold whose depth is shallow (~ 20 nm), as a result, it relaxed the depth of original Al_P16 pixel arrays. It is interesting to observe the superposition of the low order resonant peak from Al_P3 and the high order counterparts from Al_P16 in the region below 400 nm. Electromagnetic field distribution for two bands (one near P3 periodicity range, 336 nm, and the other near P16 periodicity range, 1800 nm) are presented in Figure 5(c) and 5(d). In both bands, major enhancement occurs along the denser pillars from Al_P3, and minor enhancement is observed along larger pillars at the bottom, confirming the spectral superposition of two types of pixel arrays.

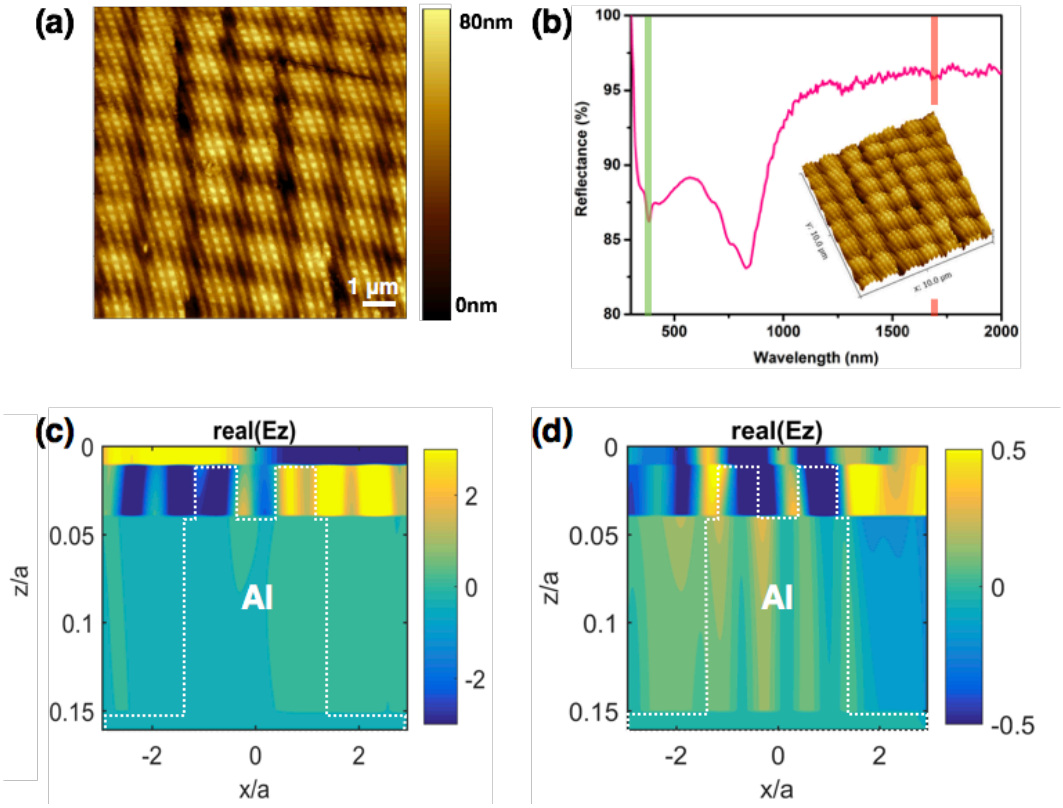


Figure 5.9 (a) AFM image of multiscale Quasi-3D nanostructures, (b) Reflectance spectrum of Quasi-3D nanostructures, inset: 3D images of multiscale Quasi-3D nanostructures. Field distributions of Quasi-3D nanostructures at (c) the low wavelength (below 400 nm) and (d) the high wavelength (above 1600 nm).

In addition to Al foil, LSI can imprint harder Ag foil using disc molds. Figure 5.10(a) shows reflectance spectrum after LSI, and similar to Al_P8, grating-coupled resonant peaks were detected near the wavelength of the periodicity of 720 nm, as well as high order resonant peak at half of the periodicity. Due to the comparable hardness of Ag foil and deposited reflective layer (Ag or Au), the detectable reflective dips are not as significant as counterparts in LSI_Al series. Despite these, surface-enhanced Raman spectroscopy indicates that LSI_Ag exhibit significant enhancement of Raman signal compared to pure Ag foil shown in Figure 5.10(b). The different detection amplitude between transverse-magnetic and transverse-electric modes confirm the polarization dependency of grating-coupled plasmon resonance.

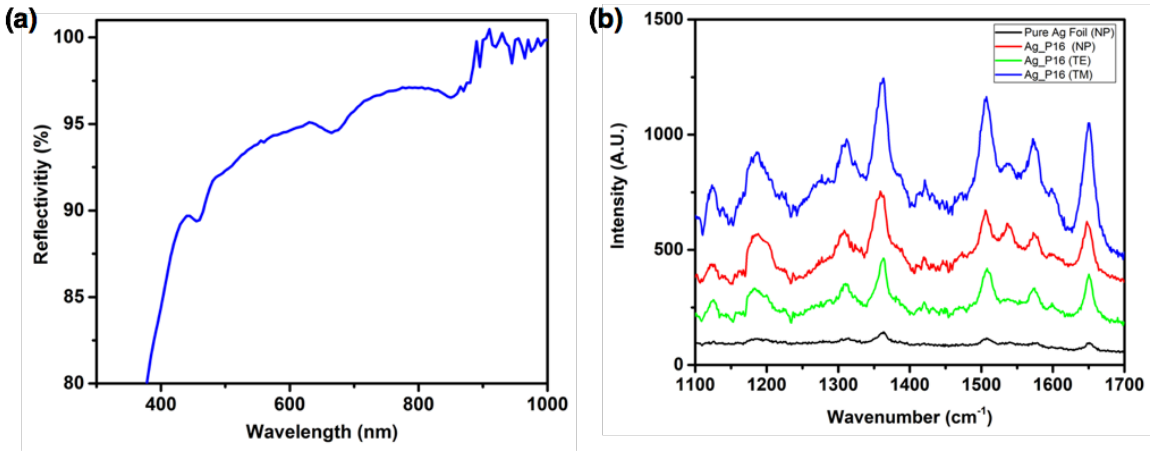


Figure 5.10 (a) Reflectivity spectrum of Ag_P8, (b) SERS detecting the molecular, R6G ( c = 0.1 mM), using pure Ag foil (black), Ag_P16 at non-polarized (NP) (red), TE mode (green), and TM mode (blue).

Lastly, LSI also shows the compatibility to the standard lithography. For example, the 10-nm Si layer is deposited on Al_P16/P8 pixel arrays as shown in Figure 5.11(a) and Figure 5.11(b). Similar to the Aluminum counterpart (Figure 4(b)), this Si-deposited pixel arrays show anisotropic reflective response due to the dual orientation of P16 and P8 trenches. If the magnetic field of the incident plane is aligned with P8 grating direction (the direction of $d_1$ in Figure 5.11(a)), resonant peaks are expected at the region of wavelength of 720 nm. More specifically, 1$^{st}$ diffraction mode occurs at ~ 650 nm and it blue-shifts as

the incident angle increases from 10° to 45°, while the -1st diffraction mode is observed at ~ 840 nm and it red-shifts. This optical response is similar to the case of imprinted Al foil because the photons below the band gap of Si (~ 1.1 eV or wavelength higher than 1100 nm) are transparent. Interestingly, the -2nd diffraction dip starts to appear and red-shifts as the incident angle increases. This is because the high absorptivity for deposited Si limits the surface plasmon resonance below 400 nm, and surface plasmon only can be resonated at the wavelength above 400 nm. When the magnetic field of the incident plane is aligned with to the grating direction of P16 (the direction of $d_2$ in Figure 5.11(d)), respective red-shift and blue-shift for -1st diffraction and 1st diffraction dips for P16 grating are observed in Figure 5.11(d) as the incident angle increases. It is worthwhile mentioning that high order diffraction dips for P16 are not apparent because the inherent reflectivity is too low to initiate the surface plasmon at shorter wavelength region.

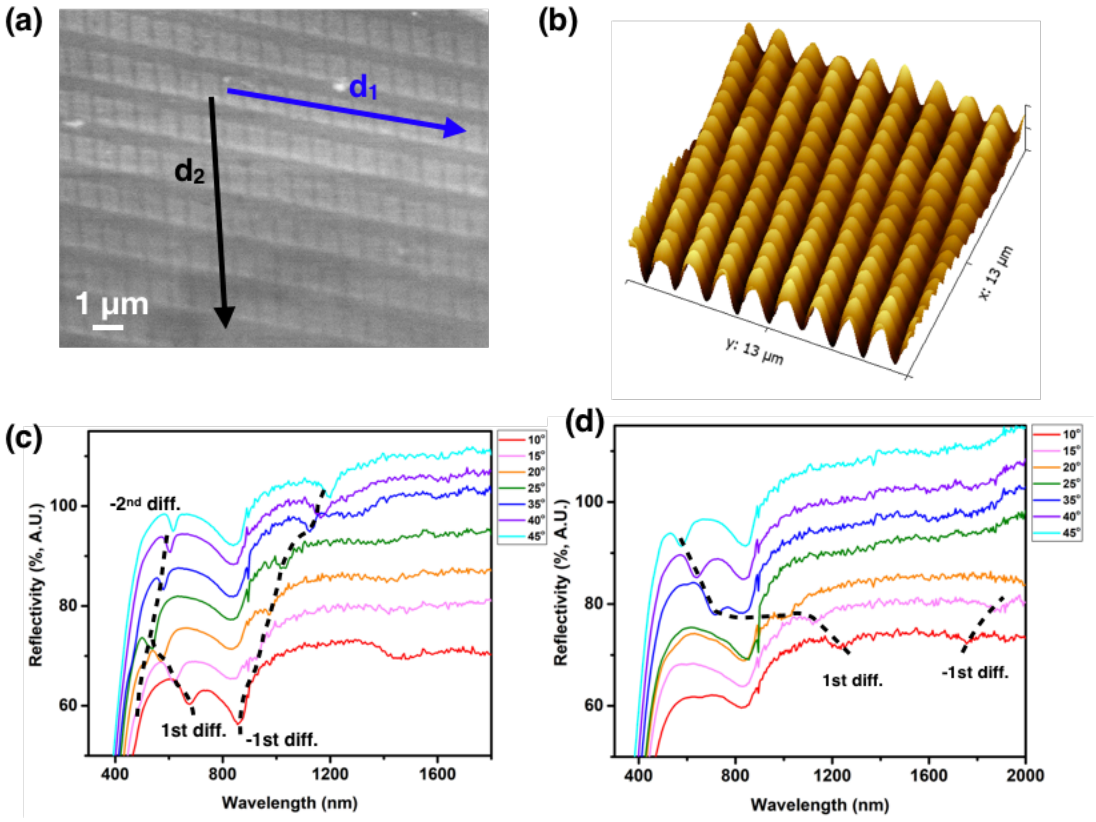


Figure 5.11 (a) SEM image of Si-deposited Al_P16/P8 pixel arrays, labeled with two major directions of trenches, (b) the corresponding 3D AFM image , (c) corresponding reflectance spectrum at different incident angles whose magnetic field is aligned with d1, and (d) corresponding reflectance spectrum at different incident angles whose magnetic field is aligned with d2.

## 5.4 Conclusions

A reliable and large-scale route of manufacturing micro/nanopatterns is presented in this study. LSI technology exhibits the capability of modulating the width of patterns from infrared, visible and ultraviolet range by selecting different discs molds. The imprinting quality of patterns is high enough for exciting grating-coupled surface plasmon resonance. The efficiency of this surface plasmon is additionally tuned through imprinting depth of patterns by changing the applied laser energy density. Ultimately, the selection of different types of molds, angles, and controlling energy doses result in multiscale micro/nanopatterns. This combination enables the anisotropic optical reflectance of foils by using two different molds orientated in certain angles. In addition to patterning pure metallic foil, LSI was used to generate periodic patterns onto semiconductor/metal foil, and its surface plasmon resonance preserves at the infrared and visible region. In sum, successive LSI with soft optical molds is a powerful and compatible technique to economically access large-area fabrication of hierarchical micro/nanopattern with high accuracy and fidelity.

# CHAPTER 6. LASER SHOCK IMPRINTING OF LOW DIMENSIONAL MATERIAL WITH ASSIST OF SOFT TEMPLATES

## 6.1 Introduction

Strain engineering has become one of the emerging areas, and various materials have been under intensive studies[114,115], including polymers[116], semiconductors[117], and semimetals[118]. Since 2004, CMOS manufacturing took advantages of strain engineer, which occurred from lattice mismatch to increase the carrier mobility. Recently, 2D materials are under on-going intensive research because such type of materials, including graphene, transition metal dichloride (TMDC)[119], and Te[120], have great performance, electrics[121], and optoelectronics[119], as well as great potential as flexible electronics[122]. Up to dates, various approaches toward introducing strains on 2D materials have been attempted, including lattice mismatch[123], buckling-method[124], and capillary-driven solution process[119]. Though these methods successfully integrated the strains on 2D materials, the precise control still remains a challenging issue. It is essential to develop a method of introducing strains on 2D material in a controllable manner. As shown in chapter 5, LSI is advantageous in producing controllable strains rather than random and material-dependent ones.

## 6.2 Experimental method

### 6.2.1 Imprinting process

The imprinting process is described in Figure 6.1. 2D materials are transferred on the surface of Al foil, followed by LSI process toward soft template. Due to the induced pressure by LSI, the metallic foil will be imprinted along with the 2D material underneath.

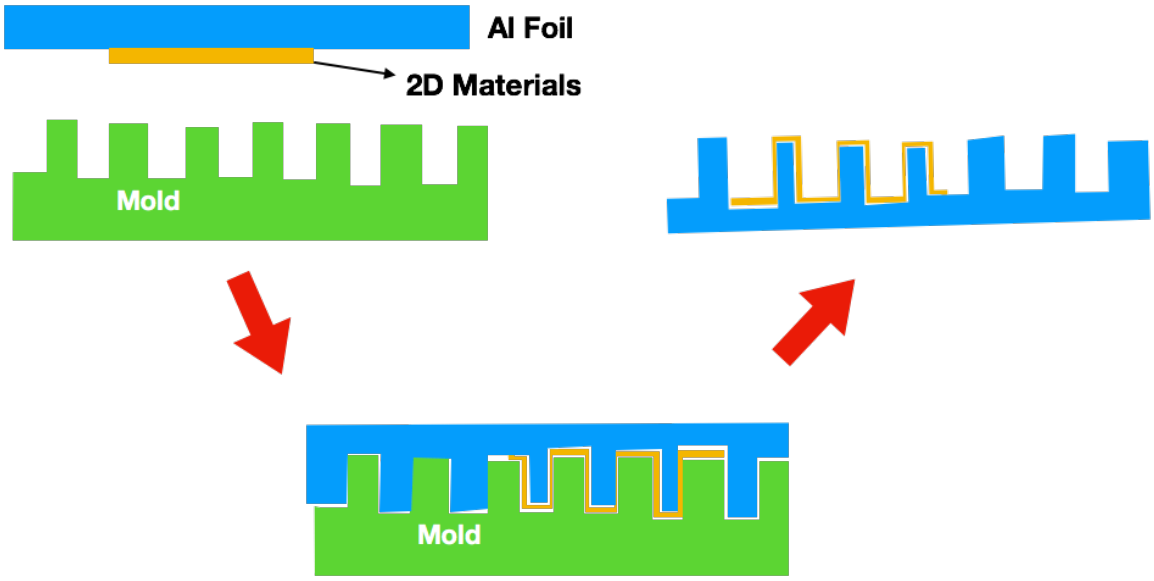


Figure 6.1 A schematic illustration of strain-inducing process using LSI

### 6.2.2 2D material transfer

#### 6.2.2.1 $WSe_2$ Transfer

A scotch tape process was used to exfoliate $WSe_2$ from the bulky to metallic foils. Special care is needed to avoid the damage toward the foil during the delamination of the tapes. In addition, short-term of mid-temperature baking is helpful to result in a large area of effective and usable 2D flakes with large size.

#### 6.2.2.2 Graphene transfer

A CVD-grown graphene on copper was transferred on Al membrane (4 um) using standard solution process. Typically, a layer of PMMA was spin-coated on graphene-grown copper, and the other side of graphene was removed by oxygen plasma (50 sccm at 50W for 1 min). The plasma-treated side was exposed to solution of $FeCl_3$ to initiate the chemical etching of copper until the PMMA layer and graphene layer remains. Then, this pair of layers were repeated rinsed with DI water to remove possible solution residual, ensuring the sample is free from any massive potential doping. This layer of composite was then placed on the top of the graphene layer, followed by either natural drying or gentle baking at 80°.

### 6.2.3 LSI of 2D/Al using soft-template

As prepared 2D/Al was placed on the soft-templates such as CD molds, covered by graphite-sprayed Al membrane, the sacrificial layer.

### 6.2.4 KPFM and AFM measurement

KPFM and AFM were coupled to measure the electrical and topological output from imprinted graphene/Al. Typically, KPFM was used to measure surface potential, while the AFM was used for measuring the topology.

### 6.2.5 Raman Spectroscopy

A numerical aperture of 0.9 with the magnification of 100 was used to focus the laser beam (wavelength of 532 nm) down to 1 um. 1800/mm or 2400/mm grating was used. Collecting time ranges from 10 s to 15 s to minimize the background noise. The slit is fixed at 200 during the measurement.

## 6.3 Results and discussion

### 6.3.1 WSe2 Characterization

An exfoliated flake of $WSe_2$ was transferred to Al foil surface as shown in Figure 6.2 (b). The brown flake is the transferred one with a layer of ~ 10, and the color is darker as the layer increases. Raman spectroscopy of $WSe_2$ is listed in Figure 6.2 (a), and characteristic peaks at 251 and 260 $cm^{-1}$ are presented.

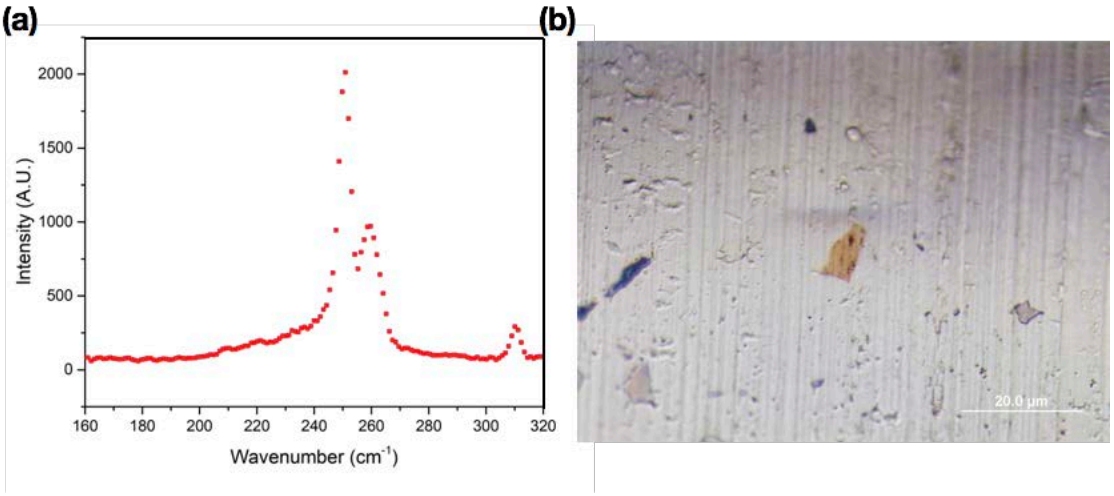


Figure 6.2 (a) Raman Spectroscopy of $WSe_2$ on Al and (b) an optical image of the transferred $WSe_2$ on Al foil.

### 6.3.2 LSI on WSe2 flakes

$WSe_2$ flakes were performed with LSI process as Figure 6.3 (b) described. It can be seen that the high throughput and high yield of LSI on imprinting 2D flakes. It should be noted that the red dashed region are not shown the continuity within the flake, meaning possible break or cracks induced by this high-pressure process. As covered in the second chapter, LSI could reach 1 GPa pressure which might be too high pressure to be sustained by $WSe_2$.

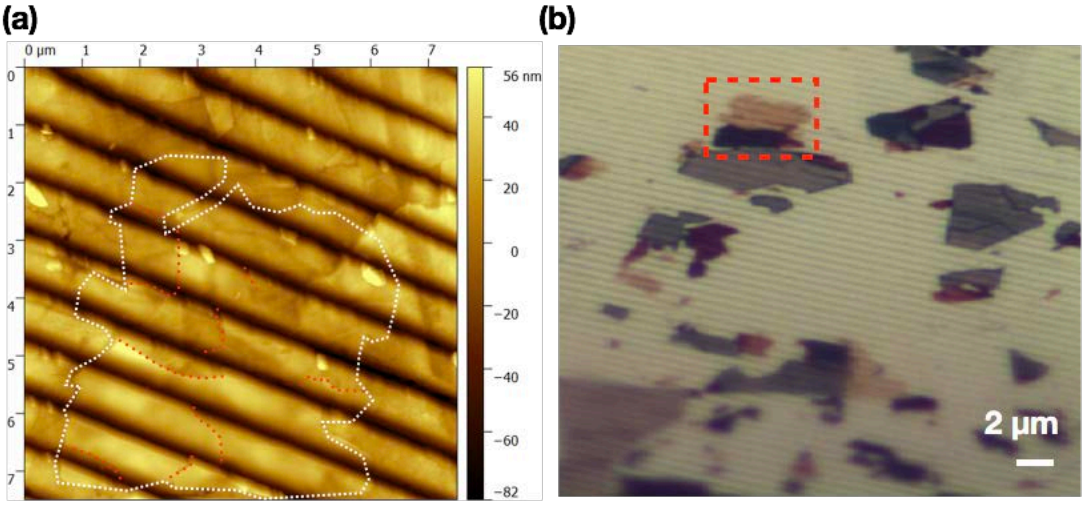


Figure 6.3 (a) an AFM image of imprinted $WSe_2$ and (b) a corresponding optical image

Mechanical properties of $WSe_2$ was referred from the previous studies. Zhang and his coworkers reported [125] that Young's modulus of this material is 167.3 GPa, and that it can endure as much as ~ 12.5 GPa under AFM tip deformation, which corresponds to 7.3% strain. Because of structures of the mold, it might be challenging to keep all region of the flake under the fracture point. In addition, low Young's modulus allows the flake to be sensitive to mechanical deformation. Thus, the high pressure results in cracks, and the strain is released to zero. The alternative solution is the use of stiffer material such as graphene whose Young's modulus is near 1 TPa and the elastic strain is about ~ 13%[126].

### 6.3.3 Graphene characterization

Graphene was grown on the copper surface by CVD temperature over 1075 °C. To verify the quality of graphene, it was transferred to $SiO_2$ surface and used with Raman spectroscopy.

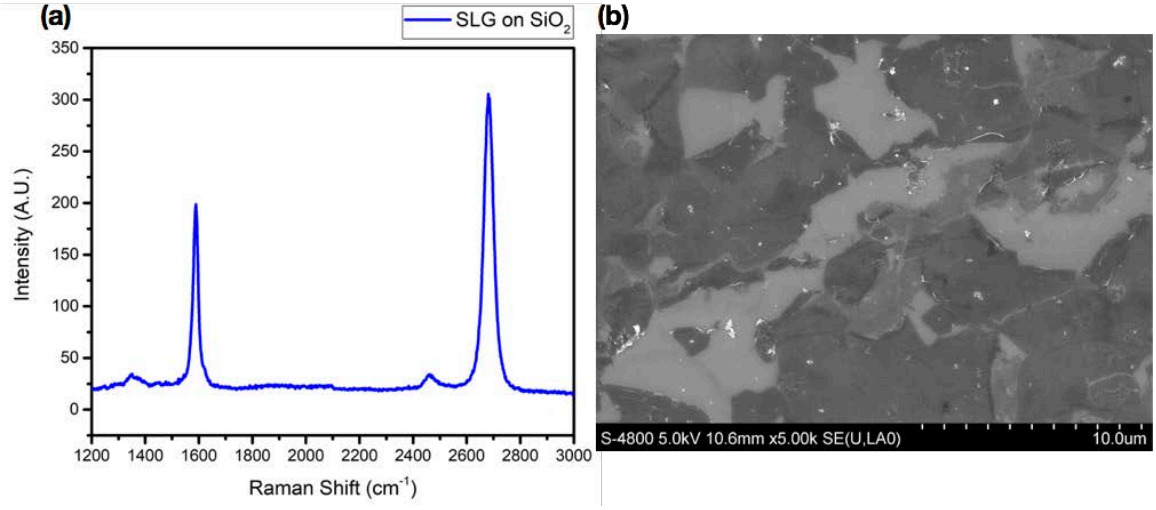


Figure 6.4 (a) Raman Spectroscopy of Single-layered graphene (SLG) on $SiO_2$ and (b) SEM images of transferred graphene on Si wafer.

It can be seen from Figure 6.4 (a) that the quality of SLG is beyond the average because the indicator of defect (1350 $cm^{-1}$) is relatively low. But the crystal quality has a lot of room to improve until ratio between 2D (~ 2700 $cm^{-1}$) and G (~ 1600 $cm^{-1}$) is close to 2. In addition, the transferring graphene into Si wafer did not lead to a good output as Figure 6.4 (b) shows. The reason is that the wettability of Si wafer without thick oxide repels water drop which was involved from graphene transfer. This causes undesirable

wrinkles on graphene even before successfully transferred on the substrate. Thus, it will be preferable of using $SiO_2$ instead of Si due to its hydrophilicity.

### 6.3.4 LSI on graphene and strain effects from surface potentials

A monolayer graphene is transferred onto the Al foil, followed by LSI process toward a 1600-nm periodicity trench mold. KFPM was used to characterize both topology and the distribution of contact potential difference (CPD) along the LSI-ed area. The definition of CPD ($V_{CPD}$) between the tip and the sample is following[46]:

$$V_{CPD} = \frac{\phi_{tip} - \phi_{sample}}{-e} \tag{10}$$

where $\Phi_{tip}$ and $\Phi_{sample}$ are work functions of the tip and the sample. The tip approaches close to the sample surface, then the forward scan characterize the topology and the backward scan characterize the contact potential difference. Since the whole sample was grounded, both topology and CPD were collected from the graphene area rather than Al foil underneath.

Figure 6.5(a) shows the topology image of LSI-ed graphene/Al samples, where the sample surface was uniformly and periodically imprinted. Figure 1(b) shows the CPD along the sample surface, ranging from 0.739 V to 0.609 V. If profiles are extracted from both the topological and the surface potential distributions, it is found that both profiles do not synchronize in terms, as shown in Figure 6.2(c). Instead, the crest of the topology meets the valley of CPD. To analyze the potential strain-induced CPD changes, a statistical distribution of heights and CPDs are presented in Figure 6.2(d) and Figure 6.2(e). The difference in height between crests and valleys is ~ 47.5 nm, whereas the corresponding CPD is ~ 46.2 mV. This sinusoidal fluctuation of monolayer graphene can be converted into the corresponding strain. For a simplified model of small deflection, the maximum strain[127] is calculated as

$$\epsilon \approx \frac{8z^2}{3a^2} \tag{11}$$

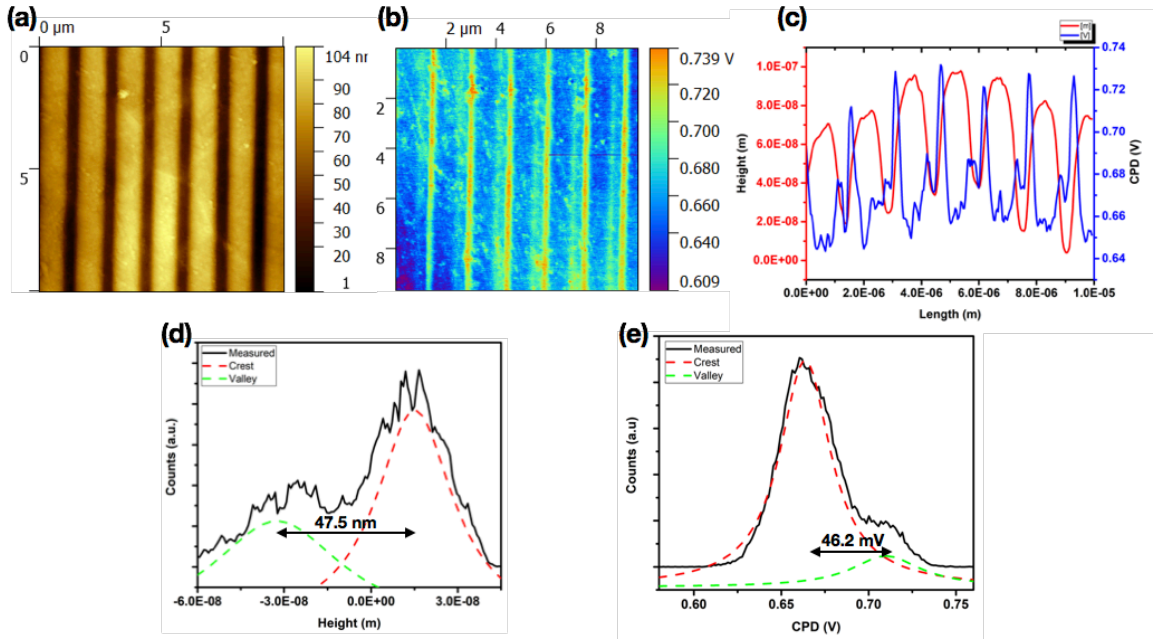


Figure 6.5 Characterization of graphene/Al samples of (a) Atomic force microscopy (AFM) image of topology, (b) the corresponding KPFM image, (c) profiles for topology and CPD, (d) height distribution, and (e) CPD distribution

For sinusoidal trenches with a periodicity of 1600 nm and the imprinting depth of 47.5 nm, the maximum strain reaches ~ 0.24%. According to Volodin et. al.'s work, the tensile strain can induce the increase in work function[127], therefore, the resultant CPD due to strain is lower than the counterpart of less-strained area. As seen from the Figure (c), crest regions are applied with more strains than valley regions, resulting in lower CPD for crest regions. In the meanwhile, the same process of LSI and corresponding characterization of topology and CPD were performed to the pure Al foil. As Figure 6.3(a) and 6.6(b) show, the sinusoidal trenches were imprinted on the Al foil and the overall CPD ranges from 1.15 to 1.07 V. The higher CPD results from an inherently lower work function of Al compared to graphene. Similar to the case of Al/graphene, desynchronization between the topological profile and the CPD profile was observed. It can be deduced that the periodic surface fluctuation also induces the periodic CPD modulation. Though the difference of depth between the crest and the valley is ~ 38.0 nm, which is the same range of the former case of graphene/Al trenches, the maximum CPD for Al is less than the counterpart of graphene/Al. Thus, we speculate that periodic CPD distribution is another evidence of strains on monolayer graphene.

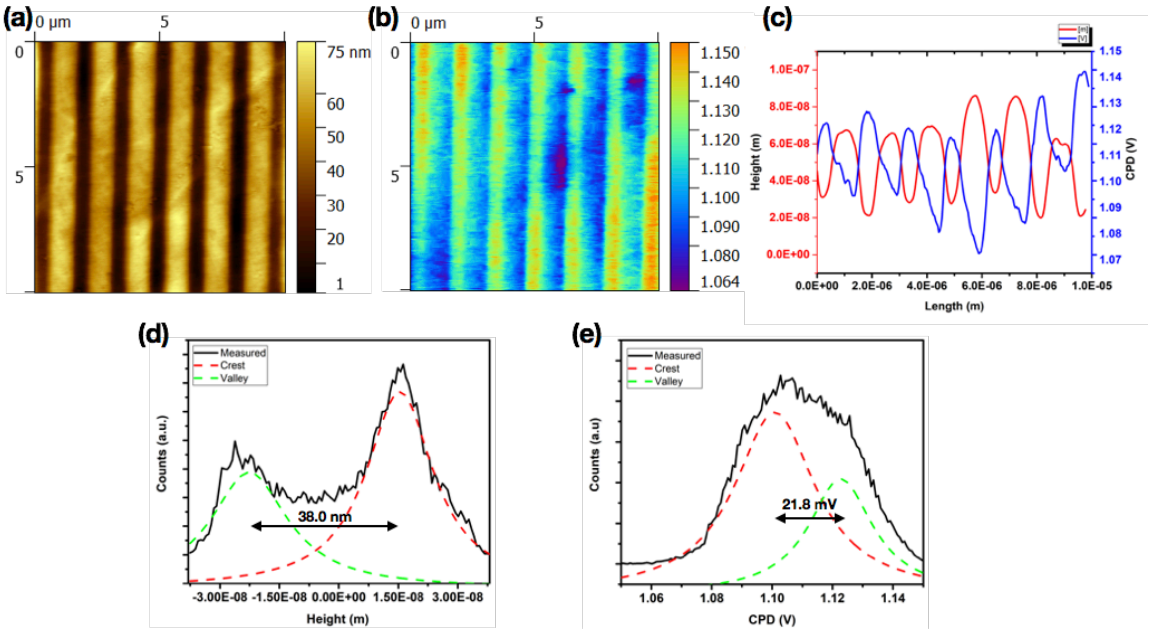


Figure 6.6 Characterization of Al sample of (a) AFM image of topology, (b) the corresponding KPFM image, (c) profiles for topology and CPD, (d) height distribution, and (e) CPD distribution

## 6.4 Conclusion

In this chapter, we introduced an effective approach to introducing strains on 2D materials such as $WSe_2$ and Graphene. It concludes that $WSe_2$ cannot survive through LSI due to low mechanical properties, while the graphene most likely is induced with strains. Raman was inspected the quality of graphene and CD molds were used as templates for imprinting graphene/Al towards. KPFM study can partially prove the successfully introduced strains on graphene.

# CHAPTER 7. CONCLUSION AND FUTURE WORK

## 7.1 Conclusion

In this dissertation, laser shock imprinting process is extended from sophisticated silicon wafer template layout to multiscale soft template configuration. The advantage of LSI, which is conformable and precise high throughput process, is remained, and in the meantime, the structural complexity is further increased. Natural leaves were successfully transferred into metallic membranes, and furthermore, the fabricated membranes were employed as triboelectric nanogenerators. A key role of a deposited metallic layer was discovered to further improve LSI resolution, addressing the issue of soft stiffness from soft templates. Numerical methods were used to validate the experimental findings of successful imprinting phenomena, from soft templates to hard metallic membranes. The imprinted membranes exhibited excellent optical responses due to high-quality imprinted micro/nanostructures. Eventually, this technique was used to induce strains in low dimensional materials.

Typically, we demonstrate for the first time a TENG device with LSI-processed biomimic hierarchical structured metal electrodes for efficient harvesting of water-drop energy in the environment. Mimicking and transferring hierarchical microstructures from natural templates into the water-TENG device is effective regarding repelling water drops off the device surface since surface hydrophobicity from these bio-microstructures maximizes the TENG output. Among various leaves' microstructures, hierarchical microstructures from dried bamboo leaves are preferable regarding maximizing power output, which attributes from its unique structures containing both dense nanostructures and microscale features compared with other types of leaves. Also, the triboelectric output is significantly improved by closely mimicking hydrophobic nature of leaves in LSI processed metal surface after functionalizing it with low surface-energy self-assembled monolayers (SAMs). This approach opens doors to new manufacturable TENG technologies for economically feasible and ecologically friendly production of functional devices with directly-patterned 3D biomimic metallic surfaces in energy, electronics, and sensor applications.

We introduce a successive laser shock imprinting process to manufacture complex hierarchical micro/nanopatterns on metallic foils with 1D-periodic trench molds. The molds can be as simple as low-cost blank optical discs. The capability of modulation of this technique is systematically investigated. A variety of micro/nanostructures are patterned through sequentially imprinting a metal foil into trench molds with a combination of depth (laser intensity), width (types of mold), and angles (rotation between molds). This integration of successive accurate LSI with low-cost and highly reliable optical disc exploits a competitive way to manufacture micro/nanopatterns with good cost-effectiveness.

Lastly, two typical 2D materials, $WSe_2$ and graphene, were attempted with LSI to induce strain. The former suffered from catastrophic damages under the process, due to poor mechanical property. Whereas, graphene flakes survived and the surface potential provides the induced strains.

## 7.2 Future work

LSI is such a productive and precise approach towards manufacturing metallic membranes by introducing plastic deformations at high strain rate. The work was proposed and developed by Dr. Huang Gao, Dr. Yingling Yang, and Dr. Ji Li, then further highlighted by Dr. Yaowu Hu. The imprinting accuracy and preciseness were improved from mesh sizes to nowadays sub-10 nm. The room for improving accuracy is not limited but obviously challenging due to the bottleneck of the current IC technology. Now it is the chance to expand the application of LSI purely from metallic membranes to other types of materials. The current roadmap has been initiated into low dimensional materials, such as 2D flakes and 1D nanowires. Addressing the issue of the huge mechanic discrepancy between generated pressures and the target material is the key to the successful expansion of such technology. Thus, further direction of development on LSI is proposed to be: (1) structural designs of templates in both hard and soft templates, (2) interface designs of templates regarding the modulation of the friction, (3) materials designs for improving the mechanical stiffness to survive through LSI, such as heterostructures of 2D materials.

# REFERENCES


[1] Andreas Ostendorf; Sabine Clauben; Marshall G. Jones, in *Intell. Energy F. Manuf.*, **2017**, pp. 259–298.

[2] G. J. Cheng, W. Zhang, Y. L. Yao, in *Intell. Energy F. Manuf.*, **2017**, p. 299.

[3] H. Gao, Y. Hu, Y. Xuan, J. Li, Y. Yang, R. V. Martinez, C. Li, J. Luo, M. Qi, G. J. Cheng, *Science* **2014**, *346*, 1352.

[4] Z. Hu, S. Gorumlu, B. Aksak, G. Kumar, *Scr. Mater* **2015**, *108*, 15.

[5] Y. Hu, J. Li, J. Tian, Y. Xuan, B. Deng, K. L. McNear, D. G. Lim, Y. Chen, C. Yang, G. J. Cheng, *Nano Lett.* **2016**, *16*, 7536.

[6] Y. Hu, P. Kumar, R. Xu, K. Zhao, G. J. Cheng, *Nanoscale* **2015**, *8*, 172.

[7] R. Bartolini, W. Hannan, D. Karlsons, M. Lurie, *Appl. Opt.* **1970**, *9*, 2283.

[8] Y. Xia, J. Tien, D. Qin, G. M. Whitesides, *Langmuir* **1996**, *12*, 4033.

[9] P. Ruchhoeft, M. Colburn, B. Choi, H. Nounu, S. Johnson, T. Bailey, S. Damle, M. Stewart, J. Ekerdt, S. V. Sreenivasan, J. C. Wolfe, C. G. Willson, *J. Vac. Sci. Technol. B Microelectron. Nanom. Struct.* **1999**, *17*, 2965.

[10] S. Y. Chou, P. R. Krauss, P. J. Renstrom, *Appl. Phys. Lett.* **1995**, *67*, 3114.

[11] S. Y. Chou, *J. Vac. Sci. Technol. B Microelectron. Nanom. Struct.* **1997**, *15*, 2897.

[12] L. J. Guo, *Adv. Mater.* **2007**, *19*, 495.

[13] G.-Y. Jung, Z. Li, W. Wu, Y. Chen, D. L. Olynick, S.-Y. Wang, W. M. Tong, R. S. Williams, *Langmuir* **2005**, *21*, 1158.

[14] Y. Hirai, Y. Tanaka, *J. Photopolym. Sci. Technol.* **2002**, *15*, 475.

[15] Y. Hirai, *J. Photopolym. Sci. Technol.* **2005**, DOI 10.2494/photopolymer.18.551.

[16] L. J. Guo, *J. Phys. D. Appl. Phys.* **2004**, *37*, R123.

[17] Y. Hirai, Y. Onishi, T. Tanabe, M. Shibata, T. Iwasaki, Y. Iriye, *Microelectron. Eng.* **2008**, *85*, 842.

[18] W. Kurnia, M. Yoshino, *J. Micromechanics Microengineering* **2009**, *19*, 125028.

[19] G. Kumar, H. X. Tang, J. Schroers, *Nature* **2009**, *457*, 868.

[20] S. Buzzi, M. Dietiker, K. Kunze, R. Spolenak, J. F. Löffler, *Philos. Mag.* **2009**, *89*, 869.

[21] S. W. Pang, *J. Vac. Sci. Technol. B Microelectron. Nanom. Struct.* **1998**, DOI 10.1116/1.590024.

[22] K. A. Lister, S. Thoms, D. S. Macintyre, C. D. W. Wilkinson, J. M. R. Weaver, B. G. Casey, *J. Vac. Sci. Technol. B Microelectron. Nanom. Struct.* **2004**, *22*, 3257.

[23] D. Devaux, R. Fabbro, L. Tollier, E. Bartnicki, *J. Appl. Phys.* **1993**, *74*, 2268.

[24] R. Fabbro, J. Fournier, P. Ballard, D. Devaux, J. Virmont, *J. Appl. Phys.* **1990**, DOI 10.1063/1.346783.

[25] Y. Liao, Y. Yang, G. J. Cheng, *J. Manuf. Sci. Eng.* **2012**, *134*, 034503.

[26] D. Lin, M. Saei, S. Suslov, S. Jin, G. J. Cheng, *Sci. Rep.* **2015**, *5*, 15405.

[27] Y. Liao, C. Ye, G. J. Cheng, *Opt. Laser Technol.* **2016**, *78*, 15.

[28] H. Gao, G. J. Cheng, in *J. Appl. Phys.*, **2011**.

[29] H. Gao, C. Ye, G. J. Cheng, *J. Manuf. Sci. Eng.* **2009**, DOI 10.1115/1.4000100.

[30] H. Gao, R. Tang, T. Ma, H. Jiang, H. Yu, G. J. Cheng, *J. Microelectromechanical Syst.* **2015**, *24*, 414.

[31] H. Gao, R. Tang, T. Ma, H. Jiang, H. Yu, G. J. Cheng, *J. Microelectromechanical Syst.* **2013**, *22*, 1428.

[32] H. Gao, G. J. Cheng, *J. Microelectromechanical Syst.* **2010**, *19*, 273.

[33] Y. Hu, Y. Xuan, X. Wang, B. Deng, M. Saei, S. Jin, J. Irudayaraj, G. J. Cheng, *Adv Mater* **2016**, *28*, 9152.

[34] J. Li, Y. Liao, S. Suslov, G. J. Cheng, *Nano Lett.* **2012**, *12*, 3224.

[35] J. Li, T. F. Chung, Y. P. Chen, G. J. Cheng, *Nano Lett.* **2012**, DOI 10.1021/nl301817t.

[36] J. Li, R. J. Zhang, H. Q. Jiang, G. J. Cheng, *Nanotechnology* **2011**, DOI 10.1088/0957-4484/22/47/475303.

[37] Y. Hu, P. Kumar, R. Xu, K. Zhao, G. J. Cheng, *Nanoscale* **2016**, *8*, 172.

[38] Y. Hu, P. Kumar, Y. Xuan, B. Deng, M. Qi, G. J. Cheng, *Adv. Opt. Mater.* **2016**, DOI 10.1002/adom.201600201.

[39] G. . Parker, M. D. . Charlton, M. . Zoorob, J. . Baumberg, M. . Netti, T. Lee, *Philos. Trans. R. Soc. A Math. Phys. Eng. Sci.* **2006**, *364*, 189.

[40] M. Abramowitz, M. Davidson, "Numerical Aperture and Resolution," **n.d.**

[41] R. Reifenberger, *Fundamentals of Atomic Force Microscopy*, **2016**.

[42] G. Binnig, C. F. Quate, C. Gerber, *Phys. Rev. Lett.* **1986**, *56*, 930.

[43] U. Hartmann, *Annu. Rev. Mater. Sci.* **1999**, DOI 10.1146/annurev.matsci.29.1.53.

[44] B. S. Simpkins, E. T. Yu, P. Waltereit, J. S. Speck, *J. Appl. Phys.* **2003**, DOI 10.1063/1.1586952.

[45] J. W. P. Hsu, M. J. Manfra, R. J. Molnar, B. Heying, J. S. Speck, *Appl. Phys. Lett.* **2002**, *81*, 79.

[46] W. Melitz, J. Shen, A. C. Kummel, S. Lee, *Surf. Sci. Rep.* **2011**, *66*, 1.

[47] D. Y. Kwok, a. W. Neumann, *Contact Angle Measurement and Contact Angle Interpretation*, **1999**.

[48] D. Y. Kwok, T. Gietzelt, K. Grundke, H.-J. Jacobasch, A. W. Neumann, *Langmuir* **1997**, DOI 10.1021/la9608021.

[49] J. M. Hollander, W. L. Jolly, *Acc. Chem. Res.* **1970**, DOI 10.1021/ar50030a003.

[50] W. E. Swartz, *Anal. Chem.* **1973**, *45*, 788A.

[51] J. F. Moulder, W. F. Stickle, P. E. Sobol, K. D. Bomben, *Surf. Interface Anal.* **1979**, DOI 10.1002/sia.740030412.

[52] Z. L. Wang, W. Wu, *Angew. Chemie Int. Ed.* **2012**, *51*, 11700.

[53] F.-R. Fan, L. Lin, G. Zhu, W. Wu, R. Zhang, Z. L. Wang, *Nano Lett.* **2012**, *12*, 3109.

[54] Z. L. Wang, J. Chen, L. Lin, J. Ha, B.-S. Lee, Y. Park, C. Choong, J.-B. Kim, Z. L. Wang, H.-Y. Kim, J.-J. Park, U. I. Chung, *Energy Environ. Sci.* **2015**, *8*, 2250.

[55] F.-R. Fan, Z.-Q. Tian, Z. Wang, *Nano Energy* **2012**, *1*, 328.

[56] Z.-H. Lin, G. Cheng, W. Wu, K. C. Pradel, Z. L. Wang, *ACS Nano* **2014**, *8*, 6440.

[57] Y. Zi, J. Wang, S. Wang, S. Li, Z. Wen, H. Guo, Z. L. Wang, *Nat. Commun.* **2016**, *7*, 10987.

[58] F. Yi, L. Lin, S. Niu, J. Yang, W. Wu, S. Wang, Q. Liao, Y. Zhang, Z. L. Wang, *Adv. Funct. Mater.* **2014**, *24*, 7488.

[59] Z. Wang, *ACS Nano* **2013**, *7*, 9533.

[60] Y. Bao, R. Wang, Y. Lu, W. Wu, *APL Mater.* **2017**, *5*, 074109.

[61] F.-R. Fan, L. Lin, G. Zhu, W. Wu, R. Zhang, Z. Wang, *Nano Lett* **2012**, *12*, 3109.

[62] M.-L. Seol, J.-H. Woo, D.-I. Lee, H. Im, J. Hur, Y.-K. Choi, *Small Weinheim Der Bergstrasse Ger* **2014**, *10*, 3887.

[63] S. Wang, Y. Zi, Y. S. Zhou, S. Li, F. Fan, L. Lin, Z. L. Wang, *J. Mater. Chem. A* **2016**, *4*, 3728.

[64] E. Ozbay, *Science* **2006**, *311*, 189.

[65] G. Zhang, J. Zhang, G. Xie, Z. Liu, H. Shao, *Small* **2006**, *2*, 1440.

[66] S. Reyntjens, R. Puers, *J. Micromechanics Microengineering* **2001**, *11*, 287.

[67] W. E. Frazier, *J. Mater. Eng. Perform.* **2014**, *23*, 1917.

[68] Y. Ren, S. H. Huang, S. Mosser, M. O. Heuschkel, A. Bertsch, P. C. Fraering, J. J. J. Chen, P. Renaud, *Micromachines* **2015**, *6*, 1923.

[69] J.-Y. Cho, G. Kim, S. Kim, H. Lee, *Electron Mater Lett* **2013**, *9*, 523.

[70] Z. Lin, G. Cheng, S. Lee, K. C. Pradel, Z. Wang, *Adv Mater* **2014**, *26*, 4690.

[71] G. Cheng, Z.-H. Lin, Z. Du, Z. L. Wang, *ACS Nano* **2014**, *8*, 1932.

[72] Q. Liang, X. Yan, Y. Gu, K. Zhang, M. Liang, S. Lu, X. Zheng, Y. Zhang, *Sci Reports* **2015**, *5*, 9080.

[73] H. Guan, Z. Han, H. Cao, S. Niu, Z. Qian, J. Ye, L. Ren, *J Bionic Eng* **2015**, *12*, 624.

[74] H. J. Ensikat, P. Ditsche-Kuru, C. Neinhuis, W. Barthlott, *Beilstein J. Nanotechnol.* **2011**, *2*, 152.

[75] Z.-H. Lin, G. Cheng, W. Wu, K. Pradel, Z. Wang, *ACS Nano* **2014**, *8*, 6440.

[76] Z. He, M. Ma, X. Lan, F. Chen, K. Wang, H. Deng, Q. Zhang, Q. Fu, *Soft Matter* **2011**, *7*, 6435.

[77] M. Zhu, M. Z. Lerum, W. Chen, **2012**, *28*, 416.

[78] E. Hoque, D. J, P. Hoffmann, B. Bhushan, H. Mathieu, *J Phys Chem C* **2007**, *111*, 3956.

[79] S. ADIVA, W. Y, *Physiol Plant.* **1975**, *34*, 90.

[80] E. Chak, N. Pawlowska, C. Blaszykowski, M. Thompson, *Surf Interface Anal* **2013**, *45*, 1347.

[81] S. Duan, X. Xu, Z.-Q. Tian, Y. Luo, *Phys. Rev. B* **2012**, *86*, 045450.

[82] N. Saito, K. Hayashi, H. Sugimura, O. Takai, N. Nakagiri, *Chem. Phys. Lett.* **2001**, *349*, 172.

[83] B. de Boer, A. Hadipour, M. M. Mandoc, T. van Woudenbergh, W. M. P. Blom, *Adv Mater* **2005**, *17*, 621.

[84] D. Krishnan, H. T. Johnson, *J. Mech. Phys. Solids* **2009**, *57*, 1500.

[85] M. Avella-Oliver, R. Puchades, S. Wachsmann-Hogiu, A. Maquieira, *Sensors Actuators, B Chem.* **2017**, *252*, 657.

[86] H. Zuo, S. Wu, M. Li, Y. Li, W. Jiang, C. Mao, *Angew. Chemie - Int. Ed.* **2015**, *54*, 15118.

[87] M. Li, M. Zheng, S. Wu, C. Tian, D. Liu, Y. Weizmann, W. Jiang, G. Wang, C. Mao, *Nat. Commun.* **2018**, *9*, 2196.

[88] L. T. Varghese, L. Fan, Y. Xuan, C. Tansarawiput, S. Kim, M. Qi, *Small* **2013**, *9*, 3778.

[89] M. Li, H. Zuo, J. Yu, X. Zhao, C. Mao, C. Mao, S. L. Ginnell, C. Mao, N. C. Seeman, *Nanoscale* **2017**, *9*, 10601.

[90] M. Li, J. Yu, J. Li, E. Ben Wang, G. Wang, C. Mao, *RSC Adv.* **2016**, *6*, 76355.

[91] H. Jung, S. Kim, D. Han, J. Jang, S. Oh, J.-H. Choi, E.-S. Lee, J. W. Hahn, *J. Micromechanics Microengineering* **2015**, *25*, 055004.

[92] H. Schift, *J. Vac. Sci. Technol. B Microelectron. Nanom. Struct.* **2008**, *26*, 458.

[93] C. Peroz, V. Chauveau, E. Barthel, E. Søndergård, *Adv. Mater.* **2009**, *21*, 555.

[94] B. D. Lucas, J. S. Kim, C. Chin, L. J. Guo, *Adv. Mater.* **2008**, *20*, 1129.

[95] H. K. Raut, S. S. Dinachali, Y. C. Loke, R. Ganesan, K. K. Ansah-Antwi, A. Góra, E. H. Khoo, V. A. Ganesh, M. S. M. Saifullah, S. Ramakrishna, *ACS Nano* **2015**, *9*, 1305.

[96] Y. Ding, H. Wook Ro, T. A. Germer, J. F. Douglas, B. C. Okerberg, A. Karim, C. L. Soles, *ACS Nano* **2007**, *1*, 84.

[97] E. A. Costner, M. W. Lin, W.-L. Jen, C. G. Willson, *Annu. Rev. Mater. Res.* **2009**, *39*, 155.

[98] H. Schift, *Appl. Phys. A Mater. Sci. Process.* **2015**, *121*, 415.

[99] X.-M. Yan, S. Kwon, A. M. Contreras, J. Bokor, G. A. Somorjai, *Nano Lett.* **2005**, *5*, 745.

[100] R. S. Mishra, T. R. Bieler, A. K. Mukherjee, *Acta Metall. Mater.* **1995**, *43*, 877.

[101] S. Jin, Y. Wang, M. Motlag, S. Gao, J. Xu, Q. Nian, W. Wu, G. J. Cheng, *Adv. Mater.* **2018**, *30*, 1705840.

[102] B. Kaplan, H. Guner, O. Senlik, K. Gurel, M. Bayindir, A. Dana, *Plasmonics* **2009**, *4*, 237.

[103] X. Dou, P.-Y. Chung, P. Jiang, J. Dai, *Appl. Phys. Lett.* **2012**, *100*, 041116.

[104] S. Fu, Y. Wang, Y. Wang, *Polym. Test.* **2009**, *28*, 724.

[105] V. Liu, S. Fan, *Comput. Phys. Commun.* **2012**, *183*, 2233.

[106] G. R. Johnson, W. H. Cook, *Proc. 7th Int. Symp. Ballist.* **1983**, *547*, 541.

[107] D. J. Littlewood, in *Vol. 9 Mech. Solids, Struct. Fluids*, ASME, **2010**, pp. 209–217.

[108] J. Richeton, S. Ahzi, K. S. Vecchio, F. C. Jiang, R. R. Adharapurapu, *Int. J. Solids Struct.* **2006**, *43*, 2318.

[109] J. Homola, S. S. Yee, G. Gauglitz, *Sensors Actuators B Chem.* **1999**, *54*, 3.

[110] J. Dostálek, J. Homola, M. Miler, *Sensors Actuators B Chem.* **2005**, *107*, 154.

[111] B. Choi, X. Dou, Y. Fang, B. M. Phillips, P. Jiang, *Phys. Chem. Chem. Phys.* **2016**, *18*, 26078.

[112] B. K. Singh, A. C. Hillier, *Anal. Chem.* **2006**, *78*, 2009.

[113] J. Homola, I. Koudela, S. S. Yee, *Sensors Actuators B Chem.* **1999**, *54*, 16.

[114] A. Reserbat-Plantey, D. Kalita, Z. Han, L. Ferlazzo, S. Autier-Laurent, K. Komatsu, C. Li, R. Weil, A. Ralko, L. Marty, S. Guéron, N. Bendiab, H. Bouchiat, V. Bouchiat, *Nano Lett.* **2014**, DOI 10.1021/nl5016552.

[115] H. Li, Q. Zhang, C. C. R. Yap, B. K. Tay, T. H. T. Edwin, A. Olivier, D. Baillargeat, *Adv. Funct. Mater.* **2012**, *22*, 1385.

[116] Y. J. Yu, Y. Zhao, S. Ryu, L. E. Brus, K. S. Kim, P. Kim, *Nano Lett.* **2009**, DOI 10.1021/nl901572a.

[117] A. J. Baca, J.-H. Ahn, Y. Sun, M. A. Meitl, E. Menard, H.-S. Kim, W. M. Choi, D.-H. Kim, Y. Huang, J. A. Rogers, *Angew. Chem. Int. Ed. Engl.* **2008**, *47*, 5524.

[118] Y. Du, G. Qiu, Y. Wang, M. Si, X. Xu, W. Wu, P. D. Ye, *Nano Lett.* **2017**, *17*, 3965.

[119] H. Li, A. W. Contryman, X. Qian, S. M. Ardakani, Y. Gong, X. Wang, J. M. Weisse, C. H. Lee, J. Zhao, P. M. Ajayan, J. Li, H. C. Manoharan, X. Zheng, *Nat. Commun.* **2015**, DOI 10.1038/ncomms8381.

[120] Y. Wang, G. Qiu, R. Wang, S. Huang, Q. Wang, Y. Liu, Y. Du, W. A. Goddard, M. J. Kim, X. Xu, P. D. Ye, W. Wu, *Nat. Electron.* **2018**, DOI 10.1038/s41928-018-0058-4.

[121] P. L. Levesque, S. S. Sabri, C. M. Aguirre, J. Guillemette, M. Siaj, P. Desjardins, T. Szkopek, R. Martel, *Nano Lett.* **2011**, *11*, 132.

[122] M. F. El-Kady, V. Strong, S. Dubin, R. B. Kaner, *Science (80-. ).* **2012**, *335*, 1326.

[123] S. E. Thompson, M. Armstrong, C. Auth, M. Alavi, M. Buehler, R. Chau, S. Cea, T. Ghani, G. Glass, T. Hoffman, C.-H. Jan, C. Kenyon, J. Klaus, K. Kuhn, Z. Ma, B. Mcintyre, K. Mistry, A. Murthy, B. Obradovic, R. Nagisetty, P. Nguyen, S. Sivakumar, R. Shaheed, L. Shifren, B. Tufts, S. Tyagi, M. Bohr, Y. El-Mansy, *IEEE Trans. Electron Devices* **2004**, *51*, 1790.

[124] A. Castellanos-Gomez, R. Roldán, E. Cappelluti, M. Buscema, F. Guinea, H. S. J. van der Zant, G. A. Steele, *Nano Lett.* **2013**, *13*, 5361.

[125] R. Zhang, V. Koutsos, R. Cheung, *Appl. Phys. Lett.* **2016**, *108*, 042104.

[126] G.-H. Lee, R. C. Cooper, S. J. An, S. Lee, A. van der Zande, N. Petrone, A. G. Hammerberg, C. Lee, B. Crawford, W. Oliver, J. W. Kysar, J. Hone, *Science (80-. ).* **2013**, *340*, 1073.

[127] A. Volodin, C. Van Haesendonck, O. Leenaerts, B. Partoens, F. M. Peeters, *Appl. Phys. Lett.* **2017**, *110*, DOI 10.1063/1.4982931.

# VITA

Shengyu Jin was born in Yanji, Jilin Province, P. R. China. In 2008, he entered the Department of Materials Science and Engineering in University of Science and Technology of China (USTC), Hefei, China. He joined Prof. Shuhong Yu's group in Hefei National Laboratory for Physical Sciences at the Microscale as an undergraduate research assistant in October, 2010. He obtained a Bachelor Degree of Material Chemistry in 2012. In August of the same year, he pursued his graduate study at department of Civil & Environmental Engineering & Earth Sciences in University of Notre Dame, South Bend, IN, USA. In 2013, he transferred to the school of Industrial Engineering in Purdue University, West Lafayette, IN, USA. He started his Ph.D. program in Prof. Gary Cheng's group. Shengyu completed his Ph.D. in Industrial Engineering in December 2018.

# PUBLICATIONS


[1] D. Lin, M. Motlag, M. Saei, **S. Jin**, R.Rahimi, D. Bahr, and G. J. Cheng, "Shock engineering the additive manufactured graphene-metal nanocomposite with high density nanotwins and dislocations for ultra-stable mechanical properties", *Acta Materialia*, vol. 150, pp 360- 372, 2018.

[2] **S. Jin**, Y. Wang, M. Motlag, S. Gao, J. Xu, Q. Nian, W. Wu, and G.J. Cheng, "Large-Area Direct Laser-Shock Imprinting of a 3D Biomimic Hierarchical Metal Surface for Triboelectric Nanogenerators", *Advanced Materials*, vol. 30, pp 1705840, 2018

[3] G. Qiu, Q. Nian, M. Motlag, **S. Jin**, B. Deng, Y. Deng, A. R. Charnas, P. D. Ye, and G. J. Cheng, "Ultrafast Laser-Shock-Induced Confined Metaphase Transformation for Direct Writing of Black Phosphorus Thin Films", *Advanced Materials*, vol. 30, pp 1704405, 2018

[4] Q. Zhang, D. Lin, B. Deng, X. Xu, Q. Nian, **S. Jin**, K.D. Leedy, H. Li, and G. J. Cheng " Flyweight, Superelastic, Electrically Conductive, and Flame-Retardant 3D Multi-Nanolayer Graphene/Ceramic Metamaterial", *Advanced Materials*, vol. 29, pp 1605506, 2017

[5] Q. Nian, M. Saei, Y. Hu, B. Deng, **S. Jin**, and G. J. Cheng, "Additive roll printing activated cold welding of 2D crystals and 1D nanowires layers for flexible transparent conductor and planer energy storage", *Extreme Mechanics Letter*, vol. 9, pp 531- 545, 2016

[6] Z. Hu, M. Saei, G. Tong, D. Lin, Q. Nian, Y. Hu, **S. Jin**, J. Xu, and G. J. Cheng, "Numerical simulation of temperature field distribution for laser sintering graphene reinforced nickel matrix nanocomposites", *Journal of Alloys and Compounds*, vol. 688, pp 438- 448, 2016

[7] **S. Jin**, A. Ziabari, Y. R. Koh, M. Saei, X. Wang, B. Deng, Y. Hu, J. Bahk, A. Shakouri, and G. J. Cheng, "Enhanced thermoelectric performance of P-type BixSb2-xTe3 nanowires with pulsed laser assisted electrochemical deposition", *Extreme Mechanics Letter*, vol. 9, pp 386 – 396, 2016

[8] G. Qiu, Y. Du, A. Charnas, H. Zhou, **S. Jin**, Z. Luo, D. Y. Zemlyanov, X. Xu, and G. J. Cheng, P. D. Ye, "Observation of Optical and Electrical In-Plane Anisotropy in High-Mobility Few-Layer ZrTe5", *Nano Letters*, vol. 16, pp 7364 – 7369, 2016

[9] Y. Hu, Y. Xuan, X. Wang, B. Deng, M. Saei, **S. Jin**, J. Irudayaraj, and G.J. Cheng, "Superplastic Formation of Metal Nanostructure Arrays with Ultrafine Gaps", *Advanced Materials*, vol. 28, pp 9152 – 9162, 2016

[10] Z. Hu, G. Tong, D. Lin, Q. Nian, J. Shao, Y. Hu, M. Saei, **S. Jin**, and GJ Cheng, "Laser sintered graphene nickel nanocomposites", *Journal of Materials Processing Technology*, vol. 231, pp 143-150, 2016

[11] D. Lin, M. Saei, S. Suslov, **S. Jin**, and G.J. Cheng, "Super-strengthening and stabilizing with carbon nanotube harnessed high density nanotwins in metals by shock loading", *Scientific Reports*, vol. 5, pp 15405, 2015

[12] S. Das, Q. Nian, M. Saei, **S. Jin**, D. Back, P. Kumar, D. B. Janes, M. A. Alam, and G. J. Cheng, "Single-Layer Graphene as a Barrier Layer for Intense UV Laser-Induced Damages for Silver Nanowire Network", *ACS Nano*, vol. 9, pp 11121-11133, 2015

[13] D. Lin, **S. Jin**, F. Zhang, C. Wang, Y. Wang, C. Zhou, and G. J. Cheng, "3D stereolithography printing of graphene oxide reinforced complex architectures", *Nanotechnology*, vol. 26, pp 434003, 2015

[14] D. Lin, P. Kumar, **S. Jin**, S. Liu, Q. Nian, and G. J. Cheng, "Laser direct writing of crystalline Fe2O3 atomic sheets on steel surface in aqueous medium", *Applied Surface Science*, vol. 351, pp 148 – 154, 2015

[15] D. Lin, Q. Nian, B. Deng, **S. Jin**, Y. Hu, W. Wang, and G. J. Cheng, "Three-Dimensional Printing of Complex Structures: Man Made or toward Nature?", *ACS Nano*, vol. 8, pp 9710 – 9715, 2014

[16] P. Yang, **S. Jin**, Q. Xu, and S. H. Yu, "Decorating PtCo bimetallic alloy nanoparticles on graphene as sensors for glucose detection by catalyzing luminol chemiluminescence", *Small*, vol. 9, pp 199 – 204

[17] P. Yang, Q. Xu, **S. Jin**, Y. Lu, Y. Zhao, and S. H. Yu, "Synthesis of multifunctional Ag@ Au@ Phenol formaldehyde resin particles loaded with folic acids for photothermal therapy", *Chemistry-A European Journal*, vol. 18, pp 9294 – 9299, 2012

[18] P. Yang, Q. Xu, **S. Jin**, Y. Zhao, . Lu, X. Xu, and S.H. Yu, "Synthesis of Fe3O4@ Phenol Formaldehyde Resin Core–Shell Nanospheres Loaded with Au Nanoparticles as Magnetic FRET Nanoprobes for Detection of Thiols in Living Cells, *Chemistry-A European Journal*, vol. 18, pp 1154 – 1160, 2012

[19] **S. Jin**, Z. Zhou, E. Sakr, M. Motlag, P. Bermel, and G. J. Cheng, "Laser-induced scalable fabrication of nanophotonic patterns using low-cost optical discs", in preparation for *ACS Nano*

[20] H. Jiang†, **S. Jin**†, Y. Song, M. Gao, A. Shen, G. J. Cheng, and H. Deng, "Metal-Organic Framework for Laser Nano-Metallurgy", in preparation for *Journal of American Society of Chemistry*